UNIVERSITY OF CALIFORNIA SAN DIEGO

Data-driven and Model-based Methods for Wideband Source Localization

A dissertation submitted in partial satisfaction of the
requirements for the degree
Doctor of Philosophy

in

Electrical Engineering (Signal and Image Processing)

by

Yifan Wu

Committee in charge:

Professor Peter Gerstoft, Chair
Professor Florian Meyer
Professor Bhaskar D. Rao
Professor Rayan Saab

2023

The dissertation of Yifan Wu is approved, and it is acceptable in quality and form for publication on microfilm and electronically.

University of California San Diego

2023

DEDICATION

To my family.

EPIGRAPH

And you will seek Me and find Me if you search for Me with all your heart; And I will be found by you.

Jeremiah 29:13-14a

And we have the prophetic word made more firm, to which you do well to give heed as to a lamp shining in a dark place, until the day dawns and the morning star rises in your hearts.

2 Peter 1:19

TABLE OF CONTENTS

LIST OF FIGURES

LIST OF TABLES

ACKNOWLEDGEMENTS

I would first like to thank my advisor, Peter Gerstoft, for his support and guidance throughout my Ph.D. journey. He always gave me the freedom to explore the area that I was interested in and encouraged me to collaborate with other people to extend my network. He always encouraged me to attend academic conferences and workshops, which enabled me to interact with a lot of wonderful scholars in my field. He also taught me to have a critical eye on prior works and be skeptical when reading the papers, even the famous and well-cited papers. That greatly built my critical thinking skills. Without his help and support, it was impossible for me to finish this dissertation.

I would like to thank Professor Michael Wakin from the Colorado School of Mines especially. I still remembered that in the midst of the pandemic, Professor Wakin hosted me as a summer visitor to his group, and he drove for more than one hour each day to come to campus to discuss research with me. He motivated me to work on the atomic norm minimization problems. We met almost daily to discuss research and that summer was the most productive period throughout my entire graduate school. His insight and passion for mathematics significantly shaped my research mindset and motivated me to stay in academia. It is my great fortune to work with him and this dissertation owed a lot to him.

I would like to thank Roshan Ayyalasomayajula, Michael Bianco, and Dinesh Bharadia as my collaborators for my sound source localization project. It was a nice and enjoyable experience to work with them and I learned a lot from meeting with them.

I would like to thank my committee members, Professor Florian Meyer, Bhaskar D. Rao, and Rayan Saab, for their time and feedback.

I would like to thank my parents for their support and encouragement during the past four years. Their support gave me the power that made me preserve throughout the past years. I am also thankful to all the brothers and sisters I met in San Diego, Denver, and Princeton. In particular, I would like to thank Jingxue Lu, Eugene Kim, Charles Lu, Bryan Chen from San

Diego, Andy Yung, Judy Yung from Denver, and Joseph Ting from Princeton. It was grateful for me to meet you and thank you all for your caring and help for me in both human and spiritual ways.

This dissertation is a collection of papers that were published or have been submitted for publication. The text of Chapter Two is in full reprint of the material as it appears in Yifan Wu, Roshan Ayyalasomayajula, Michael J. Bianco, Dinesh Bharadia and Peter Gerstoft, ”Sound Source Localization based on Multi-task Learning and Image Translation Network,” *Journal of the Acoustical Society of America*, 150, 3374-3386. The dissertation author was the primary researcher and author of that chapter. The co-authors listed in these publications directed and supervised the research.

The text of Chapter Three is in full reprint of the material as it appears in Yifan Wu, Michael B. Wakin, and Peter Gerstoft, ”Gridless DOA Estimation with Multiple Frequencies”, *IEEE Transactions on Signal Processing*, 71, 417 - 432. The dissertation author was the primary researcher and author of that chapter. The co-authors listed in these publications directed and supervised the research.

The text of Chapter Four is in part and under some rearrangements a reprint of the material as it appears in Yifan Wu, Michael B. Wakin, and Peter Gerstoft, ”Regularization-free Gridless DOA Estimation for Multi-frequency Signals”, *IEEE Transactions on Signal Processing*, to be submitted 2023. The dissertation author was the primary researcher and author of that chapter. The co-authors listed in these publications directed and supervised the research.

VITA

2019	B.S. in Communication Engineering, Northeastern University
2021	M.S. in Electrical Engineering (Signal and Image Processing), University of California San Diego
2023	Ph. D. in Electrical Engineering (Signal and Image Processing), University of California San Diego
2020–2023	Research Assistant, University of California San Diego
2020–2021, 2023	Teaching Assistant, University of California San Diego
2022	Research Intern, NEC Laboratories America, Princeton, New Jersey

PUBLICATIONS

Wu, Y., Ayyalasomayajula, R., Bianco, M., Bharadia, D. and Gerstoft, P. "SSLIDE: Sound source localization for indoors based on deep learning", *IEEE International Conference on Acoustics, Speech, and Signal Processing*, 4680-4684, 2021.

Wu, Y., Ayyalasomayajula, R., Bianco, M., Bharadia, D. and Gerstoft, P. "Sound Source Localization based on Multi-task Learning and Image Translation Network", *The Journal of the Acoustical Society of America*, 150, 3374-3386, 2021.

Wu, Y., Wakin, M. B. and Gerstoft, P. "Gridless DOA Estimation under the Multi-frequency Model", *IEEE International Conference on Acoustics, Speech, and Signal Processing*, 5982-5986, 2022.

Wu, Y., Wakin, M. B. and Gerstoft, P. "Gridless DOA Estimation With Multiple Frequencies", *IEEE Transactions on Signal Processing*, 71, 417-432, 2023.

Wu, Y., Wakin, M. B. and Gerstoft, P. "Regularization-free Gridless DOA Estimation for Multi-frequency Signals", *to be submitted, IEEE Transactions on Signal Processing*, 2023.

ABSTRACT OF THE DISSERTATION

Data-driven and Model-based Methods for Wideband Source Localization

by

Yifan Wu

Doctor of Philosophy in Electrical Engineering (Signal and Image Processing)

University of California San Diego, 2023

Professor Peter Gerstoft, Chair

Wideband source localization is an important problem in signal processing, and it has wide-range applications in underwater acoustics, indoor speaker localization, teleconferencing, etc. Over the past few decades, there are a significant amount of methods proposed for wideband source localization. However, it still remains a challenging problem. This dissertation tackles wideband source localization from data-driven and model-based perspectives.

For the data-driven part, a novel deep learning framework for sound source localization (SSL) was proposed. SSL is to estimate the locations of the sound sources based on the received signal from the microphone array. SSL in the reverberant environment can be challenging due to the multipath artifacts in the received signals. To tackle with this challenge, a deep learning

framework based on multi-task learning and image translation (MTIT) network is proposed. MTIT utilizes the encoder-decoder structure and it consists of one encoder and two decoders. The encoder aims to obtain a compressed representation of the input while the two decoders focus on two tasks in parallel. One decoder focuses on mitigating the multipath caused by reverberation and the other decoder predicts the source location. Due to the explicit dereverberation module and the shared encoder (representation), the proposed localization framework can achieve superior performance and can generalize to the unseen data in the reverberant environment compared to the existing baseline methods.

For the model-based part, gridless direction-of-arrival (DOA) estimation based on atomic norm minimization (ANM) for the multi-frequency signal was studied. ANM was formulated to an equivalent computationally feasible semi-definite program (SDP) problem. The dual certificate condition is given to certify the optimality. A fast algorithm implementation is given and the dual problem of the SDP is considered. The method is further generalized to the non-uniform array and non-uniform frequency case. Extensive theoretical analysis and numerical experiments demonstrate the superior performance of the proposed method compared to sparse Bayesian learning, the existing grid-based multi-frequency DOA estimation method.

Chapter 1

Introduction

1.1 Background and Overview

Wideband source localization (WSL) is the problem of estimating the positions of one or more wideband sources in the space based on the received responses from the sensor arrays. It has wide-range applications in underwater acoustics, automatic speech recognition, speech enhancement, and human-robot interaction. In many practical cases, source localization is simplified to direction-of-arrival (DOA) estimation, i.e. it focuses on the estimation of the angles without the need of estimating the distance.

WSL has been extensively studied in the past few decades. However, it remains a challenging problem. The existing WSL methods can be divided into two main categories based on the methodology: model-based and data-driven. The initial research in WSL began with model-based methods. The model-based methods often relied on a well-defined physical model (usually called the forward model). They usually had a solid theoretical foundation while they relied on some critical assumptions which might limit their applications to real-world scenarios. In the past decade, data-driven based deep learning methods have received increasing attention and they have been applied to WSL. These methods demonstrate superior performance over conventional

signal processing methods. However, these data-driven methods require a demanding amount of training data to achieve satisfactory performance. The interpretability and generalization will also be potential issues for these data-driven methods.

This dissertation will consider WSL from both model-based and data-driven perspectives.

1. For the data-driven part, a novel deep learning framework to localize the sound sources under the indoor and reverberant environment is proposed. The deep learning framework is based on multi-task learning and the image translation network. The multi-task learning can overcome the challenges from the reverberation and the image translation modules can enhance the generalization.

2. For the model-based part, gridless DOA estimation for multiple frequencies is studied. Multiple frequencies can be used to characterize the wideband signal. The DOA estimation problem will be formulated as an optimization problem and the source DOA can be estimated without the need for grid search, which overcomes the quantization error from the grid mismatch.

1.2 Prior Works

1.2.1 Deep Learning based Sound Source Localization

Deep learning has been extensively applied to sound source localization recently [1, 3, 5, 14, 20, 22, 24, 25, 27, 31]. Most of the approaches are based on supervised learning. In [31], a multilayer perceptron DNN taking the generalized cross-correlation with phase transform (GCC-PHAT) features as inputs for direction of arrival (DOA) estimation. This classification based method shows improvement of the DOA estimation compared with the conventional signal processing based approaches. In [5], a SSL framework based on convolutional neural network (CNN) is proposed. The input features are the multichannel phase spectrograms and it can

localize multiple sources in reverberant environment. DeepGCC [24], a SSL model based on CNN and generalized cross correlation (GCC) is presented in [24]. The network can be adapted to different microphone geometries without the need of retraining. The authors in [1] propose a convolutional recurrent DNN for SSL and sound event detection. The architecture contains a series of convolutional layers followed by max-pooling and bidirectional GRU (BGRU) layers. A feedforward layer is then used for spatial pseudo-spectrum (SPS) estimation. The SPS is an intermediate output and is shown to be useful for SSL. In [25], a robust SSL guided by deep learning based time-frequency masking framework is presented. In [20], a deep learning based SSL method is proposed, which uses two orthogonal first-order differential microphone arrays. The sound intensity is considered and phase transform (PHAT) weighting is used to improve the robustness against reverberation. There are also some works that use unsupervised learning [22], as well as semi-supervised learning methods based on manifold learning [14] and deep generative modeling [3]. These works do not assume all of the labels (ground-truth source positions) are available, and can perform well in label-limited scenarios.

1.2.2 Atomic Norm Minimization

ANM was initially proposed in [6] as a general framework for promoting sparse signal decompositions. The pioneering ANM paper [4] worked directly with the continuous (temporal) frequency estimation problem and considered the complete data case. As long as the temporal frequency separation was greater than a certain minimum separation, exact recovery of the active temporal frequencies was guaranteed. Furthermore, a semidefinite programming (SDP) framework that characterized the ANM problem was presented. The authors in [23] studied continuous temporal frequency estimation based on randomly sampled data for the single measurement vector (SMV) case. The minimum separation condition was relaxed in [12]. ANM for multiple measurement vectors (MMVs) was studied in [19, 36, 38]. In [8], the author considered a super-resolution problem that had a similar setup to [4] except that the point spread function was

assumed to be unknown. Based on the assumption that the point spread function was stationary and lived in a known subspace, the lifting trick was applied, and the problem was formulated using ANM. The model was generalized to non-stationary point spread functions in [34]. The sample complexity of modal analysis with random temporal compression was established in [18]. ANM for 2D temporal frequency estimation was studied in [9]. In [37], the authors proposed a reweighted ANM framework, which enhances the sparsity and achieves super-resolution. An atomic norm for DOA estimation under gain-phase noise [7] was proposed to mitigate the artifacts for electromagnetic signals. ANM was also recently applied in digital beamforming [16, 30], adaptive interference cancellation [15], denoising [2, 17], and blind demodulation [32, 33]. [10] gave a comprehensive overview of ANM and its applications.

1.3 Research Contributions

1.3.1 Data-driven WSL

This dissertation studied data-driven WSL by proposing a novel multi-task learning (MTL) framework for indoor sound source localization (SSL) [26, 27]. SSL is to estimate the locations of the sound sources based on the received signal from the microphone array. SSL is an important problem in WSL and it has widespread applications in human-robot interaction, teleconferencing, and audio scene monitoring. However, SSL in the reverberant environment is challenging due to the multipath artifacts in the received signals. Therefore, it is important to incorporate the dereverberation module in the localization system.

The received signal from the microphone array was a time series. The beamforming technique is initially applied to obtain the beamspectrum surface in two-dimensional space. The beamspectrum surface is treated as an image and it will be the input to the DNN. The input, output, and target are all images and we can incorporate the idea of the state-of-the-art image translation network into the network design. The encoder-decoder architecture with one encoder and two

parallel decoders is employed. The intuition for using two decoders originates from MTL [21, 39]. By training the network to learn multiple different tasks simultaneously, it performs better than just learning the primary task. It acts as regularization and helps the shared layers to obtain a more general representation of the input. Although one may only be interested in localization as our primary task, a multipath alleviation decoder to learn how to compensate for the extra range from the multipath is included as our auxiliary task. By training the network to perform both tasks (i.e. two different decoders sharing the same encoder), the higher-level feature representations in the encoder can be improved. The benefit of applying MTL is that the model complexity is only increased during the training phase. During the testing phase, only the primary task is performed and the auxiliary task is discarded.

Extensive experiments are conducted to verify the effectiveness of the proposed method. The experiments show that the proposed method can outperform the classical signal processing based methods and the state-of-the-art convolutional neural network (CNN). The ablation study shows the importance of the multipath alleviation decoder to reduce multipath and the generalization experiments show strong generalization abilities and robustness against the mismatch between the training and testing data.

1.3.2 Model-based WSL

For the model-based part, gridless DOA estimation under multiple frequencies is studied [28, 29]. The multi-frequency model can characterize the wideband signal. Atomic norm minimization (ANM), a modern optimization technique was used to achieve the continuous (gridless) DOA estimation. There are some technical challenges to extending ANM from single-frequency to multi-frequency cases. First, in the multi-frequency setup, each channel (frequency) is modulated with a different sinusoid and that *heterogeneous* modulation makes it difficult to derive an equivalent SDP based on the Vandermonde decomposition as has been done in many prior works. Second, each frequency other than the first frequency will experience spatial aliasing

of the DOAs. We developed a novel solution to overcome these two challenges. Our main contributions are summarized as follows:

- **(1) Formulate an equivalent SDP problem.** Although ANM itself is a convex optimization problem, it is not directly solvable due to an infinite number of optimization parameters. Therefore, it is critical to find a computationally feasible solution that equivalently characterizes the ANM problem. Several prior works showed that certain ANM problems could be equivalently characterized by SDPs [19, 23, 38]. The derivation of an SDP problem typically relied on a Vandermonde decomposition and equivalence with the ANM could be proved by showing that the SDP solution was both an upper and a lower bound for the ANM [19, 23, 38]. Unfortunately, this commonly used technique cannot be applied in the multi-frequency case due to the heterogeneous temporal frequencies across different channels. In [13, 16], certain SDPs were derived using the Vandermonde decomposition, but only the lower bound for the ANM problem could be guaranteed. In [29], an equivalent SDP based on the bounded real lemma for trigonometric polynomials [11] is derived. This equivalent SDP provided a computationally feasible solution for the ANM when multiple frequencies were considered. That paper also explained how the proposed SDP was the dual to a minor adaptation of the SDP proposed in [35] for line spectrum estimation with harmonics.

- **(2) Provide the dual certificate condition.** The dual certificate condition that could be used to certify the optimal atomic decomposition is derived. In particular, the DOAs of the sources are localized with the help of the dual polynomial arising from the ANM optimization problem. As long as the dual polynomial satisfies the dual certificate condition, the frequencies can be localized by finding the roots of a polynomial. Therefore, the dual certificate condition not only provides a theoretical guarantee for the optimality but also offers a method for DOA estimation.

- **(3) Construct the dual polynomial that satisfies the dual certificate condition.** In cases where the existence of a dual polynomial that satisfies the dual certificate condition can be proved, then the optimality and therefore exact DOA estimation is guaranteed. The dual polynomial based on Fejér kernel is constructed. It is shown that under some assumptions, the constructed dual polynomials will satisfy the dual certificate condition.

- **(4) Fast implementation.** A fast implementation is proposed so that the SDP has a reduced size. This fast implementation also extends the approach to an arbitrary set of frequencies. Numerical results show that the dual polynomial still serves as a precise indicator for the DOAs. Hence, in terms of the DOA estimation, the algorithm succeeds even when aliasing is present.

- **(5) Extend to multiple measurement vector (MMV) and non-uniform case.** The ANM framework is initially derived under the assumption that both the frequency set and the array spacing is uniform. It turns out that it can be further extended to MMV and non-uniform cases (both the array spacing and frequency set can be non-uniform). The SDP is formulated in the primal domain and the DOAs can be extracted based on irregular Vandermonde decomposition (IVD). The existence of IVD is formally proved.

- **(6) Regularization-free Framework.** Both the primal and dual SDP formulation are considered. Compared to the dual formulation, the primal formulation is more favorable as it does not need regularization to achieve the robustness to the noise and aliasing. The robustness to the noise and aliasing is obtained through the post-optimization step. Therefore, it overcomes the regularization bias and can obtain an improved performance.

- **(7) More sources than sensors under the uniform linear array case** Prior works showed that the maximum number of uniquely identifiable sources in an N_m-element uniform linear array (ULA) is $N_m - 1$. However, it turns out that it is possible to overcome such a bottleneck in the multi-frequency case. The physical intuition is that multiple frequencies increase the

diversity of the harmonics and these "new harmonics" can serve as extra "virtual sensors" in a large virtual array. Due to such an intrinsic property of the multi-frequency signal model, it is possible to break through such a bottleneck in the ULA setup. In many practical scenarios, the array geometry is fixed and ULA is one of the most commonly used arrays. Hence, this result has a practical impact and demonstrates the benefit of multi-frequency processing.

1.4 Dissertation Organization

This dissertation is organized as follows. Chapter 2 will introduce the data-driven sound source localization methods. Chapters 3 and 4 will introduce the model-based source localization methods. In specific, Chapter 3 will focus on the development of the gridless DOA estimation method for multiple frequencies based on ANM. The DOA can be estimated by first solving an SDP problem and then finding the roots of a polynomial. We call this framework the dual formulation as we work on the dual polynomial. Chapter 4 is an extension of the work done in Chapter 3. The primal formulation is considered and the benefit of this formulation is that the regularization bias can be avoided. In addition, the method is extended to the MMV case, and it can also deal with NUA and NUF cases, which makes the method more general and practical. Chapter 5 concludes the dissertation.

Bibliography

[1] S. Adavanne, A. Politis, J. Nikunen, and T. Virtanen. Sound event localization and detection of overlapping sources using convolutional recurrent neural networks. *IEEE J. Sel. Topics Signal Process.*, 13(1):34–48, 2018.

[2] B. N. Bhaskar, G. Tang, and B. Recht. Atomic norm denoising with applications to line spectral estimation. *IEEE Trans. Signal Process.*, 61(23):5987–5999, 2013.

[3] M. J. Bianco, S. Gannot, E. Fernandez-Grande, and P. Gerstoft. Semi-supervised source

localization in reverberant environments with deep generative modeling. *IEEE Access*, 2021.

[4] E. J. Candès and C. Fernandez-Granda. Towards a mathematical theory of super-resolution. *Commun. Pure Appl. Math.*, 67(6):906–956, 2014.

[5] S. Chakrabarty and E. A. P. Habets. Multi-speaker DOA estimation using deep convolutional networks trained with noise signals. *IEEE J. Sel. Topics Signal Process.*, 13(1):8–21, 2019.

[6] V. Chandrasekaran, B. Recht, P. A. Parrilo, and A. S. Willsky. The convex geometry of linear inverse problems. *Found. Comput. Math.*, 12(6):805–849, 2012.

[7] P. Chen, Z. Chen, Z. Cao, and X. Wang. A new atomic norm for DOA estimation with gain-phase errors. *IEEE Trans. Signal Process.*, 68:4293–4306, 2020.

[8] Y. Chi. Guaranteed blind sparse spikes deconvolution via lifting and convex optimization. *IEEE J. Sel. Topics Signal Process.*, 10(4):782–794, 2016.

[9] Y. Chi and Y. Chen. Compressive two-dimensional harmonic retrieval via atomic norm minimization. *IEEE Trans. Signal Process.*, 63(4):1030–1042, 2014.

[10] Y. Chi and M. F. Da Costa. Harnessing sparsity over the continuum: Atomic norm minimization for superresolution. *IEEE Signal Process. Mag.*, 37(2):39–57, 2020.

[11] B. Dumitrescu. *Positive trigonometric polynomials and signal processing applications*, volume 103. Springer, 2017.

[12] C. Fernandez-Granda. Super-resolution of point sources via convex programming. *Inf. Inference, J. IMA*, 5(3):251–303, 2016.

[13] J. W. Helland. *Atomic Norm Algorithms for Blind Spectral Super-resolution Problems*. Colorado School of Mines, 2019.

[14] B. Laufer-Goldshtein, R. Talmon, and S. Gannot. Semi-supervised sound source localization based on manifold regularization. *IEEE/ACM Trans. Audio, Speech, and Lang. Process.*, 24(8):1393–1407, 2016.

[15] S. Li, D. Gaydos, P. Nayeri, and M. B. Wakin. Adaptive interference cancellation using atomic norm minimization and denoising. *IEEE Antennas Wirel. Propag. Lett.*, 19(12):2349–2353, 2020.

[16] S. Li, P. Nayeri, and M. B. Wakin. Digital beamforming robust to time-varying carrier frequency offset. *arXiv preprint arXiv:2103.04948*, 2021.

[17] S. Li, M. B. Wakin, and G. Tang. Atomic norm denoising for complex exponentials with unknown waveform modulations. *IEEE Trans. Inf. Theory*, 66(6):3893–3913, 2019.

[18] S. Li, D. Yang, G. Tang, and M. B. Wakin. Atomic norm minimization for modal analysis from random and compressed samples. *IEEE Trans. Signal Process.*, 66(7):1817–1831, 2018.

[19] Y. Li and Y. Chi. Off-the-grid line spectrum denoising and estimation with multiple measurement vectors. *IEEE Trans. Signal Process.*, 64(5):1257–1269, 2015.

[20] N. Liu, H. Chen, K. Songgong, and Y. Li. Deep learning assisted sound source localization using two orthogonal first-order differential microphone arrays. *J. Acoust. Soc. Am.*, 149(2):1069–1084, 2021.

[21] S. Ruder. An overview of multi-task learning in deep neural networks. *arXiv preprint arXiv:1706.05098*, 2017.

[22] R. Takeda and K. Komatani. Unsupervised adaptation of deep neural networks for sound source localization using entropy minimization. In *IEEE ICASSP*, pages 2217–2221, 2017.

[23] G. Tang, B. N. Bhaskar, P. Shah, and B. Recht. Compressed sensing off the grid. *IEEE Trans. Inf. Theory*, 59(11):7465–7490, 2013.

[24] J. M. Vera-Diaz, D. Pizarro, and J. Macias-Guarasa. Acoustic source localization with deep generalized cross correlations. *Signal Process.*, 2021.

[25] Z. Q. Wang, X. Zhang, and D.-L. Wang. Robust speaker localization guided by deep learning-based time-frequency masking. *IEEE/ACM Trans. Audio, Speech, Lang. Process.*, 27(1):178–188, 2018.

[26] Y. Wu, R. Ayyalasomayajula, M. J. Bianco, D. Bharadia, and P. Gerstoft. Sound source localization based on multi-task learning and image translation network. *The Journal of the Acoustical Society of America*, 150(5):3374–3386, 2021.

[27] Y. Wu, R. Ayyalasomayajula, M. J. Bianco, D. Bharadia, and P. Gerstoft. Sslide: Sound source localization for indoors based on deep learning. In *IEEE ICASSP*, pages 4680–4684, 2021.

[28] Y. Wu, M. B. Wakin, and P. Gerstoft. Gridless DOA estimation under the multi-frequency model. In *IEEE ICASSP*, pages 5982–5986, 2022.

[29] Y. Wu, M. B. Wakin, and P. Gerstoft. Gridless doa estimation with multiple frequencies. *IEEE Trans. Signal Process.*, 71:417–432, 2023.

[30] A. Xenaki and P. Gerstoft. Grid-free compressive beamforming. *J. Acoust. Soc. Am.*, 137:1923–1935, 2015.

[31] X. Xiao, S. Zhao, X. Zhong, DL. Jones, E. S. Chng, and H. Li. A learning-based approach to direction of arrival estimation in noisy and reverberant environments. In *IEEE ICASSP*, pages 2814–2818, 2015.

[32] Y. Xie, M. B. Wakin, and G. Tang. Simultaneous sparse recovery and blind demodulation. *IEEE Trans. Signal Process.*, 67(19):5184–5199, 2019.

[33] Y. Xie, M. B. Wakin, and G. Tang. Support recovery for sparse signals with unknown non-stationary modulation. *IEEE Trans. Signal Process.*, 68:1884–1896, 2020.

[34] D. Yang, G. Tang, and M. B. Wakin. Super-resolution of complex exponentials from modulations with unknown waveforms. *IEEE Trans. Inf. Theory*, 62(10):5809–5830, 2016.

[35] Z. Yang. A gridless sparse method for super-resolution of harmonics. In *IEEE EUSIPCO*, pages 2096–2100, 2017.

[36] Z. Yang, J. Tang, Y. C. Eldar, and L. Xie. On the sample complexity of multichannel frequency estimation via convex optimization. *IEEE Trans. Inf. Theory*, 65(4):2302–2315, 2018.

[37] Z. Yang and L. Xie. Enhancing sparsity and resolution via reweighted atomic norm minimization. *IEEE Trans. Signal Process.*, 64(4):995–1006, 2015.

[38] Z. Yang and L. Xie. Exact joint sparse frequency recovery via optimization methods. *IEEE Trans. Signal Process.*, 64(19):5145–5157, 2016.

[39] Y. Zhang and Q. Yang. A survey on multi-task learning. *arXiv preprint arXiv:1707.08114*, 2017.

Chapter 2

Sound source localization based on multi-task learning and image translation network

Supervised learning-based sound source localization (SSL) methods have been shown to achieve a promising localization accuracy in the past. In this paper, *MTIT*, sound source localization for indoors using Multi-Task learning and Image Translation network, an image translation-based deep neural networks (DNNs) framework for sound source localization is presented to predict the locations of sound sources with random positions in a continuous space. We extract and represent the spatial features of the sound signals as beam response at each direction which can indicate the chance of the source in each point of the room. We utilize the multi-task learning (MTL) based training framework. There are one encoder and two decoders in our DNN. The encoder aims to obtain a compressed representation of the input beamspectrum surfaces while the two decoders focus on two tasks in parallel. One decoder focuses on resolving the multipath caused by reverberation and the other decoder predicts the source location. Since these two decoders share the same encoder, by training these two decoders in parallel, the

shared representations are refined. We comprehensively evaluate the localization performance of our method in the simulated data, measured impulse response and real recordings datasets and compare it with multiple signal classification (MUSIC), steered response power with phase transform (SRP-PHAT), and a competing convolutional neural network (CNN) approach. It turns out that MTIT can outperform all of the baseline methods in a dynamic environment and also can achieve a good generalization performance.

2.1 Introduction

Sound source localization (SSL) has widespread applications in human–robot interaction [1, 2], ocean acoustics [3, 4], hearing aids [5, 6], teleconferencing [7], automatic speech recognition [8, 9], and audio scene monitoring [10]. For example, in a hospital, attending robots can locate and attend to patients based on their voices [11]. However, SSL in reverberant environments is challenging due to multipath artifacts in received signals. This effect degrades SSL performance. Thus, it is important to develop SSL methods that are robust to reverberation [12].

While traditional SSL algorithms [13–16] rely on estimation theory or statistics, they fail in dynamic and reverberant environments. A well-known subspace based technique, multiple signal classification (MUSIC) [13] is known to suffer from correlated sources which are prevalent in reverberant environments. Another classical SSL method, steered response power with phase transform (SRP-PHAT) [14–16] has been shown to not be robust to non-stationary signals like speech. Recently, SSL approaches based on deep neural networks (DNNs) have been proposed [17–26]. Most of the approaches are based on supervised learning. In Ref [17], a multilayer perceptron DNN taking the generalized cross-correlation with phase transform (GCC-PHAT) features as inputs for direction of arrival (DOA) estimation. This classification based method shows improvement of the DOA estimation compared with the conventional signal processing based approaches. In Ref [18], a SSL framework based on convolutional neural

network (CNN) is proposed. The input features are the multichannel phase spectrograms and it can localize multiple sources in reverberant environment. DeepGCC [19], a SSL model based on CNN and generalized cross correlation (GCC) is presented in [19]. The network can be adapted to different microphone geometries without the need of retraining. The authors in [20] propose a convolutional recurrent DNN for SSL and sound event detection. The architecture contains a series of convolutional layers followed by max-pooling and bidirectional GRU (BGRU) layers. A feedforward layer is then used for spatial pseudo-spectrum (SPS) estimation. The SPS is an intermediate output and is shown to be useful for SSL. In [21], a robust SSL guided by deep learning based time-frequency masking framework is presented. In [22], a deep learning based SSL method is proposed, which uses two orthogonal first-order differential microphone arrays. The sound intensity is considered and phase transform (PHAT) weighting is used to improve the robustness against reverberation. There are also some works that use unsupervised learning [23], as well as semi-supervised learning methods based on manifold learning [24] and deep generative modeling [25]. These works do not assume all of the labels (ground-truth source positions) are available, and can perform well in label-limited scenarios.

In this work, we present *MTIT*, an SSL method based on multi-task learning with image translation network. Multi-task learning [27–29] (MTL), a training framework with multiple tasks (including both the primary task and auxiliary tasks) in parallel, have received much attention in the machine learning community. It can be thought as inductive transfer, or transfer learning, in which knowledge obtained from one task is applied to other tasks [27–29]. Since related tasks often share representations or parameters, learning the auxiliary tasks can help the network to perform better in the primary task. The benefit of MTL is that it only increases the complexity in the training phase and the auxiliary tasks will be turned off during the testing stage. In recent years, MTL has been successfully applied in speech recognition [30], natural language processing [31], and computer vision [32].

For SSL problem, by applying the standard beamforming technique, the features can be

extracted as an image in spatial dimension. With the help of this representation, we can apply the image translation network to learn how to generate the desired image. The generated image contains the location of the source and therefore the source can be localized. Hence, the SSL problem is framed as an image translation problem. Image Translation [33–35] has been well studied in the computer vision community. The key idea of image translation is to utilize the generator models focusing on outputting synthetic images that fit the target paired with tailored targets and loss functions to solve image-to-image translation problems like real-to-art image translations [34], image denoising [35] etc.

We use the MTL framework via an encoder-decoder structure to localize sound sources in reverberant and dynamic environments. Inspired by [36], we have one encoder to obtain the compressed representation of the input and two decoders to solve the localization and multipath alleviation tasks simultaneously. Since these two decoders share the same encoder for related tasks, in training the two decoders can help each other. Therefore, although we are only interested in localization, the localization decoder can benefit from the multipath alleviation decoder and perform better in localization.

We train and test our model using reverberant speech under four datasets including simulated data, Multiple Impulse Response Dataset (MIRD) [37], one dataset from Technical University of Denmark (DTU) [38], and Sound source localization for robots (SSLR) [39]. For the first 3 datasets, the reverberant speech is obtained by convolving the clean speech from LibriSpeech corpus [40] with the room impulse responses (RIRs) either from simulation (for simulated data) or real measurements (for MIRD and DTU dataset). For the SSLR dataset, the reverberant speech is directly obtained from the microphone recordings in the robots.

We compare MTIT with other SSL methods, including MUSIC [13], SRP-PHAT [14–16], and CNN [18]. Based on the experiment results, we find MTIT outperforms the baseline methods in all of the four datasets. In addition, MTIT can also achieve a good generalization performance and be robust against the mismatch between the training and testing data.

In Sec. 2.2, we introduce the technical details of MTIT. In specific, we discuss the details about feature extraction, range compensation, target processing and network architecture. The experiments and details of the four datasets are presented in Sec. 2.3 and 2.4. Sec. 2.5 shows the testing results for MTIT and other baseline methods and parameter studies for the number of microphones and microphone spacing under MIRD dataset. The ablation study and generalization evaluation are conducted in Sec. 2.6 and 2.7, respectively. Finally, Sec. 2.8 concludes the paper.

2.2 Proposed Method

To understand how the proposed DNN solves for the reverberation problem and helps in effective SSL, let us first look into the fundamentals of sound transmissions in a given environment. Consider the acoustics signals in the time domain

$$y_m = s * h_m + n_m \tag{2.1}$$

where $y_m \in \mathbb{R}^L$ is the signal received by mth microphone ($m \in \{1 \dots M\}$, M is number of microphones), s the source signal, and n_m the noise for the mth microphone. h_m is the RIR, which characterizes the reverberation of the room. Denote $\mathbf{y} = [y_1 \dots y_M]^T \in \mathbb{R}^{M \times L}$ as the collection of the received signal from all sensors with audio length L.

For N arrays with K microphones in each array (i.e. $M = NK$), $\mathbf{y}$ can be reshaped as a tensor with dimension $K \times N \times L$. In the following sessions, $\mathbf{y} \in \mathbb{R}^{K \times N \times L}$.

2.2.1 Features extraction

Features extraction is one of the key steps in designing the DNN model. In our work, we will try to use images to represent the input, output and target so that we can leverage the state of the art image translation network [33, 34] which has been shown great potential in the computer

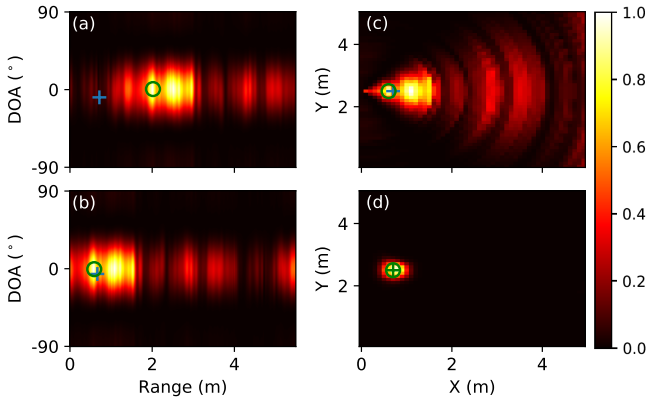

Figure 2.1: Beamspectrum surfaces (a) before and (b) after range compensation, and (c) after range compensation and coordinate transformation, (d) Output beamspectrum surface from localization decoder. The correct source position (+), and maximum value or predicted location (○) are indicated.

vision community. The spatial features are encoded as images and the network is directly trained to generate images. By decoding these output images, we can find out the locations of sound sources.

We first use standard beamforming to obtain source location beamspectrum surfaces in a 2D space. We first consider the short time Fourier transform (STFT) of the received signal (in the time domain) $\mathbf{y} \in \mathbb{R}^{K\times N\times L}$. The number of snapshots can be expressed in terms of the audio length L and fast Fourier transform (FFT) window length F as $S = \frac{L}{2F}$ (only the positive half of the frequency bins are considered). Hence, we obtain $\mathbf{Y} \in \mathbb{C}^{S\times F\times K\times N}$ as the STFT output for $\mathbf{y}$. Note that the above $\mathbf{Y}$ is evaluated for the single measurement case. If we have T independent measurements in the dataset, then there are $C = TS$ frames for $\mathbf{Y}$ (i.e. $\mathbf{Y} \in \mathbb{C}^{C\times F\times K\times N}$).

DOA Features Extraction

Assuming a uniform linear array (ULA) and a broadband signal, the magnitude of conventional beamforming output on any arbitary angle θ is

$$P(\theta) = |\mathbf{w}_\theta^H \mathbf{Y}_f^{ns}| = |\sum_{k=1}^{K} \mathbf{Y}_f^{ns}[k] e^{j\frac{2\pi k u \sin\theta f_0}{c}}| \tag{2.2}$$

where $\mathbf{w}_\theta = [e^{-j\frac{2\pi u \sin\theta f_0 1}{c}} \quad ... \quad e^{-j\frac{2\pi u \sin\theta f_0 K}{c}}]^T$, u, f_0 and c stand for the spacing between microphones, median frequency and speed of sound. Each point in $P(\theta)$ indicates the similarity of the signal to the expected beamformer response based on free-space propagation. $\mathbf{Y}_f^{ns} \in \mathbb{C}^{K\times 1}$ is a slice of $\mathbf{Y}$ for nth array, sth snapshot and fth frequency bin.

Range Features Extraction

Now that we know how to extract the features of DOA in the free space cases, let's take a look at how to obtain the features of range. Suppose we only consider the phase difference due to the range, similar to the angle features extraction, the conventional beamforming output at range d is

$$P(d) = |\mathbf{w}_d^H \mathbf{Y}_k^{ns}| = |\sum_{l=1}^{F} \mathbf{Y}_k^{ns}[l] e^{j\frac{2\pi l f_l d}{c}}|, \tag{2.3}$$

where $\mathbf{w}_d = [e^{-j\frac{2\pi f_1 d 1}{c}} \quad ... \quad e^{-j\frac{2\pi f_F d F}{c}}]^T$, and $\mathbf{Y}_k^{ns} \in \mathbb{C}^{F\times 1}$ is a slice of $\mathbf{Y}$ for kth microphone in nth array and sth snapshot. f_l is the frequency corresponding for the lth frequency bin.

DOA-Range Features Extraction

We can define a 2-D function [41] combining (2.2) and (2.3) which can indicate the chance of the signal coming from the angle θ and distance d for array $n \in \{1,...,N\}$ and frame $s \in \{1,...,S\}$

$$P_{ns}(\theta, d) = |\mathbf{w}_\theta^H \mathbf{Y}^{ns} \mathbf{w}_d^*| = |\sum_{k=1}^{K}\sum_{l=1}^{F} Y_{kl} e^{j\frac{2\pi k u \sin\theta f_0}{c}} e^{j\frac{2\pi l f_l d}{c}}| \tag{2.4}$$

where $\mathbf{Y}^{ns}[k,l] = Y_{kl}$. $P_{ns}(\theta,d)$ is the magnitude of 2-D conventional beamformer output. Y_{kl} represents the STFT output for the kth microphone and lth frequency bin. $(\cdot)^H$, $(\cdot)^T$ and $(\cdot)^*$ are Hermitian transpose, transpose and complex conjugate, separately. When the sound source is from the ground-truth angle and range, then $P_{ns}(\theta,d)$ have a high value. Therefore, $P_{ns}(\theta,d)$ can indicate how likely the source is from each candidate angle θ and range d in the searching space. If we have U and V grid points for θ and d, then we will obtain a beamspectrum surface with dimension $U \times V$ which can indicate the chance of the signal in the given θ and d. Fig. 2.1 (a) is one of the examples.

It is worth mentioning that we applied 2-D conventional beamforming technique to extract the features. There exists other feature extraction techniques like SRP-PHAT. However, it is shown to be computationally prohibitive due to the grid search [42].

For reverberation and noise free data, the localization is simply identifying the θ and d that correspond to the maximum value in the beamspectrum surface [36]. Due to the reverberation, much of the sound received by the microphones is a result of multipath, which is a complicated function of the different microphone locations relative to the source. Therefore, peaks in the beamspectrum surface may no longer indicate the correct result in terms of their predicted distance d as depicted in Fig. 2.1 (a).

2.2.2 Range compensation

To help overcome challenges of source localization in reverberant environments, we design a second decoder to correct for variation in multipath artifacts due to differences in microphone location. Details on the decoder and the loss function are further described in Sec. 2.2.4.

To enable this decoder to learn to alleviate range offsets cause by multipath artifacts, we will artificially generate beamspectrum surfaces with range compensation. These artificial beamspectra will be used as targets of the range compensation decoder in the training phase.

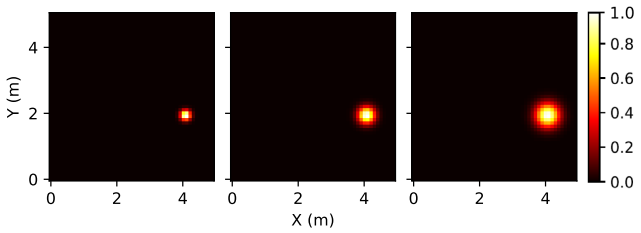

Figure 2.2: Target images under different σ. From left to right, the values of σ are 0.15, 0.25 and 0.35, respectively.

To generate the artifical beam spectra, we first identify the direct path as the path with the least range measurement, $\hat{d}$ in the incorrect range image as shown in Fig. 2.1 (a). We assume there exists a direct path between the source and at least one of the arrays. We then use the actual range measurement expected range measurement, d, from the given ground truth location for that specific measurement. We then compensate this offset in the given RIR measurement to get the expected beamspectrum profile as seen in Fig. 2.1 (b). More formally, for the STFT output in the sth frame and kth microphone of the nth array $Y_k^{ns} \in \mathbb{C}^{F\times 1}$, the range is compensated by

$$\bar{Y}_k^{ns} = Y_k^{ns} \circ e^{j2\pi\vartheta\frac{\hat{d}_n - d_n}{c}} \tag{2.5}$$

where $\vartheta = [f_1, ..., f_F]^T \in \mathbb{R}^{F\times 1}$ is a collection of all frequencies. Scalar d_n and $\hat{d}_n$ are the estimated ranges for the direct path and true ranges of the nth array, and $\circ$ represents the Hadamard product. Fig. 2.1 (b) shows the beamspectrum surface after range compensation. Our results show that the range compensation will make it easier for DNN to identify the correct location of the sound source.

We have generated two categories of beamspectrum surfaces with dimension $U \times V$. While we can perform single point identification based object detection tasks on these images, each of these images are with respect to their own microphones and lack the context of the global coordinates. To overcome that problem, we convert these range-angle images into 2D Cartesian images which show the coordinate with respect to one of the arrays. We perform a coordinate

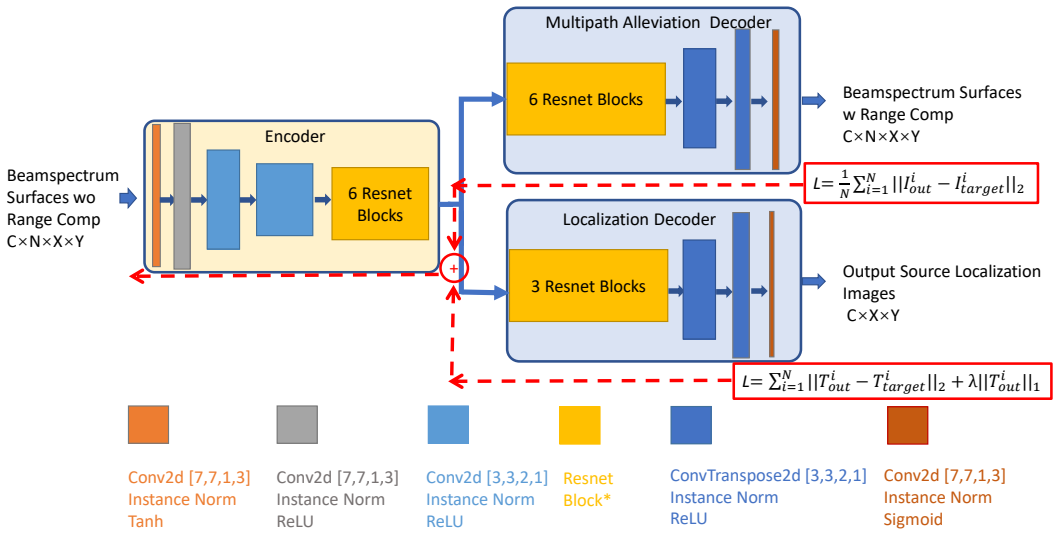

Figure 2.3: MTIT architecture. C, N are number of datapoints, number of arrays, and X, Y are dimensions for the images. [a, a, b, c] stand for kernel size a $\times$ a, stride b and padding c. The red dashed shows the directions for the back-propagation of the loss through the network.

transform on these images to convert to a 2-D Cartesian plane with dimension $Y \times X$ as shown in Fig. 2.1 (c) to encode the locations of these multiple arrays.

2.2.3 Localization targets

Now that we have defined the images for us to perform the single source localization, we need to define the targets for the network to learn the SSL task. Since we are using an image translation network, the target is also represented as an image. In our work, we use a negative exponential label to represent the target position in 2-D space. The target of the network will also be a heatmap image with dimension $Y \times X$. The distance between a random position (x', y') and ground-truth position (x, y) is

$$d(x', y') = \sqrt{(x' - x)^2 + (y' - y)^2}; \tag{2.6}$$

Then its value in the target image $l(x', y')$ will be marked as

$$l(x', y') = e^{-d(x', y')^2/\sigma^2} \tag{2.7}$$

where σ is a hyperparameter controlling the rate of decay. For $d(x', y') = 0$, then $l(x', y') = 1$ its maximum value. Far from the target position, the value will decay significantly. For most of the points in the heatmap, the values are close to 0. The benefits of such a design can be explained as follows. Instead of penalizing the wrong predictions equally as binary "hard labels", this "soft assignment" gives a weighted penalty to the incorrect predictions [43]. Depending how far the predicted location is away from the true location, this "soft label" can quantify the level of error and give adaptive tolerance to the wrong predictions.

Fig. 2.2 shows the effects of σ on controlling the rate of decay. We can see that if σ is small, the target is closer to binary labels. However, if σ is too large, then the target will lose its sparsity and the localization error will increase since as long as the estimated location is belong to the region which has high values, the loss will be small. In our future experiments, we choose $\sigma = 0.25$, which is a good balance for these two issues.

2.2.4 MTIT architecture

Now that we have appropriately represent the inputs and targets as images for performing localization, we utilize the image translation network architecture as shown in Fig. 2.3. One might think of using a regression network with mean square error (MSE) loss to perform the localization. However, there are two main drawbacks. First, it is difficult to deal with the data collected in different rooms. If the room dimension changes, then the size of the image will also change, leading to a different number of connections for dense layers while performing regression. Thus, to avoid all the issues related to scaling that occur because of dense layers involved during regression, we avoid using regression and stick to more scalable image translation networks

that are robust to scaling and translation. Second, simply using MSE loss does not promote the sparsity in localization. As we will see later, our network employs the regularization term in the loss function to avoid ambiguities of multiple local maxima.

We employ the encoder-decoder architecture with one encoder and two parallel decoders inspired from [36]. The intuition for using two decoders originates from MTL [27–30]. By training the network to learn multiple different tasks simultaneously, it can perform better than just learn the primary task. It can act as regularization and help the shared layers to obtain a more general representation of the input. In [30], the authors try to apply MTL in speech recognition. Although the primary task is senone classification, the feature enhancement task is also introduced. By introducing such an additional task, the network has to denoise and dereverberate the features while trying to classify them. That will help the network learn the good representations that can produce clean speech, which will reinforce the network to finish the primary task. In this work, although we are only interested in the localization as our primary task, we also include another decoder to learn how to compensate the range as our auxiliary task. By training the network to perform both tasks (i.e. two different decoders sharing the same encoder), they can improve the higher-level feature representations in the encoder. The benefit of applying MTL is that the model complexity is only increased during the training phase. During the testing phase, only the primary task is performed and the auxiliary task is discarded.

We apply the Instance Norm [44] instead of the conventional Batch Norm for the normalization in each layer. Instead of normalizing the images across the batch jointly, Instance Norm will normalize each individual image independently and it has been shown to be more successful than batch normalization in the image translation network.

The input to the encoder is the beamspectrum surface without range compensation indicated as (2). The encoder compresses this representation and then feeds to both of the decoders. The two decoders will focus on two different tasks simultaneously. The multipath alleviation decoder will focus on the auxiliary task and use the beamspectrum surface with range compen-

sation mentioned in Sec. 2.2.2 as targets to train the network to generate the beamspectrum surface without range offsets. The range offsets come from the reverberation. When the speech signal transmits from the speaker to the sensor, the shortest path (direct path) include the essential information about the locations of the source. However, in the indoor environment, the reflection is typically unavoidable and it will bring about extra travelling distance thus additional time-delays [45]. To cancel the extra time-delay, we will employ such a decoder to learn how to compensate the range. With the help of this decoder, the neural network will learn the multipath profile and how to alleviate such an artifact by range estimation. The localization decoder aims to predict the location of the sound source by using the target mentioned in Sec. 2.2.3 as labels. The output for the localization decoder is also a heatmap image with dimension $Y \times X$ (See Fig. 2.1 (d)). The location with the highest value in this output image will be marked as the predicted location. Note that since we have used the ground-truth position to generate the target images with range compensation, the multipath alleviation decoder will only appear during the training phase, and it will be turned off during the testing phase.

The loss function for the multipath alleviation decoder is l_2-loss

$$L_{multipath} = \frac{1}{N}\sum_{i=1}^{N} \|I^i_{out} - I^i_{target}\|_2 \tag{2.8}$$

where I^i_{out} and I^i_{target} are the decoder outputs and the targets (beamspectrum surfaces with range compensation) of the ith array, separately. All of the outputs and targets share the same dimension. N is the number of arrays. The advantage of averaging across multiple receiver arrays is that we can enforce consistency of peaks across all the target images, and the network will learn the consistency across these multiple receiver arrays.

For the localization decoder, we use l_2-norm loss with l_1 regularization to enforce the sparsity so that there only exists one global maxima in the output. The loss function of that

decoder can be expressed as

$$L_{localization} = \|T_{out} - T_{target}\|_2 + \lambda\|T_{out}\|_1 \tag{2.9}$$

where T_{out} and T_{target} are the decoder outputs and targets (target images with negative exponential labels), respectively. λ is the regularization term.

For each decoder, the loss is computed based on (2.8) and (2.9) and back-propagated from the output to the input of each decoder. Then, when the losses from these two decoders arrive the output of the shared encoder, they are summed and back-propagated to the network input. Since they share the same encoder, during the training phase, they will help each other to refine the weights in the encoder so that the shared representations (the input to these two decoders) are optimized. Therefore, they will help each other and the localization decoder can perform better with the help of multipath alleviation decoder.

2.3 Dataset

In this section, we will describe the four datasets we will use for the experiments including simulated data, MIRD [37], DTU [38] and SSLR [39]. For the simulated data, the RIRs are simulated by open-source software packages while for MIRD [37] and DTU [38] datasets, the RIRs are measured. The recordings are obtained via convolution between the RIRs and the "clean" audio. For SSLR [39], the recordings are obtained from real measurements.

2.3.1 Simulated Data

Simulated RIRs are synthesized by the RIR generator [46], which models the reverberation using the image method [47]. The room is 8×5 m with reverberation times (RT_{60}) from 0.4–0.8 s and speed of sound $c = 340$ m/s. RT_{60} is a parameter to reflect the level of reverberation and it

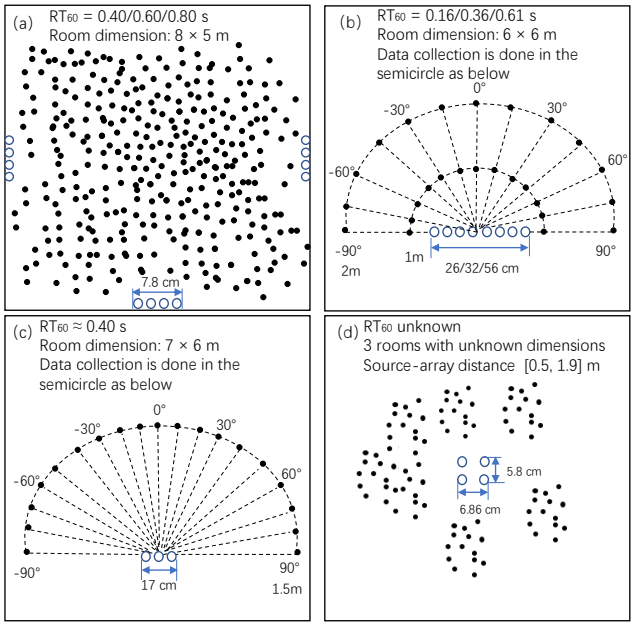

Figure 2.4: Visualization for the sources and sensors (the figure is not proportional to the actual dimensions) of (a) simulated data, (b) MIRD data, (c) DTU data and (d) SSLR data. For each figure, sources (•) and microphones (○) are shown.

is defined as the time the sound pressure level takes to decrease by 60 dB after a sound source deactivates. Therefore, the greater the RT_{60} is, the more severe the reverberation is. There are N = 3 identical ULA with array centers $(0, 2.5)$, $(4, 0)$, and $(8, 2.5)$ m and K = 4 sensors in each array with identical space 2.6 cm (See Fig. 2.4 (a)). To train the generalization across space, the sources have random (x, y) on the boundary of the room. We generate $T = 600$ RIRs with random source positions. The size of the dataset $C = 37,800$ (See Sec. 2.4 for details). The sampling frequency is 16 kHz. The input speech signal is a 1 s clean segment randomly chosen from LibriSpeech corpus [40]. Voice activity detection (VAD) is performed on all of the clean speech segments by WebRTC system. The microphone signals are obtained by convolving the RIRs with the speech signal. White noise is added to give a 20 dB signal-to-noise ratio (SNR).

2.3.2 MIRD Dataset

MIRD [37] is also utilized to evaluate the localization performance. It provides measured RIRs with 3 eight-element array apertures: 26 cm (3-3-3-8-3-3-3, the number represents the spacing between two microphone), 32 cm (4-4-4-8-4-4-4), and 56 cm (8-8-8-8-8-8-8). There are 3 different RT_{60}s (0.16, 0.36, and 0.61 s) in a 6×6 m room. We downsample to the audio frequency from 48 kHz to 16 kHz. All RT_{60}s are applied to assess the localization performance. There are 2 ranges (1 and 2 m) and 13 candidate DOAs, $[-90, 90^\circ]$ in 15° steps (See Fig. 2.4 (b)). The sound source is located in one of the 26 candidate positions. We use 20 recordings with 2 s duration and half female/male voices, resulting in $T = 520$ datapoints. The size of the dataset $C = 65,000$ (See Sec. 2.4 for details). VAD is also performed for all of the recordings.

2.3.3 DTU Dataset

We also use impulse responses measured in a classroom in Technical University of Denmark (DTU), obtained for a semi-supervised source localization study [38]. The classroom is approximately rectangular with dimension 7×6 m. However, one of the sidewalls is not regular, with a 100×40 cm extrusion across the entire wall. There are some scattering elements (like blackboards, whiteboards, diffusers and windowpanes) on all of the walls. The RT_{60} is around 400 ms. Three microphones are placed in the classroom with 8.5 cm spacing to form a ULA. The microphones are approximately in the center of the room with 4 m distance to the back wall and 3 m distance to the other walls and the height of the microphones are 1.5 m. The typical source-array distance is 1.5 m, and the DOAs are from $[-90^\circ, 90^\circ]$ with 10° resolution (See Fig. 2.4 (c)).

The DTU dataset also has off-range and off-grid RIRs. There are three off-grid RIRs with $25^\circ, 28^\circ, 45^\circ$ DOAs and 1.5 m range. The DOAs (ranges) of the off-range RIRs are 0°(1 m), 10°(2 m), 40°(2 m), -30°(2.5 m), -40°(2.5 m), and -30°(3 m). We use the 19 RIRs with 1.5 m

range, 2 RIRs with 2 m range and 1 RIR with 3 m range for training. For the testing datasets, we use 3 off-angle RIRs ($25^\circ, 28^\circ, 45^\circ$) and 3 off-range RIRs that are different from the training set (-30°(2.5 m), -40°(2.5 m) and 0°(1 m)). We use 20 recordings (after VAD) with 2 s duration and half female/male voices, resulting in $T = 560$ recordings in total. 440 of them are used for training set and the rest 120 of them are used for testing. The size of the dataset $C = 70,000$ (See Sec. 2.4 for details). The first half of the testing set is off-grid data and the second half is off-range data.

2.3.4 SSLR Dataset

For the three datasets we have mentioned above, we convolve clean speech signals with the RIRs to generate the recordings. Therefore, we assume that the room is a linear and time-invariant system such that the impulse response can characterize the room. However, in the real cases, there will be some non-linear factors (e.g. the non-linear measurement errors from the imperfections of the devices [48]) involved. Therefore, even the impulse responses are measured, they may not be enough to fully characterize the room. In this case, we try to test our method under the real recordings instead of generating the recordings by convolving clean audios with the RIRs. Therefore, the SSLR dataset [39] is used for performance evaluation.

In the SSLR dataset, the audio was transmitted from a loudspeaker and recorded by the microphones in the robot Pepper [1]. The received audio signals are strongly affected by the robot's fan noise from inside the head (ego noise). The sampling rate is 48 kHz. There are 4 microphones located at $(-0.0267, 0.0343)$, $(-0.0267, -0.0343)$, $(0.0313, 0.0343)$ and $(0.0313, -0.0343)$ on the top of the Pepper, forming a 2×2 rectangle of 5.8×6.86 cm which can be thought as two 2-element ULAs. The azimuth angle of the source is randomly distributed between $[-180^\circ, 180^\circ)$ and the source-array range is between 0.5 to 1.9 m (See Fig. 2.4 (d)). The audio is recorded in three environments: a large conference room, a small conference room and a small library room

[1] [Online]. Available: `http://doc.aldebaran.com/2-5/home_pepper.html`

Table 2.1: MAE (m) of localization for testing data (second row) and ablation study (last row) for all datasets. DTU1 and DTU2 refers to DTU off-angle and off-range testing data, respectively.

	RT_{60} (s) (Simulated)			RT_{60} (s) (MIRD)			RT_{60} (s) (DTU1)	RT_{60} (s) (DTU2)	SSLR
	.40	.60	.80	.16	.36	.61	.40	.40	/
Testing MAE (m)	**.89**	**.89**	**1.0**	**.23**	**.29**	**.39**	**.35**	**.95**	**.70**
Ablation MAE (m)	1.3	1.6	1.7	.35	.43	.59	.42	1.0	.75

Table 2.2: MAE/90$^{\text{th}}$ percentile error ($^\circ$) of DOA estimation for MTIT and other baseline methods

Method	RT_{60} (s) (Simulated)			RT_{60} (s) (MIRD)			Testing Setup (DTU)			SSLR
	.40	.60	.80	.16	.36	.61	off-angle	off-range	small	
SRP-PHAT	32/74	33/73	34/74	13/45	16/64	19/60	20/70	15/70	16/50	44/91
MUSIC	34/73	36/74	36/73	12/45	17/60	19/60	18/70	14/70	22/60	45/92
CNN	10/30	11/36	12/37	4.6/15	8.0/30	10/30	14/40	13/40	9.4/20	64/137
MTIT	**7.5/23**	**7.7/25**	**8.8/28**	**4.3/15**	**5.7/17**	**8.1/25**	**9.9/28**	**11/40**	**8.5/20**	**27/72**

with shelves. The recordings are chosen such that the array and source are almost in the same plane. There are $T = 633$ recordings (1 s length each) in total. 480 of them are used for training and the rest of them are used for validation and testing. The speech and source positions of the testing data are not seen in the training set so that it can test the generalization performance. The size of the dataset $C = 30,384$ (See Sec. 2.4 for details).

2.4 Experiments and Implementation Details

MTIT is compared with MUSIC [13], SRP-PHAT [14–16] and CNN [18]. We use the implementation of Pyroomacoustics [49] for MUSIC and SRP-PHAT. The spectrogram is used as input to train the CNN for classification. Since the source positions are random in simulation and SSLR datasets and have 15° and 10° resolution for MIRD and DTU datasets, respectively, we use 1° resolution for MUSIC and SRP-PHAT in simulations and SSLR, and 15° for MIRD and 10° for DTU dataset.

For CNN, based on the parameters suggested by [18], we have $M - 1$ (M is the number of

microphones) convolutional layers with kernel size 2, and 64 filters per layer. Then, two fully connected layers (512 units for both of them) are added following the convolutional layers. To reduce overfitting, we apply dropout (0.50 dropout rate) in output layer [18]. ReLu is used as activation function.

For simulated, MIRD and DTU data,

- We use $N_{FFT} = 256$ with no overlap for the STFT implementation, the number of snapshots $S_{sim} = 63$ and $S_{MIRD} = S_{DTU} = 125$.
- We only consider positive frequency bins, thus F is 128 for the aforementioned datasets.
- The sizes of the datasets are

  $C_{sim} = T \times S_{sim} = 600 \times 63 = 37,800$;

  $C_{MIRD} = T \times S_{MIRD} = 520 \times 125 = 65,000$;

  $C_{DTU} = T \times S_{DTU} = 560 \times 125 = 70,000$.
- The dimensions of the beamspectrum surfaces are

  $101(Y) \times 161(X)$ for simulated data;

  $121(Y) \times 121(X)$ for MIRD data;

  $121(Y) \times 141(X)$ for DTU data.

For SSLR data,

- We use $N_{FFT} = 2048$ with 50% overlapping and $S_{SSLR} = 48$.
- We only consider positive frequency bins, thus F is 1024.
- The size for that dataset is and $C_{SSLR} = T \times S_{SSLR} = 633 \times 48 = 30,384$
- The dimension of the beamspectrum surface is $41(Y) \times 41(X)$.

For MTIT, $\sigma = 0.25$ (See (2.7)) is chosen for generating the target. The beamspectrum surface is normalized by dividing the intensity of each pixel by the maximum intensity in that

Table 2.3: STOI and PESQ scores for each dataset

	Simulated Data			MIRD			DTU		SSLR
RT_{60} (s)	.40	.60	.80	.16	.36	.61	non-small	small	/
STOI	.62	.55	.49	.67	.64	.60	.82	.82	.21
PESQ	2.4	2.3	2.2	2.6	2.3	2.0	2.6	2.5	1.9

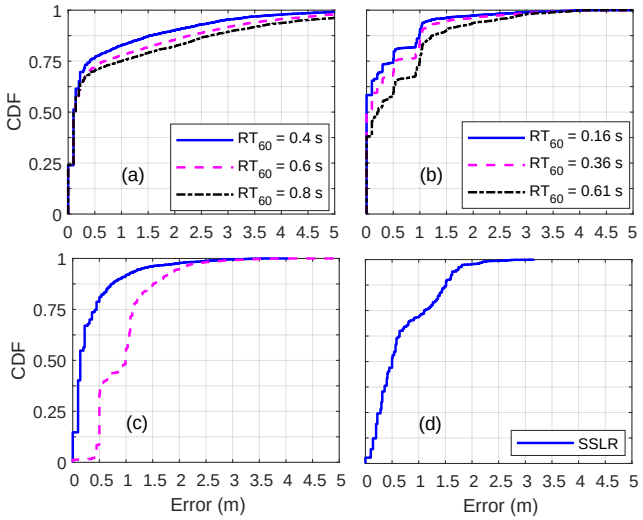

Figure 2.5: CDF of localization error for (a) simulated data, (b) MIRD data, (c) DTU data and (d) SSLR data.

image so that it is normalized between [0, 1]. The model is implemented by Pytorch [50] with learning rate 10^{-5}, batch size 32, and weight decay regularization $\lambda = 5 \times 10^{-4}$, and Adam [51] is the optimizer with weight decay 10^{-5}. The model is trained for a maximum of 50 epochs. We used early stopping based on validation localization error. We will stop the training if the validation error keeps increasing for 2 consecutive epochs.

2.5 Results and Discussions

We will use mean absolute error (MAE) and 90$^{\text{th}}$ percentile error as evaluation metrics. The localization error for ground-truth (x, y) and predicted $(\hat{x}, \hat{y})$ location can be expressed as

$$e = \sqrt{(\hat{x}-x)^2 + (\hat{y}-y)^2}\ . \tag{2.10}$$

The MAE of localization error and DOA estimation θ (the correct DOA is $\hat{\theta}$) for C datapoints are defined as

$$\text{MAE}(e) = \frac{1}{C}\sum_{c=1}^{C} e(c) \tag{2.11}$$

$$\text{MAE(DOA)} = \frac{1}{C}\sum_{c=1}^{C} |\theta(c) - \hat{\theta}(c)|. \tag{2.12}$$

The 90$^{\text{th}}$ percentile error is the worst 10% of the data. By including such an evaluation metric, we can observe the worst case for the localization performance.

We will present the localization performance of MTIT and compare the performance with baseline methods. The localization performance of MTIT for all datasets are available in Table 2.1 and Fig. 2.5. We also compare the DOA estimation error of MTIT with baseline methods and list the results in Table 2.2.

2.5.1 Testing Results

The MAE of MTIT for testing data is listed in the third row of Table 2.1. We also plot the cumulative distribution function (CDF) of the localization error for the testing data in Fig. 2.5. From Fig. 2.5, we can see that for the simulated and MIRD data, the median error is less than 0.2 m, which results in a competitive localization performance. Notice that the testing data of both DTU and SSLR are not seen during the training phase, and we can see MTIT has a good generalization performance. We will discuss more about that in Sec. 2.7.

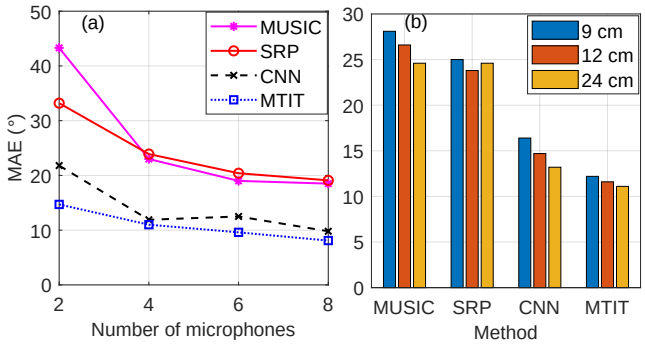

Figure 2.6: Parameter studies for (a) Number of microphones (2, 4, 6, and 8) and (b) Aperture (9, 12 and 24 cm) under MIRD data (with $M = 4$ microphones)

2.5.2 Comparison with Baseline Methods

The comparison of MAE and 90$^{\text{th}}$ percentile error for DOA estimation with other baseline methods is in Table 2.2. From these tables, we can see that our approach outperforms all baseline methods for all of the datasets.

For the SSLR data, due to the randomness of the source positions and strong robot fan noise, the localization performance of all methods degrades significantly (See Table 2.2). The results can also be attributed to the poor quality and intelligibility of the audio in SSLR dataset. We computed the short-time objective intelligibility (STOI) [52] and perceptual evaluation of speech quality (PESQ) [53] scores of each dataset (See Table 2.3). STOI is a metric to evaluate the intelligibility of the speech. It ranges from 0 to 1 and the higher STOI leads to more intelligible speech. PESQ can be used to evaluate the quality of the audio. It ranges from -0.5 to 4.5 and higher PESQ indicates the better audio quality. From the table, it is shown the strong robot fan noise adversely affects the intelligibility and quality of the audios in SSLR. However, MTIT can still have a satisfactory performance in such a harsh acoustics environment.

2.5.3 Parameter Studies

MIRD offers different microphone spacing options and for each spacing option, if we pick up half of the array (either left half or right half), it will form a ULA. In addition, for the 8

cm option, since the spacing is the same for any two adjacent microphones, regardless of how many microphones we pick up, it will form a ULA. Due to such a unique merit of MIRD, we can study the influence of number of microphones and microphone spacing on the localization performance based on that dataset.

Number of Microphones

In the previous experiments, we considered a ULA with $M = 8$ microphones with microphone spacing 8 cm. In this section, we will empirically demonstrate that based on limited number of microphones, how the localization performance will change.

In this experiment, we will consider a ULA $M = 2, 4, 6, 8$ microphones. For each case, the array is formed by selecting the M microphones starting in the middle of the array so that all of the arrays share the same inter-microphone distance. For all cases, $RT_{60} = 0.61s$

The MAE of the DOA estimation for each method is shown in Fig. 2.6 (a). For the CNN, the number of convolutional layers is set as $(M-1)$ for each case, as suggested by [18]. From the figure, we can easily find out that the localization performance will improve if the array has higher number of microphones. Therefore, for ULA, a larger aperture will result in a better performance. In addition, we observe that for the baseline methods, the MAE will decrease significantly when M increases from 2 to 4, but only slightly decrease when M is greater than 6. But MTIT can still achieve a satisfactory performance when $M = 2$, which shows the robustness against the limited number of microphones.

Influence of Microphone Spacing

In the previous experiments, we considered the ULA with 8 cm spacing. For MIRD dataset, it also provides another two apertures: 26 cm and 32 cm (See 2.3.2). In this section, we will use left half of the eight element array forming 4-element ULAs with apertures 9, 12 and 24 cm to explore the influence of the microphone spacing on the localization performance. For all of

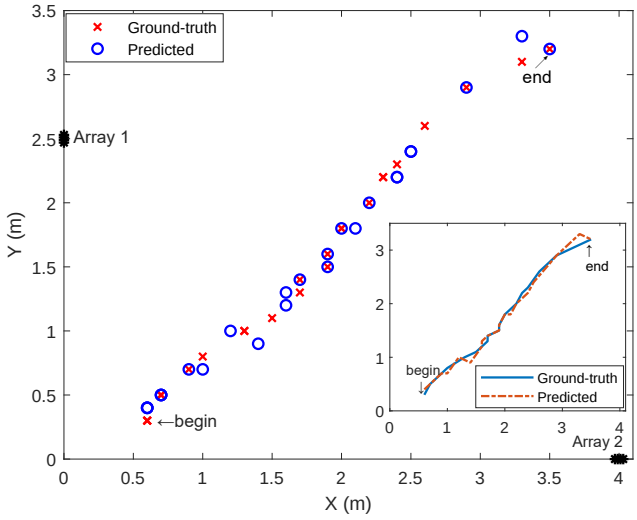

Figure 2.7: Localization results for moving sources (See Sec. 2.5.4 for details). The array 3 is not shown, and its center position is (8, 2.5) m. The ground-truth and predicted trajectory are shown in the bottom right part of the figure.

the three apertures (9, 12 and 24 cm), the RT_{60} is 0.61 s.

From Fig. 2.6 (b), for all of the methods, the best localization performance is obtained when the spacing is 8 cm, which also shows that the larger aperture will lead to a better performance.

2.5.4 Moving Source

We evaluate the localization performance for a moving source. In this experiment, we test the localization performance based on the pre-trained network under the simulated data ($RT_{60} = 0.40$ s, and SNR = 20 dB. Other parameters are described in Sec. 2.3.1.). We use RIR generator [46] to generate 25 additional RIRs from these 25 testing positions with the same setup mentioned above. The x and y coordinates of these positions range from $(0.5, 3.5]$ and $(0.3, 3.5)$, respectively. The trajectory is generated as a line with some small random perturbations (See Fig. 2.7). The source is moving from the beginning point to the end point (the begin and end points are marked in Fig. 2.7). Then, we convolve the generated RIRs with the same audio used for training to obtain the recordings polluted by reverberation. Only one snapshot is used for

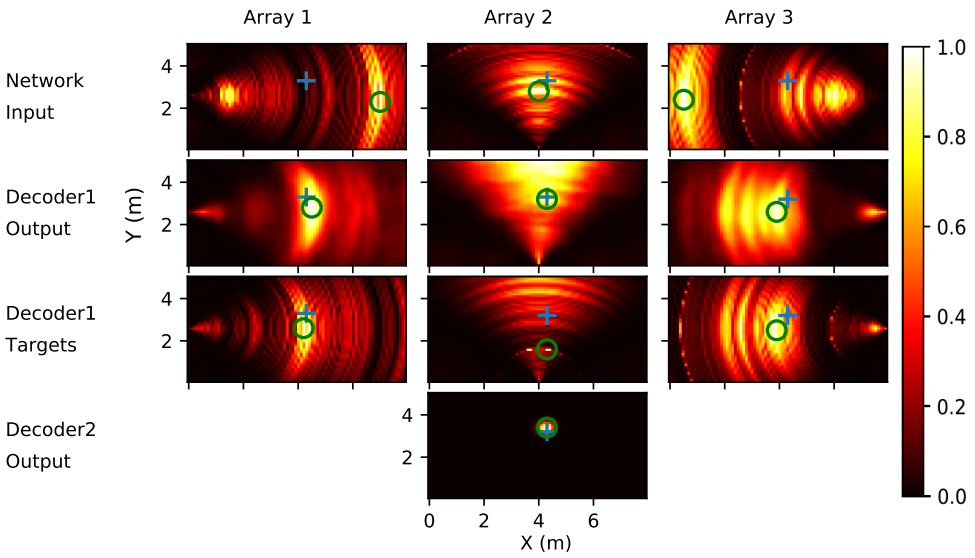

Figure 2.8: Visualization of the input, output, and target of the multipath allevation decoder (decoder 1) and the output (fourth row) of the localization decoder (decoder 2) under simulated data ($RT_{60} = 0.4$ s). The ground-truth source position (+) and the maximum point (○) are indicated.

localization. We extract the features from these recordings and generate the targets for the testing data based on the same procedure described in Sec. 2.2 and the same parameters described in Sec. 2.4. The feature heatmaps are then fed into the pre-trained network for localization. We localize these 25 positions individually and compare the localization results with the ground-truth positions (See Fig. 2.7). From the figure, we can see MTIT captures the trajectory of the moving source accurately.

2.6 Ablation Study

To validate the function of multipath alleviation decoder, we conduct ablation study which removes that decoder during the training phase. The MAEs for the testing data are listed in the second row of Table 2.1. Compared with the first row, we can see that The localization error increases when that decoder is removed for all of the cases, which verifies the role of that decoder in resolving the multipath artifacts.

To understand the role of multipath alleviation decoder, we show one example of input, output and target beamspectrum surfaces of the multipath alleviation decoder for all of the three arrays in Fig. 2.8. The example is from the *testing* data in the simulated dataset when $RT_{60} = 0.4$s. We highlight the following two observations:

2.6.1 The function of Multipath alleviation decoder

The multipath alleviation decoder is supposed to compensate the range offset caused by multipath artifacts. Let's focus on Array 1. For the input to the multipath alleviation decoder, the ground-truth position does not lie in the bright regions. Thanks to the target of that decoder which compensates the range offset, the network learns how to compensate the range and output a beamspectrum surface that is very close to the target. For Array 3, we can clearly see two local maxima in the input. But in the output of the decoder, we can see the maximum point is close to the ground-truth position. Therefore, the multipath alleviation decoder can overcome the imperfections of the input and learn how to compensate the range.

2.6.2 Evidence of Overcoming the Imperfections of the Target and Generalization

For the target of Array 2, we can see the peak is far from the ground-truth position. However, the network still overcomes such an imperfections and output an image such that the ground-truth position is close to the maximum point. Note that for this testing sample, the source position has not been seen during the training phase. Therefore, these sample images serve as an initial evidence to the generalization of MTIT. The network can even perform well when the target is not perfect.

Table 2.4: Training time (unit: mins) for 4 datasets

	Simulated Data	MIRD	DTU	SSLR
2 Decoders	308	354	371	166
1 Decoder	215	180	181	33

2.6.3 Complexity Studies

For MTIT, we introduce the auxiliary task to improve the localization performance. However, it may bring about additional computational workload in the *training* phase. Notice that the multipath alleviation decoder used for auxiliary task will be turned off during the testing phase. Hence, the auxiliary task will not increase the complexity in the *testing* phase. We compare the *training time* for MTIT in the cases when both decoders are active and only localization decoder is active (ablation case). We list the results in Table 2.4. We can see the auxiliary task indeed increases the computational workload.

2.7 Generalization Evaluation

One important assumption for the deep learning is that the training and testing data obeys the same distribution (i.e. the data are from the same environment). However, in the real applications, there will be some mismatch with the training environment. Therefore, it is crucial to evaluate the robustness of the model when the environment changes. In this section, we will comprehensively evaluate and discuss the generalization performance of our method for the four datasets under different environment changes.

2.7.1 Simulated Data

For simulated data, it is relatively easy to change the room dimension, reverberation time and SNR, so it is employed to test the generalization to unseen reverberation time and acoustic

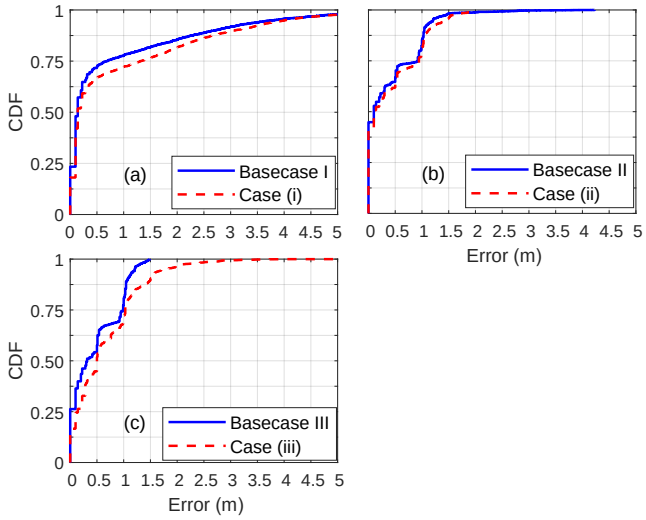

Figure 2.9: CDF of generalization experiments for (a) Base Case I (simulated data, generalization evaluation to unseen reverberation time), (b) Base Case II (MIRD data, generalization evaluation to unseen speech) and (c) Base Case III (MIRD data, generalization to unseen microphone spacing).

conditions.

Generalization to Unseen Reverberation Times

The reverberation time is a critical factor for SSL and it is determined by the room shape, the construction materials of the room, the objects placed in the room etc. Even for the same room, the reverberation times may change if the objects in the room are relocated or removed. Therefore, it is important to study the generalization to unseen reverberation times.

We train the MTIT under $RT_{60} = 0.6$ s (Base Case I) and test it under $RT_{60} = 0.7$ s (Case (i)). From Fig. 2.9 and Table 2.5, we can see that there is only a minor increase of the localization error, which shows the robustness of the model.

Generalization to Unseen Acoustics Conditions

To verify the generalization to unseen acoustics conditions, we simulate the training and testing datasets based on the configuration listed in Table 2.6. For the testing data, the RT_{60}, room

Table 2.5: Generalization performance of MTIT and CNN under simulated data (Base Case I) and MIRD data (Base Case II and III)

Training Setup	Testing Setup	MAE (°)	
		CNN	MTIT
Base Case I	Base Case I	10.8	**7.7**
Base Case I	(i)	11.7	**8.4**
Base Case II	Base Case II	9.8	**8.0**
Base Case II	(ii)	23.9	**12.0**
Base Case III	Base Case III	14.7	**11.6**
Base Case III	(iii)	25.6	**19.9**

Table 2.6: Configuration for training and testing data for generalization experiment in Sec. 2.7.1

	Training Data					Testing Data
Room Size (m)	8×5×4	9×6×4	8×6×4	10×7×4	9×5×4	8.5×5.5×4
RT_{60} (s)	.40	.60	.60	.80	.60	.70
SNR (dB)	35	25	25	15	25	20

dimension and SNR are all not seen from the training data. In addition, the positions of sound sources for the testing data are completely disjoint with that of training data. Other configurations are the same as what mentioned in 2.3.1. We compare the MAE and 90^{th} percentile error of the DOA estimation for the testing data with other baseline methods (See Table 2.7). From the table we can see that by training MTIT in a diverse set of acoustics conditions, it can generalize well to acoustic environment variation. In addition, since the positions of sources are also not seen in the training data, our method can also generalize well across space.

2.7.2 MIRD Dataset

For MIRD data, the network is trained with 20 different speech recordings, it is desirable to test whether the network has learned to be adaptive to new recordings. In addition, since it offers 3 array apertures and if we consider the left four (or the right four) sensors, it will form

Table 2.7: MAE/90$^{\text{th}}$ percentile error (°) of DOA estimation to unseen acoustics conditions and unseen source positions based on the configuration in Table 2.6

	MUSIC	SRP-PHAT	CNN	MTIT
MAE (°)	33.1	27.5	18.5	**13.7**
90% Error (°)	68.8	64.9	47.0	**34.2**

a ULA. Therefore, it may also be interesting to test whether the network can be adaptive to the unseen microphone spacing.

Generalization to Unseen Speech

It is also essential to ensure the model can generalize to different speech so that it can adapt well to arbitrary speakers. To verify the generalization to unseen speech, we pick up 3 recordings that are different from the training set and re-generate the testing data. The model is trained on $M = 8$ ULA (8 cm spacing) with $RT_{60} = 0.61$ s and 20 speech signals but tested with 3 recordings that are seen (Basecase II) or not seen (Case (ii)) from the training set. The MAEs of the DOA estimation are listed in Table 2.5. We can see that CNN is sensitive to the unseen speech and the MAE of the localization increases significantly for the new testing data. However, such a change does not seriously influence the localization performance of MTIT, which shows the potential for generalization to different speech.

Generalization to Unseen Microphone Spacing

In this section, we will use half of the eight element array ($M = 4$ ULA) and two spacings (3 cm or 4 cm) to evaluate the generalization to unseen microphone spacing. The model is trained based on 4 cm aperture (Basecase III) but tested on 3 cm aperture (Case (iii)). From Table 2.5, we can see that MTIT is more robust to the unseen microphone spacing than the CNN.

2.7.3 DTU Dataset

Although DTU and MIRD datasets are similar in that both of them are measured RIRs, DTU dataset offers off-grid and small-device measurements. Hence, it can be used to test the generalization across unseen source positions and measurement devices.

Generalization across Space

There are two sets of testing data (off-angle and off-range) in the DTU dataset (See 2.3.2). From Table 2.2, we can see that our method has a superior performance than the baseline methods. Therefore, MTIT can generalize well to unseen source positions.

Generalization across Devices

When we are doing the measurements, the sound sources were played by two type of loudspeakers including a compact loudspeaker (single-driver) and a full-range loudspeaker (two-way). To verify the generalization across devices, we train the model under the RIRs collected from full-range loudspeaker and test it by the data from compact loudspeaker. It can be seen from Table 2.2 that MTIT performs well under different measurement devices.

2.7.4 SSLR Dataset

For all of the datasets mentioned above, the recordings are obtained by convolving the RIRs with "clean" speech signals, which means that we assume the room is a linear system. So it may be necessary to include the real recordings to double check whether the network can still generalize well under a non-linear system. SSLR is therefore used to test the generalization across speech and space under non-linear system though we have tested them in MIRD and DTU datasets.

For the SSLR dataset, the speech recordings and source positions are not seen during the

training. Based on the superior performance shown in Table 2.2, we can conclude that MTIT has a good generalization performance in the presence of ego noise etc.

2.8 Conclusions

We developed MTIT, a SSL method based on MTL and image translation network. This enables the DNN to simultaneously predict the locations of sound sources and mitigate multipath artifacts. Since they share the same encoder, these two decoders will help each other during the training stage. Experiments indicate our method outperforms MUSIC, SRP-PHAT, and CNN in environments in all of the four datasets we used. The ablation study shows the importance of multipath alleviation decoder to reduce multipath and the generalization experiments show strong generalization abilities and robustness against the mismatch between the training and testing data.

Acknowledgement

The text of this chapter is in full reprint of the material as it appears in Yifan Wu, Roshan Ayyalasomayajula, Michael J. Bianco, Dinesh Bharadia and Peter Gerstoft, ”Sound Source Localization based on Multi-task Learning and Image Translation Network,” *Journal of the Acoustical Society of America*, 150, 3374-3386. The dissertation author was the primary researcher and author of this chapter. The co-authors listed in these publications directed and supervised the research.

Bibliography

[1] K. Nakadai, T. Lourens, H. G. Okuno, and H. Kitano, “Active audition for humanoid,” in *Proc. Natl. Conf. Artif. Intell.* (2000), pp. 832–839.

[2] Z. Li, B. Huang, Z. Ye, M. Deng, and C. Yang, “Physical human–robot interaction of a

robotic exoskeleton by admittance control," IEEE Trans. Ind. Electron. **65**(12), 9614–9624 (2018).

[3] Y. Wang and H. Peng, "Underwater acoustic source localization using generalized regression neural network," J. Acoust. Soc. Am. **143**(4), 2321–2331 (2018).

[4] H. Niu, E. Reeves, and P. Gerstoft, "Source localization in an ocean waveguide using supervised machine learning," J. Acoust. Soc. Am. **142**(3), 1176–1188 (2017).

[5] F. Strasser and H. Puder, "Adaptive feedback cancellation for realistic hearing aid applications," IEEE/ACM Trans. Audio, Speech, and Lang. Process. **23**(12), 2322–2333 (2015).

[6] S. Pradhan, V. Patel, D. Somani, and N. V. George, "An improved proportionate delayless multiband-structured subband adaptive feedback canceller for digital hearing aids," IEEE/ACM Trans. Audio, Speech, and Lang. Process. **25**(8), 1633–1643 (2017).

[7] S. Zhao, S. Ahmed, Y. Liang, K. Rupnow, D. Chen, and D. Jones, "A real-time 3D sound localization system with miniature microphone array for virtual reality," in *Proc. IEEE ICIEA* (2012), pp. 1853–1857.

[8] Z. Wang and D. Wang, "A joint training framework for robust automatic speech recognition," IEEE/ACM Trans. Audio, Speech, and Lang. Process. **24**(4), 796–806 (2016).

[9] D. Baby, T. Virtanen, J. F. Gemmeke, *et al.*, "Coupled dictionaries for exemplar-based speech enhancement and automatic speech recognition," IEEE/ACM Trans. Audio, Speech, and Lang. Process. **23**(11), 1788–1799 (2015).

[10] P. Gerstoft, Y. Hu, M. J. Bianco, C. Patil, A. Alegre, Y. Freund, and F. Grondin, "Audio scene monitoring using redundant ad-hoc microphone array networks," IEEE Internet Things J. (2021).

[11] S. Argentieri, P. Danès, and P. Souères, "A survey on sound source localization in robotics: From binaural to array processing methods," Computer Speech & Language **34**(1), 87–112 (2015).

[12] M. J. Bianco, P. Gerstoft, J. Traer, E. Ozanich, M. A. Roch, S. Gannot, and C.-A. Deledalle, "Machine learning in acoustics: Theory and applications," J. Acoust. Soc. Am. **146**(5), 3590–3628 (2019).

[13] R. O. Schmidt, "Multiple emitter location and signal parameter estimation," IEEE Trans. Antennas Propagat. **34**(3), 276–280 (1986).

[14] J. Dmochowski, J. Benesty, and S. Affes, "A generalized steered response power method for computationally viable source localization," IEEE/ACM Trans. Audio, Speech, Lang. Process. **15**(8), 2510–2526 (2007).

[15] M. S. Brandstein and H. F. Silverman, "A robust method for speech signal time-delay estimation in reverberant rooms," in *IEEE ICASSP* (1997), Vol. 1, pp. 375–378.

[16] D. Yook, T. Lee, and Y. Cho, "Fast sound source localization using two-level search space clustering," IEEE Trans. Cybern. **46**(1), 20–26 (2015).

[17] X. Xiao, S. Zhao, X. Zhong, D. Jones, E. S. Chng, and H. Li, "A learning-based approach to direction of arrival estimation in noisy and reverberant environments," in *IEEE ICASSP* (2015), pp. 2814–2818.

[18] S. Chakrabarty and E. A. P. Habets, "Multi-speaker DOA estimation using deep convolutional networks trained with noise signals," IEEE J. Sel. Topics Signal Process. **13**(1), 8–21 (2019).

[19] J. M. Vera-Diaz, D. Pizarro, and J. Macias-Guarasa, "Acoustic source localization with deep generalized cross correlations," Signal Process. (2021).

[20] S. Adavanne, A. Politis, J. Nikunen, and T. Virtanen, "Sound event localization and detection of overlapping sources using convolutional recurrent neural networks," IEEE J. Sel. Topics Signal Process. **13**(1), 34–48 (2018).

[21] Z. Q. Wang, X. Zhang, and D.-L. Wang, "Robust speaker localization guided by deep learning-based time-frequency masking," IEEE/ACM Trans. Audio, Speech, Lang. Process. **27**(1), 178–188 (2018).

[22] N. Liu, H. Chen, K. Songgong, and Y. Li, "Deep learning assisted sound source localization using two orthogonal first-order differential microphone arrays," J. Acoust. Soc. Am. **149**(2), 1069–1084 (2021).

[23] R. Takeda and K. Komatani, "Unsupervised adaptation of deep neural networks for sound source localization using entropy minimization," in *IEEE ICASSP* (2017), pp. 2217–2221.

[24] B. Laufer-Goldshtein, R. Talmon, and S. Gannot, "Semi-supervised sound source localization based on manifold regularization," IEEE/ACM Trans. Audio, Speech, and Lang. Process. **24**(8), 1393–1407 (2016).

[25] M. J. Bianco, S. Gannot, E. Fernandez-Grande, and P. Gerstoft, "Semi-supervised source localization in reverberant environments with deep generative modeling," IEEE Access (2021).

[26] Y. Wu, R. Ayyalasomayajula, M. J. Bianco, D. Bharadia, and P. Gerstoft, "Sslide: Sound source localization for indoors based on deep learning," in *IEEE ICASSP* (2021), pp. 4680–4684.

[27] R. Caruana, "Multitask learning," Machine learning **28**(1), 41–75 (1997).

[28] S. Ruder, "An overview of multi-task learning in deep neural networks," arXiv preprint arXiv:1706.05098 (2017).

[29] Y. Zhang and Q. Yang, "A survey on multi-task learning," arXiv preprint arXiv:1707.08114 (2017).

[30] R. Giri, M. L. Seltzer, J. Droppo, and D. Yu, "Improving speech recognition in reverberation using a room-aware deep neural network and multi-task learning," in *IEEE ICASSP* (2015), pp. 5014–5018.

[31] H. M. Alonso and B. Plank, "When is multitask learning effective? semantic sequence prediction under varying data conditions," arXiv preprint arXiv:1612.02251 (2016).

[32] J. Yim, H. Jung, B. Yoo, C. Choi, D. Park, and J. Kim, "Rotating your face using multi-task deep neural network," in *IEEE CVPR* (2015), pp. 676–684.

[33] J. Johnson, A. Alahi, and L. Fei-Fei, "Perceptual losses for real-time style transfer and super-resolution," in *ECCV*, Springer (2016), pp. 694–711.

[34] J. Zhu, T. Park, P. Isola, and A. A. Efros, "Unpaired image-to-image translation using cycle-consistent adversarial networks," in *IEEE ICCV* (2017), pp. 2223–2232.

[35] K. Zhang, W. Zuo, Y. Chen, D. Meng, and L. Zhang, "Beyond a gaussian denoiser: Residual learning of deep cnn for image denoising," IEEE Trans. Image Process. **26**(7), 3142–3155 (2017).

[36] R. Ayyalasomayajula, A. Arun, C. Wu, S. Sharma, A. Sethi, D. Vasisht, and D. Bharadia, "Deep learning based wireless localization for indoor navigation," in *ACM MobiCom* (2020), pp. 1–14.

[37] E. Hadad, F. Heese, P. Vary, and S. Gannot, "Multichannel audio database in various acoustic environments," in *Proc. Int. Workshop Acoust. Signal Enh.* (2014), pp. 313–317.

[38] E. Fernandez-Grande, M. J. Bianco, S. Gannot, and P. Gerstoft, "DTU three-channel room impulse response dataset for direction of arrival estimation 2020," (2021), `https://dx.doi.org/10.21227/c5cn-jv76`, doi: `10.21227/c5cn-jv76`.

[39] W. He, P. Motlicek, and J. Odobez, "Deep neural networks for multiple speaker detection and localization," in *IEEE ICRA* (2018), pp. 74–79.

[40] V. Panayotov, G. Chen, D. Povey, and S. Khudanpur, "Librispeech: an asr corpus based on public domain audio books," in *IEEE ICASSP* (2015), pp. 5206–5210.

[41] R. Ayyalasomayajula, D. Vasisht, and D. Bharadia, "BLoc: CSI-based accurate localization for BLE tags," in *Int. Conf. Emerg. Netw. Exp. Technol. (CoNext)* (2018), pp. 126–138.

[42] P. A. Grumiaux, S. Kitić, L. Girin, and A. Guérin, "A review of sound source localization with deep learning methods," arXiv preprint arXiv:2109.03465 (2021).

[43] R. Diaz and A. Marathe, "Soft labels for ordinal regression," in *IEEE CVPR* (2019), pp. 4738–4747.

[44] D. Ulyanov, A. Vedaldi, and V. Lempitsky, "Instance normalization: The missing ingredient for fast stylization," arXiv preprint arXiv:1607.08022 (2016).

[45] S. Shen, D. Chen, Y. Wei, Z. Yang, and R. R. Choudhury, "Voice localization using nearby wall reflections," in *ACM Mobicom* (2020), pp. 1–14.

[46] E. A. P. Habets, "Room Impulse Response (RIR) generator," (Online) Available: https://github.com/ehabets/RIR-Generator (2016).

[47] J. B. Allen and D. A. Berkley, "Image method for efficiently simulating small-room acoustics," J. Acoust. Soc. Am. **65**(4), 943–950 (1979).

[48] Y. Kaneda, "A study of non-linear effect on acoustic impulse response measurement," J. Acoust. Soc. Jpn. (E) **16**(3), 193–195 (1995).

[49] R. Scheibler, E. Bezzam, and I. Dokmanić, "Pyroomacoustics: A python package for audio room simulation and array processing algorithms," in *IEEE ICASSP* (2018), pp. 351–355.

[50] A. Paszke, S. Gross, F. Massa, A. Lerer, and J. B. et al., "Pytorch: An imperative style, high-performance deep learning library," in *Adv. Neural Info. Process. Sys* (2019), pp. 8026–8037.

[51] D. P. Kingma and J. Ba, "Adam: A method for stochastic optimization," arXiv preprint arXiv:1412.6980 (2014).

[52] C. H. Taal, R. C. Hendriks, R. Heusdens, and J. Jensen, "An algorithm for intelligibility prediction of time–frequency weighted noisy speech," IEEE/ACM Trans. Audio, Speech, and Lang. Process. **19**(7), 2125–2136 (2011).

[53] A. W. Rix, J. G. Beerends, M. P. Hollier, and A. P. Hekstra, "Perceptual evaluation of speech quality (pesq)-a new method for speech quality assessment of telephone networks and codecs," in *IEEE ICASSP* (2001), Vol. 2, pp. 749–752.

Chapter 3

Gridless DOA Estimation with Multiple Frequencies

Direction-of-arrival (DOA) estimation is widely applied in acoustic source localization. A multi-frequency model is suitable for characterizing the broadband structure in acoustic signals. In this paper, the *continuous* (gridless) DOA estimation problem with multiple frequencies is considered. This problem is formulated as an atomic norm minimization (ANM) problem. The ANM problem is equivalent to a semi-definite program (SDP) which can be solved by an off-the-shelf SDP solver. The dual certificate condition is provided to certify the optimality of the SDP solution so that the sources can be localized by finding the roots of a polynomial. We also construct the dual polynomial to satisfy the dual certificate condition and show that such a construction exists when the source amplitude has a uniform magnitude. In multi-frequency ANM, spatial aliasing of DOAs at higher frequencies can cause challenges. We discuss this issue extensively and propose a robust solution to combat aliasing. Numerical results support our theoretical findings and demonstrate the effectiveness of the proposed method.

3.1 Introduction

Line spectrum estimation is a fundamental problem in signal processing, and has many applications in direction-of-arrival (DOA) estimation in sensor array processing [1], wideband channel estimation [2], and modern imaging modalities [3]. In line spectrum estimation, the observed signal $x[n]$ is a superposition of K complex sinusoids (i.e. $x[n] = \sum_{k=1}^{K} c_k e^{-j2\pi f_k n}$) and the goal is estimating the frequencies f_k of these K sinusoids. An important application of line spectrum estimation is DOA estimation [1]. For DOA estimation, we have K plane waves from angles $\{\theta_1, \ldots, \theta_K\}$ impinging on an array with N_m sensors. Due to different propagation delays to each sensor, the received data is a sum of K spatial sinusoid vectors $[1 \ \ldots \ e^{-j\frac{2\pi f_0 (N_m-1) d\cos\theta_k}{c}}]^T (k \in \{1, \ldots, K\})$ parameterized by the plane wave directions θ_k (f_0 is a temporal frequency). Our goal is to estimate the K DOAs (θ_k) based on the received data. The cosine of each DOA linearly maps to a single spatial frequency $\frac{2\pi f_0 d\cos\theta_k}{c}$ of the sinusoid, and once the spatial frequencies are estimated, the DOA can be retrieved. Many line spectrum estimation methods as multiple signal classification (MUSIC) [4], and estimation of signal parameters via rotational invariant techniques (ESPRIT) [5], have been used for narrow band signals.

Unfortunately, the aforementioned methods cannot be applied in wideband DOA estimation problems such as ocean acoustics localization and speaker localization. Wideband signal DOA estimation has been studied for decades [6–10]. A subspace-based wideband DOA estimation approach, incoherent signal subspace method [6], was proposed with later improvement in the coherent signal subspace method (CSSM) [7]. A broadband spatial-spectrum estimation approach [8] overcame the peak bias and source spectral content sensitivity from CSSM. Variants of CSSM, such as the weighted average of signal subspaces method [9], and the test of orthogonality of projected subspaces method [10] were also proposed. Recently, some wideband DOA estimation methods based on sparse recovery have also been developed [11–14]. These sparsity-based methods have demonstrated superior performance compared to conventional methods.

The multi-frequency (or multi-dictionary) model [14–18] has shown success in modeling wideband signals. The multi-frequency model uses N_f (rather than 1) temporal frequency bins in a frequency set $\mathcal{F} = \{f_1, \ldots, f_{N_f}\}$ to characterize a wideband signal. These frequencies are then used for estimation, as opposed to using a single frequency under the narrowband model. The multi-frequency model was used for ocean acoustics localization [18]. Most of the existing methods assume that the true spatial frequencies lie on a finite set of grid points, and their performance may degrade if the true spatial frequencies fall off the grid.

To overcome the grid mismatch problem, atomic norm minimization (ANM) methods that work on continuous (gridless) dictionaries have been proposed in a variety of contexts [19–32]. ANM extends grid-based, sparsity-promoting ℓ_1 norm minimization to the continuous setting and is commonly applied to solve the line spectrum estimation problem for signals that are sparse in the temporal frequency domain. ANM was initially proposed in [19], which provides a general recipe for finding convex solutions to promote sparse decompositions, where one seeks to represent a given signal based on a minimal number of atoms from an atomic set composed of an ensemble of signal atoms. The ANM framework overcomes the grid mismatch issue and can achieve potentially infinite precision. However, all prior ANM works used a narrowband assumption and are not applicable for wideband DOA estimation.

3.1.1 Related Work

Multiple Frequencies

Multiple frequencies decompose a wideband signal into multiple narrowband signals and therefore are widely applied in acoustics source localization [15, 16, 18] when the signal contains a wide range of frequency bins and cannot be characterized by a narrowband model. Some grid-based sparse localization approaches for the multiple frequencies were proposed [14, 15, 17, 18, 33] for robustness and aliasing suppression.

Atomic Norm Minimization

ANM was initially proposed in [19] as a general framework for promoting sparse signal decompositions. The pioneering ANM paper [20] worked directly with the continuous (temporal) frequency estimation problem and considered the complete data case. As long as the temporal frequency separation was greater than a certain minimum separation, exact recovery of the active temporal frequencies was guaranteed. Furthermore, a semidefinite programming (SDP) framework that characterized the ANM problem was presented. The authors in [21] studied continuous temporal frequency estimation based on randomly sampled data for the single measurement vector (SMV) case. The minimum separation condition was relaxed in [24]. ANM for multiple measurement vectors (MMVs) was studied in [23, 26, 30]. In [25], the author considered a super-resolution problem that had a similar setup to [20] except that the point spread function was assumed to be unknown. Based on the assumption that the point spread function was stationary and lived in a known subspace, the lifting trick was applied, and the problem was formulated using ANM. The model was generalized to non-stationary point spread functions in [27]. The sample complexity of modal analysis with random temporal compression was established in [28]. ANM for 2D temporal frequency estimation was studied in [22]. In [29], the authors proposed a reweighted ANM framework, which enhances the sparsity and achieves super-resolution. An atomic norm for DOA estimation under gain-phase noise [34] was proposed to mitigate the artifacts for electromagnetic signals. ANM was also recently applied in digital beamforming [35, 36], adaptive interference cancellation [37], denoising [38, 39], and blind demodulation [40, 41]. We refer readers to [42] for a comprehensive overview of ANM and its applications.

Our multi-frequency problem is different from the MMV problems [23, 26, 30] extensively studied in the past few years. Although both our work and MMVs fall under the general topic of multi-channel line spectrum estimation, the temporal frequencies in each channel are different in our problem while they are the same in MMVs. Therefore, each channel is modulated with a different sinusoid while this *heterogeneous* modulation is absent in MMVs. This heterogeneous

modulation leads to several challenges for theoretical analysis. First, it makes it difficult to derive an equivalent SDP problem based on the Vandermonde decomposition as has been done in many prior ANM works. Second, under our setup, each frequency other than the first will experience spatial aliasing of the DOAs. This leads to potential collisions or near collisions of the DOAs which are challenging to resolve. Thus, although having multiple frequencies does provide more data, one must ensure that aliasing does not undermine this benefit. These challenges make our problem more difficult to analyse than MMV problems. We will elaborate on these two challenges and our solutions in Sec. 3.1.2.

3.1.2 Our Contributions

In this work, we extend ANM to the multi-frequency framework so that it can be used for DOA estimation with wideband signals. Our contributions are summarized as follows:

(1) Formulate an equivalent SDP problem. Although ANM itself is a convex optimization problem, it is not directly solvable due to an infinite number of optimization parameters. Therefore, it is critical to find a computationally feasible solution that equivalently characterizes the ANM problem. Several prior works showed that certain ANM problems could be equivalently characterized by SDPs [21, 23, 26]. The derivation of an SDP problem typically relies on a Vandermonde decomposition, and equivalence with the ANM can be proved by showing that the SDP solution is both an upper and a lower bound for the ANM [21, 23, 26]. Unfortunately, this commonly used technique cannot be applied in our case due to the heterogeneous temporal frequencies across different channels. In [35, 43], certain SDPs were derived using the Vandermonde decomposition, but only the lower bound for the ANM problem could be guaranteed. In this work, we derive an equivalent SDP based on the bounded real lemma for trigonometric polynomials [44]. This equivalent SDP will provide a computationally feasible solution for the ANM when multiple frequencies are considered. We also explain how our SDP is the dual to a minor adaptation of the SDP proposed in [45] for line spectrum estimation with harmonics.

(2) Provide the dual certificate condition. We derive a dual certificate condition that can be used to certify the optimal atomic decomposition. In particular, the DOAs of the sources are localized with the help of the dual polynomial arising from the ANM optimization problem. As long as the dual polynomial satisfies the dual certificate condition, the frequencies can be localized by finding the roots of a polynomial. Therefore, the dual certificate condition not only provides a theoretical guarantee for the optimality, but also offers a method for the DOA estimation.

(3) Construct the dual polynomial that satisfies the dual certificate condition. In cases where we can prove the existence of a dual polynomial that satisfies the dual certificate condition, then the optimality and therefore exact DOA estimation are guaranteed. If the array spacing $d \leq \frac{c}{2N_f f_0} = \frac{\lambda_{N_f}}{2}$, spatial aliasing would be fully avoided for all of the temporal frequencies, and it may be possible to construct a valid dual polynomial under a mild separation assumption on the source directions. In such a case, the success of the algorithm is guaranteed.

The dual polynomial is developed our model for arbitrary spacing d. A larger aperture $(N_m - 1)d$ with greater d may improve spatial resolution but introduces spatial aliasing. If the spacing $d = \frac{c}{2f_0} = \frac{\lambda_1}{2}$, spatial aliasing is present in all but the first frequency. This spacing necessarily creates periodicity in all but the first frequency of the vector-valued dual polynomial. Such periodicity brings the risk of creating ambiguity in the source direction. More specifically, after spatial aliasing, when two source directions coincide at one frequency, we refer to this as *collision*. Collision may happen in multiple frequency bins, and it becomes more likely for great N_f. Most ANM works need well-separated harmonics to work [20, 21, 23, 26]. However, in a multi-frequency scenario, one must consider the separations for DOAs across all frequencies. Assuming collisions and near collisions are thus avoided and under some additional assumptions about the source amplitudes, we guarantee that there exists a dual polynomial satisfying the dual certificate condition.

(4) Implementation. We propose a fast implementation so that the SDP has a reduced size. This fast implementation also extends the approach to an arbitrary set of frequencies. Numerical

results show that the dual polynomial still serves as a precise indicator for the DOAs. Hence, in terms of the DOA estimation, the algorithm succeeds even when collisions are present.

Finally, our work is inspired by recent advances in ANM for super-resolution, but significantly deviates from the existing MMV works. This work significantly extends our previous ICASSP paper [46]. It includes additional analysis for the dual polynomial construction, aliasing and collision, and provides a fast algorithm and extensive simulations. This paper is the first work that extends ANM to multiple frequencies so that it can be adapted to *gridless* DOA estimation for wideband signals via convex programming.

3.1.3 Notations and Organization

Boldface letters represents matrices and vectors. Conventional notations $(\cdot)^T$, $(\cdot)^H$, $(\cdot)^*$, $\langle\cdot\rangle_{\mathbb{R}}$, and $\langle\cdot\rangle$ stand for matrix/vector transpose, Hermitian transpose, complex conjugate, real inner product, and inner product, respectively. $\mathrm{Tr}(\cdot)$ is used to represent the trace of a matrix. $\|\cdot\|_p$ and $\|\cdot\|_F$ are used to express vector ℓ_p norm and matrix Frobenius norm. For a Hermitian matrix $\mathbf{A}$, $\mathbf{A} \succeq 0$ means $\mathbf{A}$ is a positive semidefinite (PSD) matrix. $\odot$ stands for the Hadamard product. The $\ell_{1,2}$ norm of a matrix $\mathbf{A} = [\mathbf{a}_1 \ \ldots \ \mathbf{a}_N]$ is defined as $\|\mathbf{A}\|_{1,2} := \sum_{i=1}^{N} \|\mathbf{a}_i\|_2$. The imaginary unit is denoted by $j = \sqrt{-1}$.

The rest of the paper is organized as follows. Sec. 3.2 introduces the signal model and the assumptions. The equivalent SDP and the dual certificate condition are derived in Sec. 3.3. Sec. 3.4 constructs the dual polynomial that satisfies the dual certificate condition and also analyses the collision and near collision issues. Sec. 3.5 presents some numerical examples to support and demonstrate theoretical findings. Finally, Sec. 3.6 concludes the paper.

3.2 Signal Model

3.2.1 Assumptions and Model Framework

Assumptions

The following assumptions are made for the array configuration and signal model:

1. There are N_m sensors forming a uniform linear array (ULA) with array spacing d.

2. There are K active sources impinging on the array from unknown directions of arrival (DOAs) θ.

3. Each source has N_f active temporal frequency components, each at an integer multiple f of a fundamental frequency f_0, i.e., $f \in \{1,\ldots,N_f\}$ and $ff_0 \in \{f_0,\ldots,N_f f_0\}$. This is only a technical assumption to simplify the analysis, and our method can be applied in any frequency set with the fast algorithm proposed in Sec. 3.3.6.

4. Suppose $d \leq \frac{c}{2f_0}$ holds (or, equivalently, $\frac{2\pi f_0 d}{c} \leq \pi$), where c is the speed of propagation. We also notice that $d = \frac{c}{2f_0}$ is the maximum separation to avoid spatial aliasing at the fundamental frequency. For higher frequencies (i.e. $f \geq 2$), aliasing will still exist. Such aliasing is not considered in conventional narrowband ANM papers. It is possible to develop the method with $d = \frac{c}{2N_f f_0}$ so that aliasing can be completely avoided in all frequencies.

Multiple Frequencies

Based on the above assumptions, we absorb the constant parameters d, f_0, and c into a scaled DOA parameter $w = w(\theta) := \frac{f_0 d\cos(\theta)}{c} \in [-f_0 d/c, f_0 d/c]$. Henceforth, w is simply referred as the DOA.

For each temporal frequency $ff_0 \in \{1,\ldots,N_f\}\cdot f_0$, let $\mathbf{y}_f \in \mathbb{C}^{N_m}$ denote the received signal across the N_m sensors. $\mathbf{y}_f$ can be expressed as a sum of K spatial sinusoid vectors, with

the k-th vector having spatial frequency $fw(\theta_k)$. Importantly, the spatial frequency depends on both the temporal frequency ff_0 and the DOA $w(\theta_k)$. To better illustrate these effects, we refer the reader to Fig. 3.1. Suppose $N_f = 3$, $N_m = 5$, and the input signal (top row) is a complex sinusoid with temporal frequency ff_0. The spatial samples obtained from the sensors (red) will be sampled sinusoids (bottom row) with different spatial frequencies that depend on both the temporal frequency and the DOA.

Stacking all of the data from the N_f frequencies into a matrix, the full set of received data is denoted by $\mathbf{Y} := [\mathbf{y}_1 \ \dots \ \mathbf{y}_{N_f}] \in \mathbb{C}^{N_m \times N_f}$. Summing over the K active DOAs, we write

$$\mathbf{Y} = \mathbf{X} + \mathbf{W}, \tag{3.1}$$

where

$$\begin{aligned} \mathbf{X} &:= \sum_w c_w [x_w(1)\mathbf{a}(1,w) \ \dots \ x_w(N_f)\mathbf{a}(N_f,w)] \\ &= \sum_w c_w \mathbf{A}(w) \circledast \mathbf{x}_w^T, \end{aligned} \tag{3.2}$$

$\mathbf{a}(f,w) := [1 \ \dots \ e^{-j2\pi w f(N_m-1)}]^T \in \mathbb{C}^{N_m}$ is the array manifold vector (steering vector) corresponding to the f-th frequency bin and DOA w, $x_w(f)$ is the signal amplitude for the f-th frequency bin, and $\mathbf{W} := [\mathbf{w}_1, \dots, \mathbf{w}_{N_f}] \in \mathbb{C}^{N_m \times N_f}$ is additive Gaussian uncorrelated noise. $\mathbf{x}_w := [x_w(1) \ \dots \ x_w(N_f)]^T \in \mathbb{C}^{N_f}$ is a collection of N_f amplitudes corresponding to the same DOA, $\mathbf{A}(w) := [\mathbf{a}(1,w) \ \dots \ \mathbf{a}(N_f,w)] \in \mathbb{C}^{N_m \times N_f}$, and $\circledast$ is the Khatri-Rao product defined as $[\mathbf{A}(w) \circledast \mathbf{x}_w^T] := [\mathbf{a}(1,w)x_w(1) \ \dots \ \mathbf{a}(N_f,w)x_w(N_f)] \in \mathbb{C}^{N_m \times N_f}$. We assume that $\|\mathbf{x}_w\|_2 = 1$; the coefficient c_w absorbs any other scaling of the source amplitudes $c_w\mathbf{x}_w$. Our goal is to identify the K active DOAs w from the data matrix $\mathbf{Y}$.

In the following sections, we primarily develop the optimization methods within the noise-free model, i.e., where $\mathbf{W} = \mathbf{0}$. We describe, however, how the optimization problem is modified if noise is present (see (3.10) and (3.21)).

3.2.2 Mapping Operator

In this section, we will define some mapping operators that help us set up our method. Define

$$\begin{aligned}\mathbf{z} = \mathbf{z}(w) &:= [1 \quad e^{-j2\pi w1} \dots e^{-j2\pi w N_f(N_m-1)}]^T \\ &= [z^0 \quad z^1 \dots z^{N-1}]^T \in \mathbb{C}^N\end{aligned} \tag{3.3}$$

that collects all possible complex exponentials from the array manifolds in all frequencies, where $N := N_f(N_m-1)+1$ and $z = z(w) := e^{-j2\pi w}$. The intuition for defining the $\mathbf{z}$ notation will be explained after the definition of the dual polynomial vector (3.13). Introduce $\mathbf{Z} = \mathbf{Z}(w) := [\mathbf{z} \dots \mathbf{z}] \in \mathbb{C}^{N\times N_f}$ and define $\mathbf{X}' \in \mathbb{C}^{N\times N_f}$ as

$$\mathbf{X}' := \left(\sum_w c_w \mathbf{Z} \circledast \mathbf{x}_w^T\right). \tag{3.4}$$

Then, we define the $\mathcal{R}$ operator that maps $\mathbf{X}'$ to $\mathbf{X}$ as

$$\mathbf{X} = \mathcal{R}(\mathbf{X}') \Rightarrow \mathbf{X}(i,j) = \mathbf{X}'(1+(i-1)j, j), \tag{3.5}$$

where $\mathcal{R} : N \times N_f \to N_m \times N_f$ is a mapping that selects N_m elements from the N elements in each column of $\mathbf{X}'$. We demonstrate the mapping in Fig. 3.2. Note that $\mathbf{A}(w)$ can be represented in terms of $\mathbf{Z}$ by using the $\mathcal{R}$ operator as

$$\mathbf{A}(w) = \mathcal{R}(\mathbf{Z}). \tag{3.6}$$

Note that in [45, (8)], an analogous mapping operator is introduced in the context of the line spectrum estimation problem with harmonics. In [45, (9)], the transformation is applied in the signal space and enables the formulation of an SDP problem in the primal domain. In our paper, $\mathcal{R}$ is applied to the coefficient matrix $\mathbf{H}$ (see (3.15)) and that enables us to formulate an SDP problem in the dual domain.

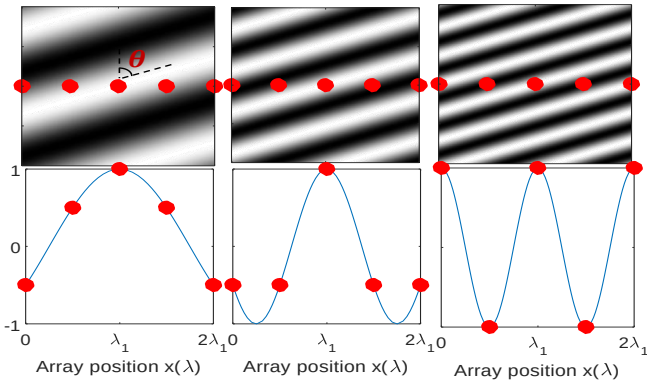

Figure 3.1: Multi-frequency data on array with $N_m = 5$ sensors. Top: time snapshot of propagating plane wave with DOA θ and temporal frequency f_0, $2f_0$, $3f_0$. Bottom: array data are samples of a spatial sinusoid whose spatial frequency depends on the temporal frequency and DOA. Only the real part is shown.

3.3 Methodology

3.3.1 Atomic Norm Minimization (ANM)

To efficiently represent matrices of the form (3.2), we define the atomic set

$$\mathcal{A} := \{\mathbf{A}(w) \circledast \mathbf{x}_w^T : \ w \in [-f_0 d/c, f_0 d/c], \|\mathbf{x}_w\|_2 = 1\}. \tag{3.7}$$

From (3.2), $\mathbf{X}$ is a sparse combination of K atoms from $\mathcal{A}$ since only a few directions have active sources. ANM provides a framework for identifying such sparse combinations in continuously parameterized dictionaries. In our case, the dictionary $\mathcal{A}$ is parameterized by the continuous DOA w.

In the the noise-free case, to identify the K active DOAs w from the data matrix $\mathbf{Y}$, we propose the following ANM-based optimization framework:

$$\min_{\mathbf{X}} \quad \|\mathbf{X}\|_{\mathcal{A}} \quad \text{s.t.} \qquad \mathbf{Y} = \mathbf{X}, \tag{3.8}$$

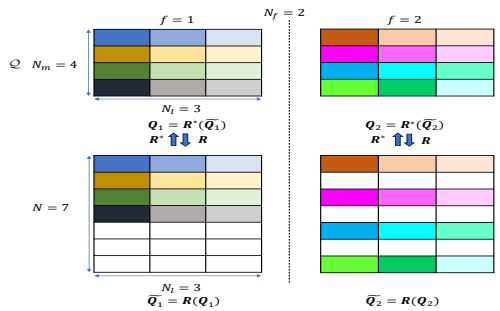

Figure 3.2: Compaction of matrix $\mathbf{X}'$ to $\mathbf{X}$ by mapping $\mathcal{R} : N \times N_f \to N_m \times N_f$ defined in (3.5).

where the atomic norm is defined as

$$\begin{aligned} \|\mathbf{X}\|_{\mathcal{A}} &:= \inf\{t \geq 0 | \mathbf{X} \in t \cdot \mathrm{conv}(\mathcal{A})\} \\ &= \inf\Big\{ \sum_w |c_w| \Big| \mathbf{X} = \sum_w c_w \mathbf{A}(w) \circledast \mathbf{x}_w^T \Big\}. \end{aligned} \tag{3.9}$$

When noise is present, we modify the optimization problem to relax the equality constraint:

$$\min_{\mathbf{X}} \quad \|\mathbf{X}\|_{\mathcal{A}} \quad \text{s.t.} \qquad \|\mathbf{Y} - \mathbf{X}\|_F \leq \eta, \tag{3.10}$$

where η depends on the noise level.

It is not obvious how to obtain DOAs directly based on (3.8) (and (3.10)), as one of the solutions is $\mathbf{Y}$ itself. In the following sections, we develop an equivalent optimization problem for computing the atomic decomposition of $\mathbf{Y}$, which enables determining the DOAs via the dual polynomial.

3.3.2 Dual Atomic Norm and Dual Polynomial

Let $\|\mathbf{X}\|$ be a matrix norm. The associate *dual norm*, denoted $\|\mathbf{Q}\|^*$, is defined as [47, Appendix A.1.6],

$$\|\mathbf{Q}\|^* := \sup_{\|\mathbf{X}\| \leq 1} \langle \mathbf{Q}, \mathbf{X} \rangle_{\mathbb{R}}. \tag{3.11}$$

Also note that the dual of the dual norm is the primal norm.

Now we apply (3.11) to the atomic norm. The primal atomic norm $\|\mathbf{X}\|_{\mathcal{A}}$ is expressed in terms of the dual atomic norm $\|\mathbf{Q}\|_{\mathcal{A}}^*$ (where $\mathbf{Q} := [\mathbf{q}_1 \dots \mathbf{q}_{N_f}] \in \mathbb{C}^{N_m \times N_f}$ is the dual variable) as

$$\|\mathbf{X}\|_{\mathcal{A}} := \sup_{\|\mathbf{Q}\|_{\mathcal{A}}^* \leq 1} \langle \mathbf{Q}, \mathbf{X} \rangle_{\mathbb{R}} = \sup_{\|\mathbf{Q}\|_{\mathcal{A}}^* \leq 1} \langle \mathbf{Q}, \mathbf{Y} \rangle_{\mathbb{R}}, \tag{3.12}$$

where the last equality is only for the noise-free case (see the constraint in (3.8)).

For any dual variable $\mathbf{Q}$, we define the corresponding *dual polynomial vector* $\boldsymbol{\psi}(\mathbf{Q}, w) \in \mathbb{C}^{N_f}$ as

$$\begin{aligned} \boldsymbol{\psi}(\mathbf{Q}, w) &:= [\mathbf{q}_1^H \mathbf{a}(1, w) \dots \mathbf{q}_{N_f}^H \mathbf{a}(N_f, w)]^T \\ &= [\sum_{m=1}^{N_m} q_1^*(m) z^{(m-1)} \dots \sum_{m=1}^{N_m} q_{N_f}^*(m) z^{N_f \cdot (m-1)}]^T. \end{aligned} \tag{3.13}$$

Note that each entry in $\boldsymbol{\psi}(\mathbf{Q}, w)$ is a polynomial in z. The dual polynomial will be useful for setting up the dual certificate condition and extracting the DOA (see Sec. 3.3.4 and Sec. 3.3.5). However, since each frequency has different array manifold vectors, it is difficult to express $\boldsymbol{\psi}(\mathbf{Q}, w)$ as a matrix product of $\mathbf{Q}$ and a vector. To construct a homogeneous representation for $\boldsymbol{\psi}(\mathbf{Q}, w)$, we will leverage $\mathbf{z}$, an ensemble of the array manifold, and the matrix $\mathbf{H} \in \mathbb{C}^{N \times N_f}$ defined in terms of $\mathbf{Q}$ as follows ($m = \{1, \dots, N_m\}, f = \{1, \dots, N_f\}$)

$$\mathbf{H}(i, f) = \begin{cases} \mathbf{Q}(m, f) & \text{for } (i, f) = (f \cdot (m-1) + 1, f) \\ 0 & \text{otherwise,} \end{cases} \tag{3.14}$$

or $\mathbf{H} = \mathcal{R}^*(\mathbf{Q})$, where $\mathcal{R}^* : N_m \times N_f \to N \times N_f$ is the adjoint mapping of $\mathcal{R}$. Note the relationship between $\mathbf{Q}$ and $\mathbf{H}$ can be alternatively expressed as

$$\mathbf{Q} = \mathcal{R}(\mathbf{H}). \tag{3.15}$$

With the help of $\mathbf{H}$ and $\mathbf{z}$, $\boldsymbol{\psi}(\mathbf{Q},w)$ has the homogeneous representation

$$\boldsymbol{\psi}(\mathbf{Q},w) = \mathbf{H}^H \mathbf{z}. \tag{3.16}$$

Now, we consider $\|\mathbf{Q}\|_{\mathcal{A}}^*$, which appears in a constraint in (3.12). Recalling that $\|\mathbf{x}_w\|_2 = 1$, we have

$$\begin{aligned}
\|\mathbf{Q}\|_{\mathcal{A}}^* &:= \sup_{\|\mathbf{X}\|_{\mathcal{A}}\le 1} \langle \mathbf{Q}, \mathbf{X}\rangle_{\mathbb{R}} = \sup_{\|\mathbf{X}\|_{\mathcal{A}}\le 1} \mathrm{Re}[\mathrm{Tr}(\mathbf{Q}^H\mathbf{X})] \\
&= \sup_{\substack{\mathbf{x}_w \\ w}} \mathrm{Re}[\mathrm{Tr}(\mathbf{Q}^H \mathbf{A}(w) \circledast \mathbf{x}_w^T)] \\
&= \sup_{\substack{x_w(f) \\ w}} \mathrm{Re}\left(\sum_{f=1}^{N_f} x_w(f) \mathbf{q}_f^H \mathbf{a}(f,w) \right) \\
&\overset{(a)}{=} \sup_{\substack{\mathbf{x}_w \\ w}} \mathrm{Re}(\mathbf{x}_w^H \boldsymbol{\psi}(\mathbf{Q},w)) = \sup_{\substack{\mathbf{x}_w \\ w}} |\mathbf{x}_w^H \boldsymbol{\psi}(\mathbf{Q},w)| \\
&\overset{(b)}{=} \sup_{w} \|\boldsymbol{\psi}(\mathbf{Q},w)\|_2 = \sup_{w} \|\mathbf{H}^H \mathbf{z}\|_2
\end{aligned} \tag{3.17}$$

where (a) follows by the definition of the dual polynomial vector and (b) follows from the definition of the operator norm.

Using (3.17), the condition $\|\mathbf{Q}\|_{\mathcal{A}}^* \le 1$ can be equivalently formulated as an SDP constraint. To simplify the theoretical analysis, we assume $d = \frac{c}{2f_0}$ and thus $w \in [-1/2, 1/2]$ here. We however notice that the "if" part can be generalized to any $d \le \frac{c}{2f_0}$.

Proposition 3.3.1 *Let $\boldsymbol{\psi}(\mathbf{Q},w)$ be as defined in (3.13) and $w \in [-1/2, 1/2]$. Then $\|\mathbf{Q}\|_{\mathcal{A}}^* \le 1$ holds if and only if there exists a matrix $\mathbf{P}_0 \in \mathbb{C}^{N\times N} \succeq 0$ such that*

$$\sum_{i=1}^{N-k} \mathbf{P}_0(i, i+k) = \delta_k = \begin{cases} 1, & k = 0, \\ 0, & k = 1, \ldots, N-1, \end{cases} \tag{3.18}$$

and such that

$$\begin{bmatrix} \mathbf{P}_0 & \mathbf{H} \\ \mathbf{H}^H & \mathbf{I}_{N_f} \end{bmatrix} \succeq 0. \tag{3.19}$$

Proof See Appendix 3.7.1. □

3.3.3 SDP Formulations of ANM Problems

Noise-free ANM

In the noise-free case, based on Proposition 3.3.1 and (3.12), we have an SDP that is equivalent to (3.8):

$$\begin{aligned} &\max_{\mathbf{Q},\mathbf{P}_0} \langle \mathbf{Q}, \mathbf{Y} \rangle_{\mathbb{R}} \quad \text{s.t.} \begin{bmatrix} \mathbf{P}_0 & \mathbf{H} \\ \mathbf{H}^H & \mathbf{I}_{N_f} \end{bmatrix} \succeq 0, \\ &\sum_{i=1}^{N-k} \mathbf{P}_0(i, i+k) = \delta_k, \mathbf{H} = \mathcal{R}^*(\mathbf{Q}), \end{aligned} \tag{3.20}$$

where the dual variable $\mathbf{Q} \in \mathbb{C}^{N_m \times N_f}$, and $\mathbf{H}$ is related to $\mathbf{Q}$ as in (3.14).

Robust ANM

To make ANM robust to noise and near collisions (see (3.50)), we use the following alternative to (3.20):

$$\begin{aligned} &\max_{\mathbf{Q},\mathbf{P}_0} \langle \mathbf{Q}, \mathbf{Y} \rangle_{\mathbb{R}} - \eta \|\mathbf{Q}\|_F - \lambda \|\mathbf{Q}\|_{1,2} \quad \text{s.t.} \begin{bmatrix} \mathbf{P}_0 & \mathbf{H} \\ \mathbf{H}^H & \mathbf{I}_{N_f} \end{bmatrix} \succeq 0, \\ &\sum_{i=1}^{N-k} \mathbf{P}_0(i, i+k) = \delta_k, \mathbf{H} = \mathcal{R}^*(\mathbf{Q}), \end{aligned} \tag{3.21}$$

where the term $\eta \|\mathbf{Q}\|_F$ suppresses noise [25, (15)] [36, (34), and App. D]. The value of η is the same as in (3.10) [25, 36]. Based on similar arguments to [36, App. D], (3.21) with $\lambda = 0$ is the

dual problem of (3.10). We further add an $\ell_{1,2}$ regularization term to suppress near collisions. The $\ell_{1,2}$ regularization term $\lambda\|\mathbf{Q}\|_{1,2}$ promotes column sparsity, and it reduces the contributions from the "bad frequencies". Near collision is a phenomenon that arises in our multi-frequency ANM model, and it is introduced in Sec. 3.4.4. For the noise-free data, one may set $\eta = 0$, and for the near-collisions-free data, one may set $\lambda = 0$.

3.3.4 Dual Certificate

The dual polynomial $\boldsymbol{\psi}(\mathbf{Q}, w)$ introduced in (3.13) serves as a certificate for the optimality of (3.8) and can therefore be used to extract the unknown DOAs. Specifically, we have the following dual certificate theorem, which is inspired by [21, Proposition II.4]. To ensure uniqueness, a linear independence assumption is added.

Theorem 3.3.2 *Define $\mathcal{W} := \{w_1, \ldots, w_K\}$ as a collection of DOAs with cardinality K. Then $\mathbf{X} = \sum_{w\in\mathcal{W}} c_w \mathbf{A}(w) \circledast \mathbf{x}_w^T$ ($\|\mathbf{x}_w\|_2 = 1$) is the unique atomic decomposition such that $\|\mathbf{X}\|_{\mathcal{A}} = \sum_{w\in\mathcal{W}} |c_w|$ if the following two conditions are satisfied:*
(1) There exists $\mathbf{Q}$ such that the dual polynomial vector $\boldsymbol{\psi}(\mathbf{Q}, w)$ satisfies

$$\begin{cases} \boldsymbol{\psi}(\mathbf{Q}, w) = \operatorname{sign}(c_w^*)\mathbf{x}_w \quad \forall w \in \mathcal{W} \\ \|\boldsymbol{\psi}(\mathbf{Q}, w)\|_2 < 1 \quad \forall w \notin \mathcal{W}, \end{cases} \tag{3.22}$$

where $\operatorname{sign}(c_w^*) := \frac{c_w^*}{|c_w^*|}$.
(2) $\{\mathbf{A}(w) \circledast \mathbf{x}_w^T : w \in \mathcal{W}\}$ is a linearly independent set.

Proof See Appendix 3.7.2. □

3.3.5 DOA Extraction

Based on Theorem 3.2, we know if (3.22) is satisfied, the optimality is guaranteed. In (3.22), $\|\boldsymbol{\psi}(\mathbf{Q}, w)\|_2 = 1$ for $w \in \mathcal{W}$. After solving the SDPs (3.20)–(3.21) by CVX [48], the

optimal dual variables $\mathbf{Q}$ (and thus $\mathbf{H}$) are obtained. Then, the DOA is retrieved by finding the roots for $R(w)$ defined in (3.57).

Based on (3.16), $R(z)$ has the polynomial representation

$$R(z) = 1 - \mathbf{z}^H \mathbf{P}_1 \mathbf{z} = 1 - \sum_{i=-(N-1)}^{(N-1)} r_i z^i, \tag{3.23}$$

where $\mathbf{P}_1 := \mathbf{H}\mathbf{H}^H$ and $r_k := \sum_{i=1}^{N-k} \mathbf{P}_1(i, i+k)$. Indeed, $R(w)$ is a polynomial with degree $2(N-1)$. The roots $\hat{z}$ can be obtained, and $\hat{w}$ is retrieved by locating the roots of $R(z)$ on the unit circle (see Fig. 3.3 (c)):

$$\hat{w} = \left\{ -\frac{\angle \hat{z}}{2\pi} \middle| R(\hat{z}) = 0, |\hat{z}| = 1 \right\}. \tag{3.24}$$

Note $\angle \hat{z} = -2\pi\hat{w} = -\frac{2\pi f_0 d}{c}\cos\theta = \frac{2\pi f_0 d}{c}\cos(\pi - \theta)$. $\hat{\theta}$ is therefore estimated by

$$\hat{\theta} = \pi - \cos^{-1}\left(\frac{\angle \hat{z}}{2\pi f_0 d/c}\right). \tag{3.25}$$

The implementation details for the proposed algorithm are summarized in Algorithm 1.

3.3.6 Fast Algorithm

We notice that many rows in the matrix $\mathbf{H}$ are all zero, yet they contribute to the size of the SDP constraint in (3.19). This inspires us to come up with a fast algorithm which only includes the non-zero rows of $\mathbf{H}$ in the SDP constraint. This fast algorithm generalizes the method to any frequency set.

In particular, consider a frequency set $\mathcal{F} = \{F_1, \ldots, F_{N_f}\} \cdot f_0$ with integers $F_1, \ldots, F_{N_f}$ and define $\mathcal{U} = \{m \cdot f | m \in \{0, \ldots, N_m - 1\}, f \in \{F_1, \ldots, F_{N_f}\}\}$ with cardinality N_u. The ratio of N/N_u in Fig. 3.4(a) shows a factor of 2 in savings for large N_m and N_f which gives up to a factor of 30 savings in CPU time (Fig. 3.4 (b)). Assume the entries in $\mathcal{U}$ are sorted in ascending order.

Algorithm 1: Gridless DOA estimation algorithm

Input: $\mathbf{Y} \in \mathbb{C}^{N_m \times N_f}, d, f_0, c, K$, η (for noisy case), λ (for near collision case)

Initialization:

(For noisy or near collision case) Solve (3.21) by CVX and obtain $\mathbf{H}$

(Otherwise) Solve (3.20) by CVX and obtain $\mathbf{H}$ from $\mathbf{Q}$

$\mathbf{P}_1 \leftarrow \mathbf{H}\mathbf{H}^H$

$N \leftarrow N_f(N_m - 1) + 1$

while $-(N-1) \le k \le (N-1)$ **do**

$r_k \leftarrow \sum_{i=1}^{N-k} \mathbf{P}_1(i, i+k)$

end while

$\mathbf{r} \leftarrow [-r_{-(N-1)} \cdots - r_{(N-1)}]$

$\mathbf{r}(N) \leftarrow \mathbf{r}(N) + 1$

roots $\leftarrow$ roots($\mathbf{r}$)

[**dist**, **ind**] $\leftarrow$ sort(abs($1 -$ abs(**roots**))

roots_sort $\leftarrow$ **roots**(**ind**)

roots_unique $\leftarrow$ **roots_sort**$(1:2:2K)$

$\hat{\theta} \leftarrow 180 -$ acosd(angle(**roots_unique**)$/(f_0 d/c)$)

Output: $\hat{\theta}$

The matrix $\mathbf{H}_r \in \mathbb{C}^{N_u \times N_f}$ with a reduced number of rows can be expressed in terms of $\mathbf{Q}$ as

$$\mathbf{H}_r(r,f) = \begin{cases} \mathbf{Q}(m,f) & \text{for } (\mathcal{U}_r, f) = (f \cdot (m-1) + 1, f) \\ 0 & \text{otherwise;} \end{cases} \tag{3.26}$$

note r is the index of $\mathcal{U}_r = f \cdot (m-1) + 1$. We have the following proposition for an SDP with reduced dimension.

Proposition 3.3.3 *Let $\boldsymbol{\psi}(\mathbf{Q}, w)$ be as defined in (3.13). Then $\|\mathbf{Q}\|_{\mathcal{A}}^* \le 1$ holds if there exists a matrix $\mathbf{P}_{r0} \in \mathbb{C}^{N_u \times N_u} \succeq 0$ such that*

$$\sum_{\substack{i,j \\ \mathcal{U}_j - \mathcal{U}_i = k}} \mathbf{P}_{r0}(i,j) = \delta_k = \begin{cases} 1, & k = 0, \\ 0, & k = 1, \ldots, N-1 \end{cases} \tag{3.27}$$

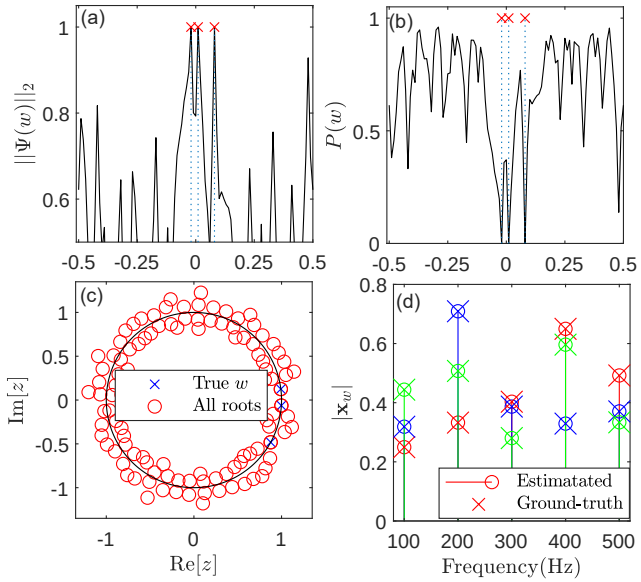

Figure 3.3: DOA extraction through the dual polynomial. An ULA with $N_m = 12$ sensors, and spacing $d = c/2f_0$ is used. $N_f = 5$. $\theta = [80.79°, 88.85°, 92.29°]$, and $w = [0.08, 0.01, -0.02]$. (a) $\|\boldsymbol{\psi}(w)\|_2$ versus w; (b) $P(w)$ versus w; (c) Roots for $P(w)$; (d) Amplitude estimation for each frequency.

and such that

$$\begin{bmatrix} \mathbf{P}_{r0} & \mathbf{H}_r \\ \mathbf{H}_r^H & \mathbf{I}_{N_f} \end{bmatrix} \succeq 0, \tag{3.28}$$

where $\mathbf{H}_r$ *is defined in* (3.26).

The proof is in the Appendix 3.7.3. □

We therefore propose fast alternatives to (3.20) and (3.21) by incorporating the reduced dimension SDP constraint. Note that in Proposition 3.3.1, we theoretically guaranteed the equivalence between (3.20) and (3.8). However, we only guarantee the "if" part in Proposition 3.3.3. Nevertheless, it turns out that the fast algorithm achieves promising performance in the empirical experiments while greatly reducing the computational complexity. The empirical improvement in computational complexity is up to a factor of 30 (see Fig. 3.4 (b)). We apply the fast algorithms throughout Sec. 3.5.

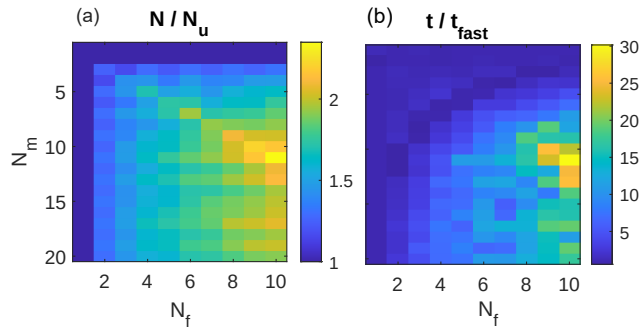

Figure 3.4: (a) N/N_u; (b) t/t_{fast}, where t and t_{fast} are CPU times for (3.20) and the fast program, respectively.

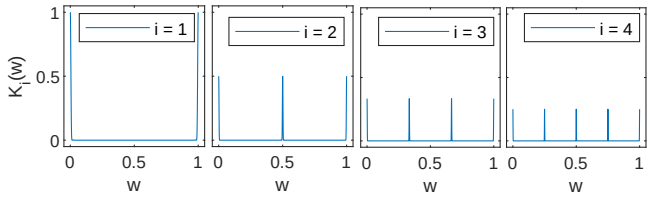

Figure 3.5: Visualization of $K_i(w)$ for $i \in \{1,2,3,4\}$.

3.3.7 Dual SDP Problem

Based on [45, (16)], we consider the dual problem of (3.20). The dual problem of (3.20) is also an SDP, and it can be expressed as

$$\begin{aligned} &\min_{\mathbf{W},\mathbf{u},\widetilde{\mathbf{Y}}} [\text{Tr}(\mathbf{W}) + \text{Tr}(\text{Toep}(\mathbf{u}))] \\ &\text{s.t.} \begin{bmatrix} \text{Toep}(\mathbf{u}) & \widetilde{\mathbf{Y}} \\ \widetilde{\mathbf{Y}}^H & \mathbf{W} \end{bmatrix} \succeq 0, \mathbf{Y} = \mathcal{R}(\widetilde{\mathbf{Y}}), \end{aligned} \tag{3.29}$$

where $\mathbf{W} \in \mathbb{C}^{N_f \times N_f}$, $\mathbf{u} \in \mathbb{C}^N$, $\widetilde{\mathbf{Y}} \in \mathbb{C}^{N \times N_f}$, and $\text{Toep}(\mathbf{u})$ is a $N \times N$ Toeplitz matrix with the first column $\mathbf{u}$.

The derivation of the dual problem is provided in App. 3.7.4. After solving (3.29), the DOAs are retrieved using the Vandermonde decomposition of $\text{Toep}(\mathbf{u})$ [45] and the root-MUSIC procedure. Since both (3.20) and (3.29) are strictly feasible, strong duality holds. Therefore, the optimal values for (3.20) and (3.29) must be the same. Note the matrix associated with the PSD

constraint for both problems are $(N+N_f)\times(N+N_f)$. We can solve either one of them for DOA estimation.

3.4 Dual Polynomial Construction

In Theorem 3.3.2, a *sufficient* condition for optimal atomic decomposition was given. In this section, for certain scenarios, we show that it is possible to construct a dual certificate satisfying (3.22). This implies the success of the DOA estimation algorithm in the noise-free setting.

Following from [20], we consider an alternative, symmetric index set $\{-2M,...,2M\}$ (modified from $\{0,...,N_m-1\}$), where $M=\frac{N_m-1}{4}$. Constructing a dual certificate satisfying the requisite properties (3.22) using the original index set is equivalent to constructing a "modulated" dual polynomial $\boldsymbol{\psi}(w)$ (note that $\boldsymbol{\psi}(w)$ is different from the $\boldsymbol{\psi}(\mathbf{Q},w)$ defined in Sec. III) on the symmetric index set satisfying

$$\begin{cases} \boldsymbol{\psi}(w)=\text{sign}(c_w^*)\overline{\mathbf{x}}_w \quad \forall w\in\mathcal{W} \\ \|\boldsymbol{\psi}(w)\|_2<1 \quad \forall w\notin\mathcal{W}, \end{cases} \tag{3.30}$$

where $\overline{\mathbf{x}}_w(i):=\mathbf{x}_w(i)\cdot e^{-j2\pi wi\frac{N_m-1}{2}}$, $\forall i\in\{1,\dots,N_f\}$. Note $|\overline{\mathbf{x}}_w(i)|=|\mathbf{x}_w(i)\cdot e^{-j2\pi wi\frac{N_m-1}{2}}|=|\mathbf{x}_w(i)|$, and $|\boldsymbol{\psi}(w)(i)\cdot e^{j2\pi wi\frac{N_m-1}{2}}|=|\boldsymbol{\psi}(w)(i)|$. Therefore, as long as $\boldsymbol{\psi}(w)$ (associated with the new index set $\{-2M,\dots,2M\}$) satisfies (3.30), $\overline{\boldsymbol{\psi}(w)}:=\boldsymbol{\psi}(w)\odot[e^{j2\pi w\frac{N_m-1}{2}}\dots e^{j2\pi wN_f\frac{N_m-1}{2}}]^T$ (associated with the original index set) must satisfy (3.22). Indeed, $\|\boldsymbol{\psi}(w)\|_2=\|\overline{\boldsymbol{\psi}(w)}\|_2$ and $\overline{\boldsymbol{\psi}(w)}=\text{sign}(c_w^*)\mathbf{x}_w$ for $\forall w\in\mathcal{W}$. In this section, we will construct $\boldsymbol{\psi}(w)$ that satisfies (3.30).

In addition, $w\in[0,1)$ is assumed in this section. Due to the periodicity of the kernel, it is equivalent to consider $w\in[-1/2,1/2]$ as $w\in[0,1)$. This assumption indicates that $d=\frac{c}{2f_0}$ needs to be assumed for the following analysis.

3.4.1 Interpolation Kernel

Inspired by [20], we leverage the i-th order squared Fejér kernel $K_i(w)$ for the dual polynomial construction:

$$\begin{aligned} K_i(w) &:= \frac{1}{iM} \sum_{k=-2M}^{2M} g_M(k) e^{-j2\pi kw \cdot i} \\ &= \frac{1}{i} \left[\frac{\sin(\pi(M+1)wi)}{(M+1)\sin(\pi wi)} \right]^4, \end{aligned} \tag{3.31}$$

where

$$g_M(k) = \frac{1}{M} \sum_{t=\max\{k-M,-M\}}^{\min\{k+M,M\}} \left(1 - \frac{|t|}{M}\right)\left(1 - \frac{|k-t|}{M}\right). \tag{3.32}$$

$K_i(w), i \in \{1,2,3,4\}$ is shown in Fig. 3.5. When $i = 1$, $K_i(w)$ corresponds to the classical kernel used for the dual polynomial construction in [20, 21, 23, 26, 30]. When i increases, the period of the kernel reduces to $1/i$. Therefore, the periodic copies appears in the visible region $[0,1)$, and will potentially bring about aliasing for the localization. In addition, note that the amplitude of $K_i(w)$ shrinks to $1/i$, which will cancel the scaling factor i of $K_i'(w)$.

We summarize some useful facts for $K_i(w)$

$$K_i(w) = \frac{1}{i} K_1(iw) \quad K_i'(w) = K_1'(iw) \quad K_i''(w) = iK_1''(iw). \tag{3.33}$$

3.4.2 Dual Polynomial Construction by Interpolation Kernel

We construct the dual polynomial vector $\boldsymbol{\psi}(w) \in \mathbb{C}^{N_f}$ as follows

$$\boldsymbol{\psi}(w) := \begin{bmatrix} \sum_{w_k \in \mathcal{W}} [\alpha_{k,1} K_1(w - w_k) + \beta_{k,1} K_1'(w - w_k)] \\ \vdots \\ \sum_{w_k \in \mathcal{W}} [\alpha_{k,N_f} K_{N_f}(w - w_k) + \beta_{k,N_f} K_{N_f}'(w - w_k)] \end{bmatrix}, \tag{3.34}$$

where $K_i'(w - w_k)$ is the first order derivative for $K_i(w - w_k)$.

The constructed dual polynomial in (3.34) is valid if there exists $\alpha_{k,i}$ and $\beta_{k,i}$ $(i = 1, ..., N_f)$

that satisfy (3.22). To satisfy (3.22), for each frequency, we must have [20]

$$\begin{bmatrix} \mathbf{D}_{i,0} & \mathbf{D}_{i,1} \\ \mathbf{D}_{i,1} & \mathbf{D}_{i,2} \end{bmatrix} \begin{bmatrix} \alpha_{1i} \\ \vdots \\ \alpha_{Ki} \\ \beta_{1i} \\ \vdots \\ \beta_{Ki} \end{bmatrix} = \begin{bmatrix} \text{sign}(c_w^*)\overline{\mathbf{x}}_{w_1}(i) \\ \vdots \\ \text{sign}(c_w^*)\overline{\mathbf{x}}_{w_K}(i) \\ 0 \\ \vdots \\ 0 \end{bmatrix} = \begin{bmatrix} \mathbf{c}_i \\ \mathbf{0}_K \end{bmatrix}, \tag{3.35}$$

where ($K_i^{(l)}$ is the l-th order derivative of K_i)

$$[\mathbf{D}_{i,l}]_{mn} := K_i^{(l)}(w_m - w_n), \quad m,n \in \{1,...,K\}, l \in \{0,1,2\}, \tag{3.36}$$

and $\mathbf{c}_i := [\text{sign}(c_w^*)\overline{\mathbf{x}}_{w_1}(i) \dots \text{sign}(c_w^*)\overline{\mathbf{x}}_{w_K}(i)]^T \in \mathbb{C}^K$. $\boldsymbol{\psi}(w)$ can be expressed as

$$\boldsymbol{\psi}(w) = [\sum_{k=1}^{K} \mathbf{c}_1(k) \cdots \sum_{k=1}^{K} \mathbf{c}_{N_f}(k)]^T. \tag{3.37}$$

One sufficient condition to ensure the existence for $\alpha_{k,i}$ and $\beta_{k,i}$ ($i = \{1,...,N_f\}$) is that

$$\mathbf{K}_i := \begin{bmatrix} \mathbf{D}_{i,0} & \mathbf{D}_{i,1} \\ \mathbf{D}_{i,1} & \mathbf{D}_{i,2} \end{bmatrix} \in \mathbb{C}^{2K \times 2K} \tag{3.38}$$

is invertible for any $i \in \{1,...,N_f\}$, which means $\text{rank}(\mathbf{K}_\text{i}) = 2K$. Then, the solution to (3.35) is uniquely determined by inverting $\mathbf{K}_i$. Unfortunately, the invertibility of $\mathbf{K}_i$ may not be guaranteed in general.

3.4.3 Single Source Analysis

We begin with single source analysis ($K = 1$). For one source, there is no separation condition or risk of collision to consider in the analysis. The constructed $K_i(w)$ is guaranteed to satisfy (3.22) as stated in the theorem.

Theorem 3.4.1 *Suppose $K = 1$ (DOA is w_1), and $\overline{\mathbf{x}}_{w_1}(i) \neq 0$ for $\forall i \in \{1,...,N_f\}$. We then have*

$$\begin{cases} \boldsymbol{\psi}(w) = \text{sign}(c_w^*)\overline{\mathbf{x}}_w & w = w_1 \\ \|\boldsymbol{\psi}(w)\|_2 < 1 & \forall w \neq w_1. \end{cases} \tag{3.39}$$

Proof Since $K = 1$, (3.35) reduces to

$$\begin{aligned} \begin{bmatrix} K_i(0) & K_i'(0) \\ K_i'(0) & K_i''(0) \end{bmatrix} \begin{bmatrix} \alpha_{1i} \\ \beta_{1i} \end{bmatrix} &= \begin{bmatrix} 1/i & 0 \\ 0 & K_i''(0) \end{bmatrix} \begin{bmatrix} \alpha_{1i} \\ \beta_{1i} \end{bmatrix} \\ &= \begin{bmatrix} \text{sign}(c_w^*)\overline{\mathbf{x}}_{w_1}(i) \\ 0 \end{bmatrix}. \end{aligned} \tag{3.40}$$

Hence $\alpha_{1i} = i \cdot \text{sign}(c_w^*)\overline{\mathbf{x}}_{w_1}(i)$ and $\beta_{1i} = 0$. Furthermore,

$$\|\boldsymbol{\psi}(w)\|_2^2 = \sum_{i=1}^{N_f} |\alpha_{1i} K_i(w - w_1)|^2. \tag{3.41}$$

When $w = w_1$, $\boldsymbol{\psi}(w) = [\alpha_{11}K_1(0)\ldots\alpha_{1N_f}K_{N_f}(0)]^T = \text{sign}(c_w^*)[\overline{\mathbf{x}}_{w_1}(1)\ldots\overline{\mathbf{x}}_{w_1}(N_f)]^T = \text{sign}(c_w^*)\overline{\mathbf{x}}_w$ and $\|\boldsymbol{\psi}(w)\|_2^2 = \|\overline{\mathbf{x}}_{w_1}\|_2^2 = 1$.

For $w \neq w_1$, suppose $\alpha_{1i} = i \cdot \text{sign}(c_w^*)\overline{\mathbf{x}}_{w_1}(i) \neq 0$ for $\forall i \in \{1,...,N_f\}$, and notice that $K_i(w - w_1) < K_i(0) = 1/i$. Therefore

$$\|\boldsymbol{\psi}(w)\|_2^2 = \sum_{i=1}^{N_f} |\alpha_{1i} K_i(w - w_1)|^2 < \sum_{i=1}^{N_f} |\alpha_{1i} K_i(0)|^2 = 1. \tag{3.42}$$

Therefore, (3.39) must hold. □

3.4.4 Multiple Source Analysis

The analysis is now extended to multiple source cases. For the existing ANM based methods, if there is more than one source, a minimum separation condition is assumed [20, 21, 23, 26]. However, in our signal model, we have to consider the potential for aliasing and collisions (see Sec. 3.4.4).

We first define the separation of $\mathcal{W}$ for the i-th frequency $\Delta(\mathcal{W}^i)$ as the closest wrap-around distance between two *distinct* DOAs w_m, w_n

$$\begin{aligned}\Delta(\mathcal{W}^i) := \inf_{w_m, w_n \in \mathcal{W}} \min\{ & i|w_m - w_n| \mod 1, \\ & 1 - (i|w_m - w_n| \mod 1)\}.\end{aligned} \tag{3.43}$$

Note that although $|w_m - w_n| \in [0,1)$, for $i \geq 2$, $i|w_m - w_n|$ can be greater than 1. Due to the periodicity of the interpolation kernel, we keep only the fractional part of $i|w_m - w_n|$ in the definition of the separation. We first introduce the concepts of aliasing and collision before our analysis.

Aliasing and Collision

Aliasing. Because of the wrap-around nature of $\mathbf{a}(i,w)$, when $d > \frac{\lambda_{N_f}}{2}$ there will be aliasing peaks in the higher frequencies. Aliasing can happen even for the single source case. Specifically, based on [1], if the temporal frequency $f \cdot f_0$ satisfies

$$f \cdot f_0 \geq \frac{c}{d} \frac{1}{1 + |\cos(\theta)|}, \tag{3.44}$$

then aliasing peaks enter into the visible region $[-1/2, 1/2]$ and that frequency experiences *aliasing*. When $d = c/(2f_0)$ and $\theta \in [0^\circ, 180^\circ]$, aliasing happens for all $f \geq 2$. In addition to the peak associated with the ground-truth DOA w, there are aliasing peaks with DOAs $\bar{w} = w \pm \frac{k}{f}, (k < f, k \in \mathbb{N}_+)$. It can be shown that

$$\mathbf{a}(f, w) = \mathbf{a}(f, \bar{w}). \tag{3.45}$$

Aliasing happens for the single frequency beamforming [1] provided that the temporal frequency is high enough. In [17], the authors demonstrate that multiple frequencies can overcome aliasing for conventional beamforming (CBF) and sparse Bayesian learning (SBL) methods.

Collision. One consequence of aliasing is the possibility of *collision* of multiple DOAs. Collision occurs when one DOA lies exactly in the positions of the aliasing peaks of another source. Formally, suppose there are $K = 2$ distinct DOAs w_1 and w_2 ($w_1, w_2 \in [-1/2, 1/2]$). w_1 and w_2 are said to have *collision* in the i-th frequency if

$$\mathbf{a}(i, w_1) = \mathbf{a}(i, w_2). \tag{3.46}$$

Such collision occurs whenever w_1 and w_2 satisfy

$$|w_1 - w_2| = \frac{k}{i} \quad (i \in \{2, \ldots, N_f\}, k < i, k \in \mathbb{N}_+). \tag{3.47}$$

When collision occurs in the i-th frequency bin, it is verified that the pi-th ($p \geq 2, p \in \mathbb{N}_+$) frequency bins also have collision.

For CBF and SBL, collision may bring about ambiguities in the source power (and amplitude) estimation as these two sources share the same array manifold vector.

As an example, let $N_f = 5$, $f_0 = 100$ Hz, $w_1 = 1/2$, and $w_2 = 1/6$. Then $\mathbf{a}(3, w_1) = \mathbf{a}(3, w_2)$ and so these two sources collide in the third frequency bin. As Fig. 3.6 (a)-(b) illustrate,

the spatial samples obtained from all sensors are the same at that frequency. In addition, collision can be interpreted as the intersection of the true DOA of one source and the aliasing peaks of another source. In Fig. 3.6 (c), it is clear the collision exists in the third frequency (300 Hz).

For our ANM problem, if (3.47) is satisfied, based on (3.46), we must have

$$\mathbf{q}_i^H \mathbf{a}(i, w_1) = \mathbf{q}_i^H \mathbf{a}(i, w_2). \tag{3.48}$$

Based on the definition of the dual polynomial in (3.13), the i-th entry of $\boldsymbol{\psi}(\mathbf{Q}, w_1)$ and $\boldsymbol{\psi}(\mathbf{Q}, w_2)$ must therefore be equal. This serves as an additional constraint for the dual polynomial. We refer to (3.47) as the *exact collision* case. Collisions complicate the construction of a dual polynomial that satisfies the optimality condition (see (3.48)). However, we observe that in the numerical experiments, the method still works in the presence of exact collisions (See Fig. 3.8 (a)).

Case Classification

With multiple sources, depending on the true DOAs, we have three possible cases:

- Case 1: There exists an *exact collision*. An exact collision in the i-th frequency is defined as

$$|w_m - w_n| = \frac{k}{i} \quad (i \in \{1, \ldots, N_f\}, k < i). \tag{3.49}$$

  for some DOAs w_m, w_n. For example, suppose $w_1 = 1/2$, $w_2 = 1/6$, $N_f = 6$. Since $|w_1 - w_2| = 1/3$, the third frequency has collision. Indeed, as shown in Fig. 3.6, the spatial samples obtained from all sensors are the same in the third frequency. Notice also that $|w_1 - w_2| = 2/6 = 1/3$, so the sixth frequency also has collision.

- Case 2: There exists a *near collision*. A near collision in the i-th frequency is defined as

$$|w_m - w_n| = \frac{k}{i} \pm \varepsilon \quad (i \in \{1, \ldots, N_f\}, k < i), \tag{3.50}$$

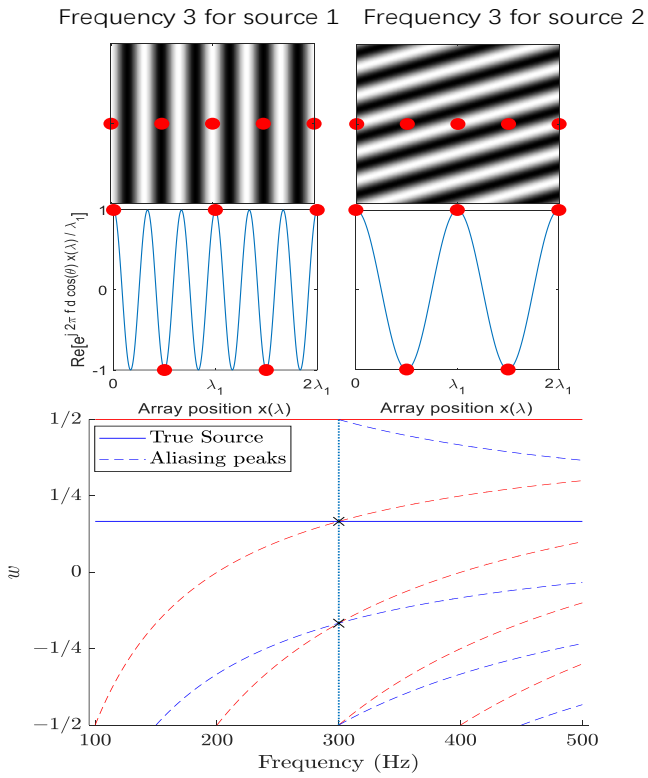

Figure 3.6: Collision demonstration. $K = 2, N_f = 5, w_1 = 1/2, w_2 = 1/6$. (a–b) are the same as Fig. 3.1. (c) Red lines indicate w_1 and blue lines indicate w_2 for the true sources (solid), and the aliased signal (dashed). Collision occurs at 300 Hz.

for some w_m, w_n for sufficiently small $\varepsilon > 0$. The upper bound of ε is proportional to $1/N_m$. For example, suppose $w_1 = 1/4$, $w_2 = 0.001$, $N_f = 6$, and the minimum separation condition $\Delta_{\min} = 0.01$. Then $|w_1 - w_2| = 1/4 - 0.001 = 1/4 - \varepsilon$ with $\varepsilon = 0.001 < \Delta_{\min}$. Therefore, the fourth frequency has a near collision.

- Case 3: There are no collisions or near collisions across all N_f frequencies. For example, suppose $w_1 = 1/4$, $w_2 = 1/10$, $N_f = 6$, and $\Delta_{\min} = 0.01$. It can be easily shown that there is no collision or near collision for any $i \in \{1, \ldots, N_f\}$.

Case 1 and 2 Study

For Case 1 and 2, an analytical guarantee is hard to obtain due to the singularity of $\mathbf{K}_i$. We list some properties for Case 1 in the Appendix 3.7.5. Although an analytical guarantee is hard to obtain, we find the method (3.20) can perform well in Case 1 (See Fig. 3.8 (a)). However, directly solving (3.20) for Case 2 does not give a satisfactory performance (See Fig. 3.7). To resolve the near collision issue in (3.21), we proposed a robust solution in (3.21). The robust solution applies $\ell_{1,2}$ regularization to nullify the contribution from the near collision frequencies. The numerical examples (see Fig. 3.7) demonstrate the effectiveness of the $\ell_{1,2}$ regularization in suppressing near collisions.

Case 3 Analysis

For Case 3, there is no collision and therefore the theoretical analysis becomes tractable. Under a uniform amplitude assumption, we draw analytical conclusions on $\|\boldsymbol{\psi}(w)\|_2$ in Theorem 3.4.2.

Theorem 3.4.2 *If the amplitude is uniform across frequencies for each source (i.e.* $|\mathbf{x}_w(1)| = \cdots = |\mathbf{x}_w(N_f)| = 1/\sqrt{N_f}$ *for all* $w \in \mathcal{W}$*),* $\Delta(\mathcal{W}^i) \geq 4/(N_m - 1)$ *and* $N_m \geq 257$*, then* $\|\boldsymbol{\psi}(w)\|_2 < 1$ *for* $w \notin \mathcal{W}$*.*

Remark The assumptions on the uniform amplitudes and the number of sensors are made to facilitate the proof and may not be necessary in practice. Intuitively, the uniform amplitude assumption prevents certain frequency bins from dominating the source amplitudes, which in the extreme case could transform the multi-frequency model into the single-frequency model. The assumption on the number of sensors is used to bound the Fejér kernel. Note also that the separation assumption implicitly implies an upper bound for the source number K.

Proof See Appendix 3.7.8 and the following paragraphs.

With the first K constraints in (3.35), the constructed $\boldsymbol{\psi}(w)$ automatically satisfies the

first equality condition in (3.22) as $\boldsymbol{\psi}(w)$ satisfies (3.37). However, we also need to show that with the last K equality constraints in (3.35), the constructed $\boldsymbol{\psi}(w)$ satisfies the second inequality condition in (3.22) (i.e. $\|\boldsymbol{\psi}(w)\|_2 < 1$), and we prove Theorem 3.4.2 to guarantee that. Inspired by [20], to bound $\|\boldsymbol{\psi}(w)\|_2$, α and β in (3.35) need to be bounded first. To simplify the derivation, we prove the case when $K = 2$ in the following sections. The result can be generalized to $K > 2$ with the same reasoning.

Supposing that $K = 2$, (3.35) is simplified as a 4×4 system of equations. Note that $i = 1$ is the classical case [20, 21]. Since collision is absent in this case, the matrix $\mathbf{K}_i$ defined in (3.38) is invertible (for detailed reasoning, see Appendix 3.7.7). Therefore, the solution for (3.35) is *uniquely* identified as

$$\begin{aligned}\begin{bmatrix}\alpha_{1i}\\ \alpha_{2i}\\ \beta_{1i}\\ \beta_{2i}\end{bmatrix} &= \begin{bmatrix}\mathbf{D}_{i,0} & \mathbf{D}_{i,1}\\ \mathbf{D}_{i,1} & \mathbf{D}_{i,2}\end{bmatrix}^{-1} \begin{bmatrix}\operatorname{sign}(c_w^*)\overline{\mathbf{x}}_{w_1}(i)\\ \operatorname{sign}(c_w^*)\overline{\mathbf{x}}_{w_2}(i)\\ 0\\ 0\end{bmatrix}\\ &= \begin{bmatrix}\mathbf{S}_i^{-1}\\ -\mathbf{D}_{i,2}^{-1}\mathbf{D}_{i,1}\mathbf{S}_i^{-1}\end{bmatrix} \begin{bmatrix}\operatorname{sign}(c_w^*)\overline{\mathbf{x}}_{w_1}(i)\\ \operatorname{sign}(c_w^*)\overline{\mathbf{x}}_{w_2}(i)\end{bmatrix}.\end{aligned} \tag{3.51}$$

where the Schur complement $\mathbf{S}_i := \mathbf{D}_{i,0} - \mathbf{D}_{i,1}\mathbf{D}_{i,2}^{-1}\mathbf{D}_{i,1}$.

Define $\alpha_i := [\alpha_{1i} \quad \alpha_{2i}]^T$ and $\beta_i := [\beta_{1i} \quad \beta_{2i}]^T$. The following lemma gives upper bounds for $\|\alpha_i\|_\infty$ and $\|\beta_i\|_\infty$.

Lemma 3.4.3 *If $\Delta(\mathcal{W}^i) \geq 4/(N_m - 1) = 1/M$ and $N_m \geq 257$ (or $f_c := 2M \geq 128$), then*

$$\textit{(1)}\|\alpha_i\|_\infty \leq i \cdot 1.008824 \textit{ and } \|\beta_i\|_\infty \leq \frac{3.294 \times 10^{-2}}{f_c}. \tag{3.52}$$

(2) If the amplitude is uniform across frequencies for each source (i.e. $|\mathbf{x}_w(1)| = \cdots = |\mathbf{x}_w(N_f)| =$

$1/\sqrt{N_f}$ *for all* $w \in \{w_1, w_2\}$*), we further have*

$$\|\alpha_i\|_\infty \leq \frac{i \cdot 1.008824}{\sqrt{N_f}}, \|\beta_i\|_\infty \leq \frac{3.294 \times 10^{-2}}{f_c \sqrt{N_f}}. \tag{3.53}$$

Proof See Appendix 3.7.6 for (1). The proof for (2) is similar to that of Lemma 4.3 with the additional condition $\left\| \begin{bmatrix} \text{sign}(c_w^*)\mathbf{x}_{w_1}(i) \\ \text{sign}(c_w^*)\mathbf{x}_{w_2}(i) \end{bmatrix} \right\|_\infty = \frac{1}{\sqrt{N_f}}$. □

Now that the upper bounds for $\|\alpha_i\|_\infty$ and $\|\beta_i\|_\infty$ have been obtained, $\|\boldsymbol{\psi}(w)\|_2$ can be further bounded. The remaining steps for bounding $\|\boldsymbol{\psi}(w)\|_2$ are available in Appendix 3.7.8.

3.5 Numerical Results

3.5.1 Case Studies

We evaluate our method for the 3 cases mentioned in Sec. 3.4.4. The noisy case is also evaluated.

The simulation setup for the following examples is K incoherent sources have DOAs $\theta = \{\theta_1, \ldots \theta_K\}$ (90° is considered broadside). Assume $c = 340$ m/s, $f_0 = 100$ Hz, a uniform linear array with N_m sensors and spacing $d = \frac{c}{2f_0}$. The temporal frequencies of the sources are $\{1, \ldots, N_f\} \cdot f_0$ Hz. The amplitude vectors $\mathbf{x}_w$ of the 3 sources are randomly generated with standard complex normal distribution $\mathcal{CN}(0,1)$ and then normalized so that $\|\mathbf{x}_w\|_2 = 1$. In Fig. 3.8, 100 realizations are evaluated and in each realization, $\mathbf{x}_w$ will be different. We plot the distribution of the DOA estimation of these realizations in the histogram. All $c_w = 1$. The noise for each frequency $\mathbf{w}_f$ is randomly generated from the distribution $\mathcal{CN}(0, \sigma^2)$ and then scaled to fit the desired signal-to-noise ratio (SNR) defined as

$$\text{SNR} = 20 \log_{10} \frac{\|\mathbf{X}\|_F}{\|\mathbf{W}\|_F}. \tag{3.54}$$

This setup is applied in all of the examples in the Sec. 3.5.1 unless otherwise specified.

The Dual Polynomial for Case 2

For Case 2, if $d = \frac{c}{2f_0}$, then all of the frequencies other than the first frequency will have the risk of near collision. To overcome this issue, robust ANM (see (3.21)) needs to be employed to suppress the near collision. An alternative way to suppress the collision is to choose a smaller spacing $d = \frac{c}{2N_f f_0}$ so that the collision can be completely avoided for all frequencies. These two collision suppression methods will be examined. Suppose there are $K = 2$ incoherent sources. In this case, if $N_f \geq 2$, then the $2n$-th (n is any positive integer) frequency will have the near collision. The dual polynomial for different N_f, λ, d, and θ (λ is the regularization hyper-parameter in (3.21)) can be seen in Fig. 3.7. For the regularization parameter λ, we empirically choose it proportional to N_f (i.e. $\lambda = k \cdot N_f$, with $k = 0.125$ in particular for Fig. 3.7). The intuition behind is that for more frequencies, the near collision is more likely to happen. However, since the regularization can bring bias, a smaller λ is more favorable in practice.

From Fig. 3.7 (a), if we only solve (3.20) without regularization, numerous spurious peaks are an obstacle for identifying source positions. However, with regularization, the dual polynomial peaks become precise indicators for the source positions (See Fig. 3.7(b–c)). When $N_f = 6$, the near collision frequencies are the 2nd, 4th, and 6th frequencies. Fig. 3.7 (d) demonstrates the success of choosing a smaller spacing $d = \frac{c}{2N_f f_0}$ in collision suppression without regularization. However, there are potential limitations for smaller spacing. Comparing Fig. 3.7 (e) and (f), the smaller aperture cannot resolve the close sources while the larger aperture can. Thus, although the smaller aperture can avoid the collision, it has lower spatial resolution. We leave the theoretical analysis for choosing the regularization hyperparameter λ as future work.

Case 1, 3, and Noisy cases

The histograms for these cases are plotted in Fig. 3.8. Since $|w_1 - w_2| = |w_2 - w_3| = 0.25$ and $|w_1 - w_3| = 0.5$, there are collisions in both the second and fourth frequencies. From Fig. 3.8 (a), all of the instances in the histogram are nevertheless concentrated in the ground-truth positions, which shows the proposed method can capture the ground-truth positions accurately and has the robustness to the exact collisions. The robustness to the exact collisions is attributed to the combination of multiple frequencies. For the collision frequencies, these two sources are essentially one source since they share the same array manifolds for these frequencies (see (3.46)) and they are mixed coherently, which makes it difficult to separate them. For the non-collision frequencies, the two sources are well-separated. Therefore, if we combine all N_f frequencies, the two peaks associated with the DOAs still stand out as long as there exists non-collision frequencies. To demonstrate Case 3, we compare the single-frequency ($N_f = 1$, see Fig. 3.8 (b)) and multi-frequency ($N_f = 5$, see Fig. 3.8 (c)) scenarios. When $N_f = 1$, there are many bins that lie in the undesired positions. In contrast, when $N_f = 5$, the bins are mostly concentrated in the ground-truth positions. This example demonstrates the potential benefits of multi-frequency ANM. In Fig. 3.8 (d), the setup is identical to that in Fig. 3.8 (c) except the noise is present. For the noisy case, the empirical value of η is chosen as [25]

$$\eta = \sigma/2 \cdot \sqrt{N_m N_f + 2\sqrt{N_m N_f}}.$$

From Fig. 3.8 (d), the proposed method captures the source positions accurately in the noisy cases.

3.5.2 DOA Estimation Performance Evaluation

To comprehensively evaluate the performance of the proposed method, we conduct Monte Carlo experiments. In all of the experiments in this section, each point represents $MC = 100$

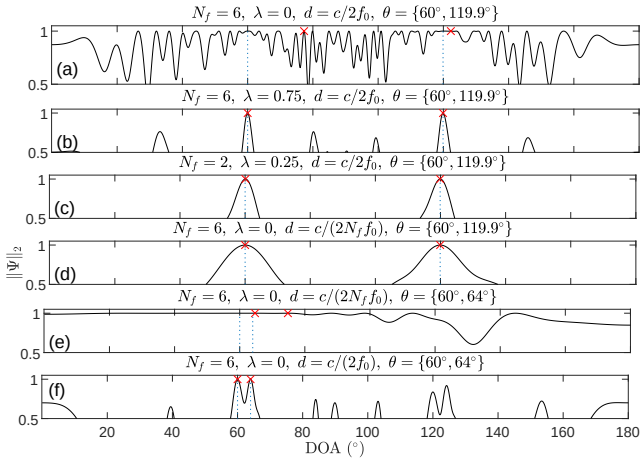

Figure 3.7: $\|\boldsymbol{\psi}(\mathbf{Q}, w)\|_2$ versus DOA θ for Case 2. $N_m = 12$, $f_0 = 100$ Hz, $d = \frac{c}{2f_0}$, and $\mathbf{x}_w \sim \mathcal{CN}(0,1)$, $K = 2$. "$\times$" indicates the peak, and the dashed lines indicate the ground-truth DOAs.

trials, and the root mean square error (RMSE) and mean absolute error (MAE) are computed as

$$\text{RMSE} = \sqrt{\frac{1}{MC}\sum_{m=1}^{MC}\left[\frac{1}{K}\sum_{k=1}^{K}(\hat{\theta}_{mk} - \theta_{mk})^2\right]}. \tag{3.55}$$

$$\text{MAE} = \frac{1}{MC}\sum_{m=1}^{MC}\left(\frac{1}{K}\sum_{k=1}^{K}|\hat{\theta}_{mk} - \theta_{mk}|\right), \tag{3.56}$$

where $\hat{\theta}_{mk}$, and θ_{mk} are (sorted) estimated DOAs, and (sorted) ground-truth DOAs for the k-th source and m-th trial. A maximum threshold of 10° was used to penalize the incorrect DOA estimates (see below). c, f_0, d, and the temporal frequencies are the same as those in Sec. 3.5.1. We also compare the proposed method (ANM) with the multi-frequency sparse Bayesian learning (SBL) [17] and Cramér-Rao bound (CRB) [49, Eq. (119)]. For SBL, the spatial angle is discretized into grids with 0.5° between the adjacent grid points. Although there are many DOA estimation methods, very few of them have been developed for the multiple-frequency model. Therefore, only SBL and CRB are included for reference.

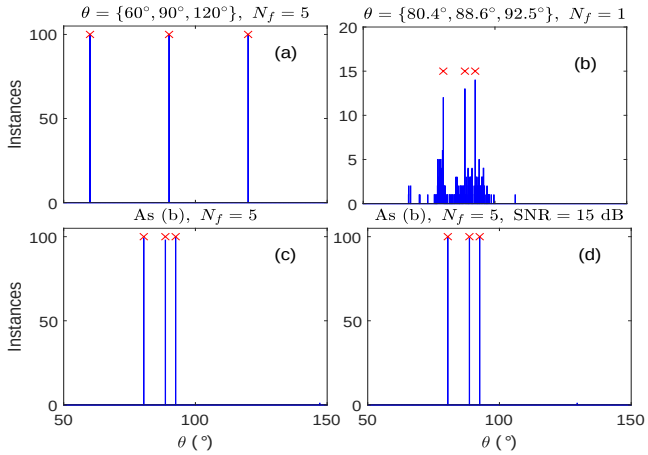

Figure 3.8: Histogram of the estimated DOA $\hat{\theta}$ for 100 realizations with true DOAs ($\times$). $N_m = 12$, $f_0 = 100$ Hz, $d = \frac{c}{2f_0}$, and $\mathbf{x}_w \sim \mathcal{CN}(0,1)$, $K = 3$. For each realization, $\mathbf{x}_w$ will be different. No noise is present except for (d) where SNR is 15 dB.

DOA Estimation under Varying SNR

We first examine the robustness of ANM to noise. The performance of each algorithm under $d = \frac{\lambda_{N_f}}{2}$ is detailed in Fig. 3.9. Notice that in this setup, there will be no aliasing or collision. Therefore, we can turn off the $\ell_{1,2}$ regularization in (3.21). The proposed algorith outperforms SBL in the high SNR cases. At low SNRs, SBL achieves a better performance since it can estimate the noise power. Note for the SBL with limited 0.5° separation, the achievable accuracy for RMSE is 0.125°. In addition, it turns out that SBL has no failure trials (RMSE $> 10^\circ$ is defined as failure) starting from SNR $= 0, -5, -5$, and -10 dB for $N_f = 1, 2, 4$, and 8. For ANM, the same happens for SNR $= 0, 0, -5$, and -5 dB. Therefore, for both SBL and ANM, the performance improves in the low SNR region, which demonstrates the enhanced robustness to noise for the multi-frequency processing.

We then change the spacing to $d = \frac{\lambda_1}{2}$ (See Fig. 3.10). In this case, aliasing and possible collisions will be present when $N_f \geq 2$. However, if more frequencies are available, such ambiguities can be potentially suppressed [17]. For that reason, we only consider the case with 8 frequencies from $100, \ldots, 800$ Hz. In Fig. 3.9 the frequencies were $12.5, \ldots, 100$ Hz, the aperture is here a factor 8 larger in Fig. 3.10. Although the error stops to decrease for ANM in the high

SNR region due to the bias from the regularization, the performance still improves in the low SNR region if more frequencies are available. In addition, compared with Fig. 3.9 (d), the performance of ANM improves when SNR is between 0 to 20 dB, and that demonstrates the benefits of larger apertures.

DOA Estimation under Varying K

We examine the DOA estimation performance under varying numbers of sources (K) in this section. Both the real flat (Fig. 3.11 (a)) and complex random amplitude source (Fig. 3.11 (b)) are tested under noise-free conditions. DOA is an integer randomly generated from a uniform distribution between [0°, 180°]. Therefore, there is no grid mismatch issue for SBL. For the real and flat amplitude case ($\mathbf{x}_w = 1/\sqrt{N_f} \cdot \mathbf{1}_{N_f}$), ANM will be immune to collisions (or near collisions) since the fundamental constraint (3.48) and the dual certificate condition (3.22) can be satisfied simultaneously. Therefore, the optimality is guaranteed and perfect DOA estimation is expected. In the complex random amplitude case, since near collisions affect the performance of ANM, robust ANM (see (3.21)) is applied. From Fig. 3.11 (b), the DOA estimation error increases when the complex amplitude is applied for both methods. ANM (and robust ANM) still outperforms SBL for both real and complex amplitudes even if there is no grid mismatch for SBL. Fig. 3.11 (b) also demonstrates the effectiveness of robust ANM for suppressing near collisions. Because of the presence of near collisions in the complex amplitude case, more frequencies do not necessarily bring about better performance for ANM.

DOA estimation under Varying DOA separation

Finally, we study the DOA estimation performance under different DOA separations. Since the amplitude is real and flat, ANM is immune to near collisions. From Fig. 3.11 (c), SBL has the same estimation error for all DOA separations and N_f. That error is entirely from the grid mismatch. However, the proposed gridless approach overcomes this issue and achieves exact

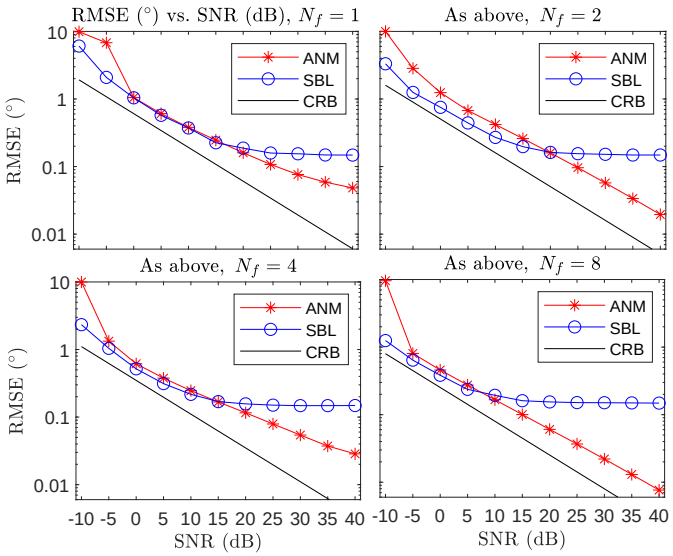

Figure 3.9: RMSE (°) vs. SNR for $d = \frac{\lambda_{N_f}}{2} = \frac{c}{2N_f f_0}$. $N_m = 15$, $K = 3$, $f_0 = 100$ Hz, and the frequency set is $\{1,\ldots,N_f\} \cdot f_0$ Hz. $\lambda = 0$ for all plots. Each point represents 100 trials. The DOAs for each trial are randomly generated between $[10°, 170°]$ with a minimum angular separation $4/N_m$. $\mathbf{x}_w \sim \mathcal{CN}(0,1)$.

DOA estimation.

3.6 Conclusions

The ANM framework is extended to support continuous parameter estimation across multiple frequencies. ANM is initially formulated as an equivalent SDP problem based on the bounded real lemma so that the ANM becomes computationally tractable. In addition, the dual certificate condition is derived. With the help of the dual certificate condition, the optimality can be certified, and the DOAs are identified by finding the roots of a polynomial. We also construct the dual certificate and show that a valid construction exists when the source amplitude has a uniform magnitude. Based on our signal model, the higher frequencies may have the risk of collision or near collision. These two cases are extensively studied and a robust ANM method with regularization is proposed for near collision suppression. The numerical results demonstrate the effectiveness of the proposed method.

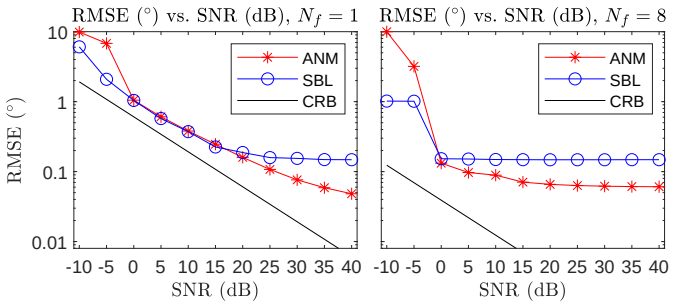

Figure 3.10: RMSE (°) vs. SNR for $d = \frac{\lambda_1}{2} = \frac{c}{2f_0}$. $N_m = 15$, $K = 3$, $f_0 = 100$ Hz, and the frequency set is $\{1, \ldots, N_f\} \cdot f_0$ Hz. $\lambda = 0.6$ for (b). Each point represents 100 trials. The DOAs for each trial are randomly generated between $[10°, 170°]$ with with a minimum angular separation $4/N_m$. $\mathbf{x}_w \sim \mathcal{CN}(0, 1)$.

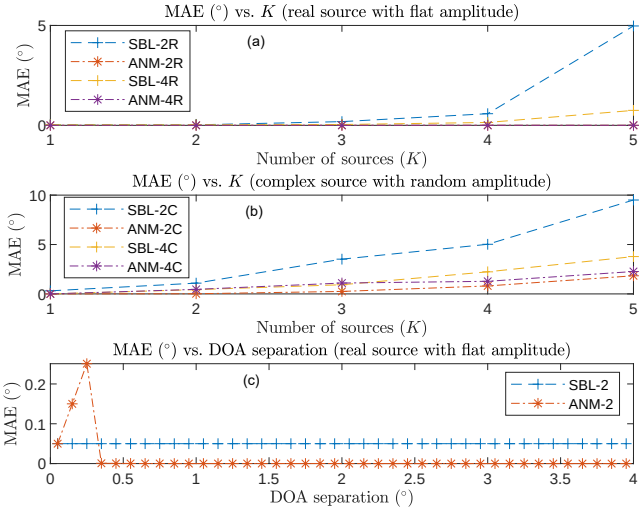

Figure 3.11: MAE (°) vs. K (a–b) and DOA separation (c). $N_m = 15$. No noise is present. For (a–b), $N_f = \{2, 4\}$. For (b), robust ANM is used. For (c), $N_f = 2$, $K = 2$, and $\mathbf{x}_w = 1/\sqrt{N_f} \cdot \mathbf{1}_{N_f}$. The first DOA is $90° -$ DOA separation, and the second DOA is $90° +$ DOA separation. The grid resolution for SBL is $0.1°$.

3.7 Appendix

3.7.1 Proof for Proposition 3.1

Construct the Hermitian trigonometric polynomial

$$R(w) := 1 - \|\mathbf{H}^H \mathbf{z}\|_2^2 = 1 - \mathbf{z}^H \mathbf{H}\mathbf{H}^H \mathbf{z}. \tag{3.57}$$

From (3.17), we know that $\|\mathbf{Q}\|_{\mathcal{A}}^* \leq 1$ holds if and only if $R(w) \geq 0$ for all $w \in [-1/2, 1/2]$.

First, suppose there exists a matrix $\mathbf{P}_0 \in \mathbb{C}^{N\times N} \succeq 0$ such that (3.18) and (3.19) hold. We must argue that $R(w) \geq 0$ for all w. Consider the expression $\mathbf{z}^H \mathbf{P}_0 \mathbf{z}$ and note that

$$\mathbf{z}^H \mathbf{P}_0 \mathbf{z} = \mathrm{Tr}(\mathbf{z}^H \mathbf{P}_0 \mathbf{z}) = \mathrm{Tr}(\mathbf{z}\mathbf{z}^H \mathbf{P}_0) = \sum_{k=-(N-1)}^{N-1} r_k z^{-k},$$

where $r_k = \sum_{i=1}^{N-k} \mathbf{P}_0(i, i+k)$ for $k \geq 0$ and $r_k = r_{-k}^*$ for $k < 0$. From (3.18), we conclude that $\mathbf{z}^H \mathbf{P}_0 \mathbf{z} = z^0 = 1$. Substituting this into $R(w)$ and defining $\mathbf{P}_1 := \mathbf{H}\mathbf{H}^H$ gives

$$R(w) = \mathbf{z}^H \mathbf{P}_0 \mathbf{z} - \mathbf{z}^H \mathbf{P}_1 \mathbf{z} = \mathbf{z}^H (\mathbf{P}_0 - \mathbf{P}_1)\mathbf{z}.$$

Since the matrix in (3.19) is PSD, its Schur complement $\mathbf{P}_0 - \mathbf{H}\mathbf{I}_{N_f}^{-1}\mathbf{H}^H = \mathbf{P}_0 - \mathbf{P}_1 \succeq 0$, and so $R(w) \geq 0$ for all $w \in [-1/2, 1/2]$.

Next, suppose $R(w) \geq 0$ for all $w \in [-1/2, 1/2]$. We must argue that there exists a matrix $\mathbf{P}_0 \in \mathbb{C}^{N\times N} \succeq 0$ such that (3.18) and (3.19) hold. Since $R(w) \geq 0$, $1 \geq \mathbf{z}^H \mathbf{P}_1 \mathbf{z}$, where we have again defined $\mathbf{P}_1 := \mathbf{H}\mathbf{H}^H \succeq 0$. From [44, Lemma 4.25] and the fact that 1 and $\mathbf{z}^H \mathbf{P}_1 \mathbf{z}$ are univariate trigonometric polynomials, it follows that there exists $\mathbf{P}_0 \succeq \mathbf{P}_1$ such that $1 = \mathbf{z}^H \mathbf{P}_0 \mathbf{z}$ and (3.18) hold. The matrix in (3.19) has Schur complement $\mathbf{P}_0 - \mathbf{H}\mathbf{I}_{N_f}^{-1}\mathbf{H}^H = \mathbf{P}_0 - \mathbf{P}_1 \succeq 0$, and therefore (3.19) holds. □

3.7.2 Proof for Theorem 3.2

First, notice that if (3.22) is satisfied, based on (3.17), we have $\|\mathbf{Q}\|_{\mathcal{A}}^* \leq 1$. Then,

$$\begin{aligned}
\|\mathbf{X}\|_{\mathcal{A}} &\geq \|\mathbf{X}\|_{\mathcal{A}} \cdot \|\mathbf{Q}\|_{\mathcal{A}}^* \overset{(a)}{\geq} \langle \mathbf{Q}, \mathbf{X} \rangle_{\mathbb{R}} = \mathrm{Re}[\mathrm{Tr}(\mathbf{Q}^H \mathbf{X})] \\
&= \sum_{w \in \mathcal{W}} \mathrm{Re}[\mathrm{Tr}(c_w \mathbf{Q}^H \mathbf{A}(w) \circledast \mathbf{x}_w^T)] \\
&= \sum_{w \in \mathcal{W}} \sum_{f=1}^{N_f} \mathrm{Re}[c_w \mathbf{q}_f^H x_w(f) \mathbf{a}(f,w)] = \sum_{w \in \mathcal{W}} \mathrm{Re}[c_w \mathbf{x}_w^H \boldsymbol{\psi}(\mathbf{Q}, w)] \\
&\overset{(b)}{=} \sum_{w \in \mathcal{W}} \mathrm{Re}[c_w \mathrm{sign}(c_w^*) \|\mathbf{x}_w\|_2^2] = \sum_{w \in \mathcal{W}} |c_w| \overset{(c)}{\geq} \|\mathbf{X}\|_{\mathcal{A}},
\end{aligned} \tag{3.58}$$

where (a) is based on Hölder's inequality, (b) follows because if $w \in \mathcal{W}$, then $\boldsymbol{\psi}(\mathbf{Q}, w) = \mathrm{sign}(c_w^*)\mathbf{x}_w$ based on (3.22), and (c) follows from the definition of the atomic norm (3.9) as the infimum of the combination coefficients. Hence, $\|\mathbf{X}\|_{\mathcal{A}} = \langle \mathbf{Q}, \mathbf{X} \rangle_{\mathbb{R}} = \sum_{w \in \mathcal{W}} |c_w|$.

For uniqueness, suppose there exists another decomposition $\mathbf{X} = \sum_{w'} c_{w'} \mathbf{A}(w') \circledast \mathbf{x}_{w'}^T$ which satisfies $\|\mathbf{X}\|_{\mathcal{A}} = \sum_{w'} |c_{w'}|$. There must exist $w' \notin \mathcal{W}$ contributing to $\mathbf{X}$ due to the mutual linear independence of the atoms. Therefore, we have the contradiction:

$$\begin{aligned}
\sum_{w'} |c_{w'}| &= \|\mathbf{X}\|_{\mathcal{A}} = \langle \mathbf{Q}, \mathbf{X} \rangle_{\mathbb{R}} = \sum_{w'} \mathrm{Re}[c_{w'} \langle \mathbf{x}_{w'}, \boldsymbol{\psi}(\mathbf{Q}, w') \rangle] \\
&= \sum_{w' \in \mathcal{W}} \mathrm{Re}[c_{w'} \mathbf{x}_{w'}^H \boldsymbol{\psi}(\mathbf{Q}, w')] + \sum_{w' \notin \mathcal{W}} \mathrm{Re}[c_{w'} \mathbf{x}_{w'}^H \boldsymbol{\psi}(\mathbf{Q}, w')] \\
&\overset{(a)}{<} \sum_{w' \in \mathcal{W}} |c_{w'}| + \sum_{w' \notin \mathcal{W}} |c_{w'}| = \sum_{w'} |c_{w'}|,
\end{aligned} \tag{3.59}$$

where (a) is because of (3.22). Therefore, the atomic decomposition which satisfies $\|\mathbf{X}\|_{\mathcal{A}} = \sum_{w \in \mathcal{W}} |c_w|$ must be unique. □

3.7.3 Proof for Proposition 3.3.3

Construct the Hermitian trigonometric polynomial

$$R(w) := 1 - \|\mathbf{H}_r^H \mathbf{z}_r\|_2^2 = 1 - \mathbf{z}_r^H \mathbf{H}_r \mathbf{H}_r^H \mathbf{z}_r. \tag{3.60}$$

From (3.17), we know that $\|\mathbf{Q}\|_{\mathcal{A}}^* \leq 1$ holds if and only if $R(w) \geq 0$ for all w.

First, suppose there exists a matrix $\mathbf{P}_{r0} \in \mathbb{C}^{N_u \times N_u} \succeq 0$ such that (3.27) and (3.28) hold. We must argue that $R(w) \geq 0$ for all w. Consider the expression $\mathbf{z}_r^H \mathbf{P}_{r0} \mathbf{z}_r$ and note that

$$\mathbf{z}_r^H \mathbf{P}_{r0} \mathbf{z}_r = \mathrm{Tr}(\mathbf{z}_r^H \mathbf{P}_{r0} \mathbf{z}_r) = \mathrm{Tr}(\mathbf{z}_r \mathbf{z}_r^H \mathbf{P}_{r0}) = \sum_{k=-(N-1)}^{N-1} r_k z^{-k}$$

$$r_k = \sum_{i,j,\mathcal{U}_j - \mathcal{U}_i = k} \mathbf{P}_{r0}(i,j) \tag{3.61}$$

for $k \geq 0$ and $r_k = r_{-k}^*$ for $k < 0$. From (3.27), we then conclude that $\mathbf{z}_r^H \mathbf{P}_{r0} \mathbf{z}_r = z^0 = 1$. Substituting this fact into $R(w)$ and defining $\mathbf{P}_{r1} := \mathbf{H}_r \mathbf{H}_r^H$, we have

$$R(w) = \mathbf{z}_r^H \mathbf{P}_{r0} \mathbf{z}_r - \mathbf{z}_r^H \mathbf{P}_{r1} \mathbf{z}_r = \mathbf{z}_r^H (\mathbf{P}_{r0} - \mathbf{P}_{r1}) \mathbf{z}_r. \tag{3.62}$$

Since the matrix in (3.28) is PSD, its Schur complement $\mathbf{P}_{r0} - \mathbf{H}_r \mathbf{I}_{N_f}^{-1} \mathbf{H}_r^H = \mathbf{P}_{r0} - \mathbf{P}_{r1} \succeq 0$, and so $R(w) \geq 0$ for all w. □

3.7.4 The Derivation of the Dual Problem of (20)

Consider the Lagrangian of (3.20) given by

$$\begin{aligned}
&\mathcal{L}(\mathbf{Q},\mathbf{P}_0,\mathbf{H},\mathbf{\Lambda}_1,\mathbf{\Lambda}_2,\mathbf{\Lambda}_3,\mathbf{\Lambda}_Q,\mathbf{v}) = \\
&\langle \mathbf{Q},\mathbf{Y}\rangle_{\mathbb{R}} - \left\langle \begin{bmatrix} \mathbf{\Lambda}_1 & \mathbf{\Lambda}_2 \\ \mathbf{\Lambda}_2^H & \mathbf{\Lambda}_3 \end{bmatrix}, \begin{bmatrix} \mathbf{P}_0 & \mathbf{H} \\ \mathbf{H}^H & \mathbf{I}_{N_f} \end{bmatrix} \right\rangle_{\mathbb{R}} \\
&- \sum_{k=0}^{N-1} v_k(\delta_k - \sum_{j-i=k} \mathbf{P}_0(i,j)) - \langle \mathbf{\Lambda}_Q, \mathbf{H} - \mathcal{R}^*(\mathbf{Q})\rangle_{\mathbb{R}} \\
&= \langle \mathbf{Q},\mathbf{Y}\rangle_{\mathbb{R}} + \langle \mathbf{\Lambda}_Q, \mathcal{R}^*(\mathbf{Q})\rangle_{\mathbb{R}} - [\langle \mathbf{P}_0, \mathbf{\Lambda}_1\rangle_{\mathbb{R}} + 2\langle \mathbf{\Lambda}_2, \mathbf{H}\rangle_{\mathbb{R}} + \mathrm{Tr}(\mathbf{\Lambda}_3)] \\
&- \mathbf{v}_0 + \langle \mathbf{P}_0, \mathrm{Toep}(\mathbf{v})\rangle_{\mathbb{R}} - \langle \mathbf{\Lambda}_Q, \mathbf{H}\rangle_{\mathbb{R}}. \qquad (3.63)
\end{aligned}$$

The derivation uses: $\sum_{k=0}^{N-1} v_k \sum_{j-i=k} \mathbf{P}_0(i,j) = \langle \mathbf{P}_0, \mathrm{Toep}(\mathbf{v})\rangle_{\mathbb{R}}$. Further, the dual matrix $\begin{bmatrix} \mathbf{\Lambda}_1 & \mathbf{\Lambda}_2 \\ \mathbf{\Lambda}_2^H & \mathbf{\Lambda}_3 \end{bmatrix}$ associated with the inequality constraint $\begin{bmatrix} \mathbf{P}_0 & \mathbf{H} \\ \mathbf{H}^H & \mathbf{I}_{N_f} \end{bmatrix} \succeq 0$ is an PSD matrix to ensure the inner product between these two matrices is non-negative, whereby the optimal value for the dual problem gives a lower bound for the primal problem.

The dual function is

$$\begin{aligned}
g(\mathbf{\Lambda}_1,\mathbf{\Lambda}_2,\mathbf{\Lambda}_3,\mathbf{\Lambda}_Q,\mathbf{v}) = &\inf_{\mathbf{Q},\mathbf{P}_0,\mathbf{H}} \mathcal{L}(\mathbf{Q},\mathbf{P}_0,\mathbf{H},\mathbf{\Lambda}_1,\mathbf{\Lambda}_2,\mathbf{\Lambda}_3,\mathbf{\Lambda}_Q,\mathbf{v}) \\
&\text{s.t.} \begin{bmatrix} \mathbf{\Lambda}_1 & \mathbf{\Lambda}_2 \\ \mathbf{\Lambda}_2^H & \mathbf{\Lambda}_3 \end{bmatrix} \succeq 0. \qquad (3.64)
\end{aligned}$$

The infimum of $\mathcal{L}$ over $\mathbf{Q}$ is thereby $\inf_{\mathbf{Q}} J(\mathbf{Q}) := [\langle \mathbf{Q},\mathbf{Y}\rangle_{\mathbb{R}} + \langle \mathbf{\Lambda}_Q, \mathcal{R}^*(\mathbf{Q})\rangle_{\mathbb{R}}] = [\langle \mathbf{Y},\mathbf{Q}\rangle_{\mathbb{R}} + \langle \mathcal{R}(\mathbf{\Lambda}_Q),\mathbf{Q}\rangle_{\mathbb{R}}] = \langle \mathbf{Y} + \mathcal{R}(\mathbf{\Lambda}_Q),\mathbf{Q}\rangle_{\mathbb{R}}$. The infimum of $J(\mathbf{Q})$ is bounded only if $\mathbf{Y} = -\mathcal{R}(\mathbf{\Lambda}_Q)$. Similarly, the infimum of $\mathcal{L}$ over $\mathbf{P}_0$ is bounded only if $\mathrm{Toep}(\mathbf{v}) = \mathbf{\Lambda}_1 \succeq 0$. The infimum of $\mathcal{L}$

over $\mathbf{H}$ is bounded only if $\mathbf{\Lambda}_Q = -2\mathbf{\Lambda}_2$. Consider $2\mathbf{\Lambda}_2 = \widetilde{\mathbf{Y}}$, then we must have $\mathbf{Y} = -\mathcal{R}(\mathbf{\Lambda}_Q) = \mathcal{R}(2\mathbf{\Lambda}_2) = \mathcal{R}(\widetilde{\mathbf{Y}})$.

Consider $\mathbf{\Lambda}_3 = \frac{1}{2}\mathbf{W}$, and $\mathbf{v} = \frac{1}{2}\mathbf{u}$, the dual function becomes $-\frac{1}{2}\mathrm{Tr}(\mathbf{W}) - \frac{1}{2}\mathrm{Tr}(\mathrm{Toep}(\mathbf{u}))$. The dual problem is

$$\begin{aligned} &\max_{\mathbf{W},\mathbf{u},\widetilde{\mathbf{Y}}} -\frac{1}{2}[\mathrm{Tr}(\mathbf{W})+\mathrm{Tr}(\mathrm{Toep}(\mathbf{u}))] \\ &\quad \text{s.t.} \begin{bmatrix} \mathrm{Toep}(\mathbf{u}) & \widetilde{\mathbf{Y}} \\ \widetilde{\mathbf{Y}}^H & \mathbf{W} \end{bmatrix} \succeq 0, \mathbf{Y}=\mathcal{R}(\widetilde{\mathbf{Y}}), \end{aligned} \tag{3.65}$$

which is equivalent to (3.29). □

3.7.5 Properties for Exact Collision

$\mathbf{K}_i$ is Singular

First observe that $\mathbf{K}_i$ in (3.38) is singular. We also recognize the periodicity of $K_i(w)$. Since $K_i(w) = K_i(w+k/i)(k < i, i \in \{1,\ldots,N_f\})$, k/i is the period for $K_i(w)$. In addition, k/i is also the period for $K_i'(w)$ and $K_i''(w)$. Without loss of generality, we assume there exists collision between w_1 and w_2 (i.e. $|w_1 - w_2| = \frac{k}{i}$), then

$$\begin{aligned} &K_i(0) = K_i(w_1 - w_2) = K_i(w_2 - w_1) = 1, \\ &K_i'(0) = K_i'(w_1 - w_2) = K_i'(w_2 - w_1) = 0, \text{ and} \\ &K_i''(0) = K_i''(w_1 - w_2) = K_i''(w_2 - w_1). \end{aligned} \tag{3.66}$$

The first and second row of $\mathbf{K}_i$ are

$$\begin{aligned} &[K_i(w_1-w_1)\ldots K_i(w_1-w_K)\ldots K_i'(w_1-w_1)\ldots K_i'(w_1-w_K)] \\ &[K_i(w_2-w_1)\ldots K_i(w_2-w_K)\ldots K_i'(w_2-w_1)\ldots K_i'(w_2-w_K)]. \end{aligned} \tag{3.67}$$

Note that $K_i(w_2 - w_j) = K_i(w_1 - w_j - (w_1 - w_2)) = K_i(w_1 - w_j)$ and $K_i'(w_2 - w_j) = K_i'(w_1 - w_j - (w_1 - w_2)) = K_i'(w_1 - w_j)$ for any j. Thus, the first two rows are identical. $\mathbf{K}_i$ is hence rank-deficient and singular.

However, the singularity of $\mathbf{K}_i$ does not imply that the solution to the system of equations (3.35) does not exist. If $\left[\text{sign}(c_w^*)x_{w_1}(i) \ldots \text{sign}(c_w^*)x_{w_K}(i)\ 0 \ldots 0\right]^T := \widehat{\mathbf{x}}_i$ lies in the range space of $\mathbf{K}_i$, the solution of (3.35) exists but non-unique. Among the infinite number of solutions, we choose the Moore-Penrose pseudoinverse solution $\mathbf{K}_i^{\dagger}\widehat{\mathbf{x}}_i$.

Recovery for the Coefficients not Possible

Here, we discuss the possibility of recovering the coefficients under the collision condition. Although it is possible to localize the sources, the recovery of the coefficients $\widehat{c}_k\widehat{\mathbf{x}}_k$ is not possible due to the fundamental limit in (3.46).

The DOAs are localized by finding the peak of the dual polynomial vector under the collision condition. For the estimated DOAs $(\widehat{w}_1, ..., \widehat{w}_K)$, (3.2) gives

$$\mathbf{X} = \sum_{k=1}^{K} \widehat{c}_k \mathbf{A}(\widehat{w}_k) \circledast \widehat{\mathbf{x}}_k^T = \sum_{k=1}^{K} \mathbf{A}(\widehat{w}_k) \circledast \widetilde{\mathbf{x}}_k^T, \tag{3.68}$$

where $\widetilde{\mathbf{x}}_k := \widehat{c}_k\widehat{\mathbf{x}}_k$. Since $\mathbf{Y} = \mathbf{X} = [\mathbf{y}_1 ... \mathbf{y}_{N_f}]$, the entries in $\widetilde{\mathbf{x}}_k$ are recovered by solving $\mathbf{y}_f = \sum_{k=1}^{K} \mathbf{a}(f, \widehat{w}_k)\widetilde{\mathbf{x}}_k = [\mathbf{a}(f, \widehat{w}_1) ... \mathbf{a}(f, \widehat{w}_K)][\widetilde{\mathbf{x}}_1(f) ... \widetilde{\mathbf{x}}_K(f)]^T (f = 1, \ldots, N_f)$.

However, when $f = i$, $\mathbf{a}(i, \widehat{w}_1) = \mathbf{a}(i, \widehat{w}_2)$ from (3.46). Then, $\mathbf{a}(i, \widehat{w}_1)\widetilde{\mathbf{x}}_1(i) + \mathbf{a}(i, \widehat{w}_2)\widetilde{\mathbf{x}}_2(i) = \mathbf{a}(i, \widehat{w}_1)[\widetilde{\mathbf{x}}_1(i) + \widetilde{\mathbf{x}}_2(i)]$. Therefore, we have to decouple $\widetilde{\mathbf{x}}_1(i)$ and $\widetilde{\mathbf{x}}_2(i)$ based on their sum, which is impossible.

3.7.6 Proof for Lemma 3.4.3

From below (3.30), $|\overline{\mathbf{x}}_w(i)| = |\mathbf{x}_{w_2}(i)|$, we have

$$\begin{aligned}
\|\alpha_i\|_\infty &= \left\| \mathbf{S}_i^{-1} \begin{bmatrix} \operatorname{sign}(c_w^*)\overline{\mathbf{x}}_{w_1}(i) \\ \operatorname{sign}(c_w^*)\overline{\mathbf{x}}_{w_2}(i) \end{bmatrix} \right\|_\infty \\
&\le \|\mathbf{S}_i^{-1}\|_\infty \left\| \begin{bmatrix} \operatorname{sign}(c_w^*)\mathbf{x}_{w_1}(i) \\ \operatorname{sign}(c_w^*)\mathbf{x}_{w_2}(i) \end{bmatrix} \right\|_\infty \le \|\mathbf{S}_i^{-1}\|_\infty, \qquad (3.69) \\
\|\beta_i\|_\infty &\le \left\| \mathbf{D}_{i,2}^{-1}\mathbf{D}_{i,1}\mathbf{S}_i^{-1} \begin{bmatrix} \operatorname{sign}(c_w^*)\mathbf{x}_{w_1}(i) \\ \operatorname{sign}(c_w^*)\mathbf{x}_{w_2}(i) \end{bmatrix} \right\|_\infty \\
&\le \|\mathbf{D}_{i,2}^{-1}\mathbf{D}_{i,1}\mathbf{S}_i^{-1}\|_\infty \le \|\mathbf{D}_{i,2}^{-1}\|_\infty \|\mathbf{D}_{i,1}\|_\infty \|\mathbf{S}_i^{-1}\|_\infty. \qquad (3.70)
\end{aligned}$$

$\|\mathbf{S}_i^{-1}\|_\infty$ is bounded as

$$\begin{aligned}
\|\mathbf{S}_i^{-1}\|_\infty &= \|(\mathbf{D}_{i,0} - \mathbf{D}_{i,1}\mathbf{D}_{i,2}^{-1}\mathbf{D}_{i,1})^{-1}\|_\infty \\
&\le 1/(1 - \|\mathbf{I} - (\mathbf{D}_{i,0} - \mathbf{D}_{i,1}\mathbf{D}_{i,2}^{-1}\mathbf{D}_{i,1})\|_\infty) \\
&\le 1/[1 - (\|\mathbf{I} - \mathbf{D}_{i,0}\|_\infty + \|\mathbf{D}_{i,1}\|_\infty^2 \|\mathbf{D}_{i,2}^{-1}\|_\infty)]. \qquad (3.71)
\end{aligned}$$

Inspired by the proof of [20, Lemma 2.2], the bounds for $\|\mathbf{I} - \mathbf{D}_{i,0}\|_\infty$, $\|\mathbf{D}_{i,1}\|_\infty$, and $\|K_i''(0)\mathbf{I} - \mathbf{D}_{i,2}\|_\infty$ are established (define $d_0 := 6.253 \times 10^{-3}, d_1 := 7.639 \times 10^{-2}, d_2 := 1.053, d_3 :=$

$11/32\pi^2$, where d_0, d_1, and d_2 are empirical [20] and d_3 is analytical):

$$\begin{aligned}
&\|\mathbf{I}-\mathbf{D}_{i,0}\|_\infty \le \left\|\mathbf{I}-\frac{1}{i}\mathbf{I}\right\|_\infty + \left\|\frac{1}{i}\mathbf{I}-\mathbf{D}_{i,0}\right\|_\infty = 1-\frac{1}{i} + |K_i(w_1-w_2)| \\
&= 1-\frac{1}{i}+\frac{1}{i}|K_1(i(w_1-w_2))| \le 1+\frac{d_0-1}{i}, \\
&\|\mathbf{D}_{i,1}\|_\infty = |K_i'(w_1-w_2)| = |K_1'(i(w_1-w_2))| \le d_1 f_c, \\
&\|K_i''(0)\mathbf{I}-\mathbf{D}_{i,2}\|_\infty = |K_i''(w_1-w_2)| = i|K_1''(i(w_1-w_2))| \le i d_2 f_c^2, \\
&|K_i''(0)| = \frac{i\pi^2 f_c(f_c+4)}{3} \ge \frac{i\pi^2 f_c^2}{3} + \frac{4i\pi^2 f_c^2}{3\cdot 128} = i\cdot d_3 f_c^2.
\end{aligned} \tag{3.72}$$

Therefore, $\|\mathbf{D}_{i,2}^{-1}\|_\infty$ is bounded as follows ($d_4 := 1/(d_3-d_2) = 0.4275$)

$$\|\mathbf{D}_{i,2}^{-1}\|_\infty \le \frac{1}{|K_i''(0)| - \|K_i''(0)\mathbf{I}-\mathbf{D}_{i,2}\|_\infty} \le \frac{1}{i(d_3-d_2)f_c^2} = \frac{d_4}{i f_c^2}. \tag{3.73}$$

Then, following (3.69) and (3.70), the bounds for $\|\alpha_i\|_\infty$ and $\|\beta_i\|_\infty$ are (define $c_\alpha := 1.008824$, and $c_\beta := 3.294\times 10^{-2}$):

$$\begin{aligned}
&\|\alpha_i\|_\infty \le \|\mathbf{S}_i^{-1}\|_\infty \le \frac{i}{1-d_0-d_1^2 d_4} := i\cdot c_\alpha, \\
&\|\beta_i\|_\infty \le \|\mathbf{D}_{i,2}^{-1}\|_\infty \|\mathbf{D}_{i,1}\|_\infty \|\mathbf{S}_i^{-1}\|_\infty \le \frac{d_1 d_4}{f_c(1-d_0-d_1^2 d_4)} := \frac{c_\beta}{f_c}.
\end{aligned} \tag{3.74}$$

□

3.7.7 Invertibility of $\mathbf{K}_i$

Using the Schur complement, $\mathbf{K}_i$ is invertible if $\mathbf{D}_{i,2}$ and the Schur complement $\mathbf{S}_i := \mathbf{D}_{i,0} - \mathbf{D}_{i,1}\mathbf{D}_{i,2}^{-1}\mathbf{D}_{i,1}$ are both invertible. To show that, we use the fact that a Hermitian matrix $\mathbf{M}$ is invertible if $\|\mathbf{I}-\mathbf{M}\|_\infty < 1$ [20, eq. (2.12)].

We begin with $\mathbf{D}_{i,2}$. Notice $|K_i''(0)| = i|K_1''(0)| = \frac{i\pi^2 f_c(f_c+4)}{3}$. Therefore, based on (3.72),

$$\left\|\mathbf{I} - \frac{\mathbf{D}_{i,2}}{K_i''(0)}\right\|_\infty = \frac{\|K_i''(0)\mathbf{I} - \mathbf{D}_{i,2}\|_\infty}{|K_i''(0)|} \leq \frac{id_2 f_c^2}{i\pi^2 f_c(f_c+4)/3} < 1, \tag{3.75}$$

which implies that $\frac{\mathbf{D}_{i,2}}{K_i''(0)}$ is invertible. Hence, $\mathbf{D}_{i,2}$ is also invertible. We then consider the invertibility of $\mathbf{S}_i$. Based on the triangle inequality,

$$\|\mathbf{I} - \mathbf{S}_i\|_\infty \leq \|\mathbf{I} - \mathbf{D}_{i,0}\|_\infty + \|\mathbf{D}_{i,1}\|_\infty^2 \|\mathbf{D}_{i,2}^{-1}\|_\infty. \tag{3.76}$$

Hence, to show $\|\mathbf{I} - \mathbf{S}_i\|_\infty < 1$, $\|\mathbf{I} - \mathbf{D}_{i,0}\|_\infty$, $\|\mathbf{D}_{i,1}\|_\infty$, and $\|\mathbf{D}_{i,2}^{-1}\|_\infty$ need to be bounded.

Plugging in the bounds in (3.72), and (3.73), we have

$$\|\mathbf{I} – \mathbf{S}_i\|_\infty \leq 1 + \frac{d_0 + d_1^2 d_4 - 1}{i} = 1 + \frac{8.747 \times 10^{-3} - 1}{i} < 1, \tag{3.77}$$

which implies that $\mathbf{S}_i$ is invertible. □

3.7.8 Proof for Theorem 3.4.2

For simplicity, we assume $K = 2$ in this section. But the theorem can be generalized to $K \geq 2$ if the separation condition is satisfied. Based on the assumption $|\mathbf{x}_{w_1}(i)| = |\mathbf{x}_{w_2}(i)| = 1/\sqrt{N_f}$ for $\forall i \in \{1, ..., N_f\}$, as long as each entry in the constructed dual polynomial vector satisfies $|\boldsymbol{\psi}^i(w; w_1, w_2)| < 1/\sqrt{N_f}$, then $\|\boldsymbol{\psi}(w)\|_2 < 1$. Therefore, the bounds in Lemma 4.3 (2)

further indicate $|\boldsymbol{\psi}^i(w;w_1,w_2)|$ (denote $c_\alpha := 1.008824$, $c_\beta := 3.294\times 10^{-2}$, $c := \frac{1}{\sqrt{N_f}}$)

$$
\begin{aligned}
&|\boldsymbol{\psi}^i(w;w_1,w_2)| = |\sum_{k\in\{1,2\}} \alpha_{k,i}K_i(w-w_k)+\beta_{k,i}K_i'(w-w_k)| \\
&\le \|\alpha_i\|_\infty \sum_{k\in\{1,2\}} |K_i(w-w_k)| + \|\beta_i\|_\infty \sum_{k\in\{1,2\}} |K_i'(w-w_k)| \\
&\le c[ic_\alpha \sum_{k\in\{1,2\}} \frac{|K_1(i(w-w_k))|}{i} + \frac{c_\beta}{f_c}\sum_{k\in\{1,2\}} |K_1'(i(w-w_k))|] \\
&= c[c_\alpha \sum_{k\in\{1,2\}} |K_1(i(w-w_k))| + \frac{c_\beta}{f_c}\sum_{k\in\{1,2\}} |K_1'(i(w-w_k))|] \\
&= c[\sum_{k\in\{1,2\}} c_\alpha |K_1(i(w-w_k) \mod 1)| + \frac{c_\beta}{f_c}|K_1'(i(w-w_k) \mod 1)|].
\end{aligned}
\tag{3.78}
$$

When $i = 1$,

$$
|\boldsymbol{\psi}^1(w;w_1,w_2)| \le c[c_\alpha \sum_{k\in\{1,2\}} |K_1(w-w_k)| + \frac{c_\beta}{f_c}\sum_{k\in\{1,2\}} |K_1'(w-w_k)|]. \tag{3.79}
$$

We show $c[c_\alpha \sum_{k\in\{1,2\}} |K_1(w-w_k)| + \frac{c_\beta}{f_c}\sum_{k\in\{1,2\}} |K_1'(w-w_k)|] < \frac{1}{\sqrt{N_f}}$ by applying [20, Lemma 2.3 and 2.4]. We consider both the near and far regions. The near region $\mathcal{T}_{\text{near}}$ and far region $\mathcal{T}_{\text{far}}$ are defined as $\mathcal{T}_{\text{near}} := \cup_{k=1}^2 [w_k-\nu, w_k+\nu]$ and $\mathcal{T}_{\text{far}} := [0,1]\backslash\mathcal{T}_{\text{near}}$, where $\nu = \frac{0.1649}{f_c}$.

For $\mathcal{T}_{\text{far}}$, based on [20, Lemma 2.4]

$$
\begin{aligned}
&c_\alpha \sum_{k\in\{1,2\}} |K_1(w-w_k)| + \frac{c_\beta}{f_c}\sum_{k\in\{1,2\}} |K_1'(w-w_k)| \\
&\le 0.99992 < 1.
\end{aligned}
\tag{3.80}
$$

Therefore,

$$
|\boldsymbol{\psi}^1(w;w_1,w_2)| \le c[c_\alpha \sum_{k\in\{1,2\}} |K_1(w-w_k)| + \frac{c_\beta}{f_c}\sum_{k\in\{1,2\}} |K_1'(w-w_k)|] < c.
$$

If $i > 1$, the only difference between the last line of (3.78) and the right hand side of (3.79) is the dilation of K_1 and K_1'. This indicates the i-th entry is a special case for $i = 1$. Therefore,

$|\boldsymbol{\psi}^i(w;w_1,w_2)| < c = 1/\sqrt{N_f}$ will also hold for $i > 1$. Hence, in $\mathcal{T}_{\text{far}}$, $\|\boldsymbol{\psi}(w)\|_2 < 1$ for $w \notin \mathcal{W}$.

For $\mathcal{T}_{\text{near}}$, inspired by the proof in [20, Lemma 2.3], we show the strict concavity of $|\boldsymbol{\psi}^i(w;w_1,w_2)|$. We have

$$\begin{aligned} &\boldsymbol{\psi}_R^i(w)\boldsymbol{\psi}_R^{i''}(w) + |\boldsymbol{\psi}^{i'}(w)|^2 + |\boldsymbol{\psi}_I^i(w)||\boldsymbol{\psi}_I^{i''}(w)| \\ &\leq -9.291 \times 10^{-2}(if_c/\sqrt{N_f})^2 < 0 \end{aligned} \tag{3.81}$$

and

$$\begin{aligned} &\frac{\mathrm{d}^2|\boldsymbol{\psi}^i|(w)}{\mathrm{d}w^2} = -\frac{(\boldsymbol{\psi}_R^i(w)\boldsymbol{\psi}_R^{i'}(w) + \boldsymbol{\psi}_I^i(w)\boldsymbol{\psi}_I^{i'}(w))^2}{|\boldsymbol{\psi}^i(w)|^3} \\ &+ \frac{\boldsymbol{\psi}_R^i(w)\boldsymbol{\psi}_R^{i''}(w) + |\boldsymbol{\psi}^{i'}(w)|^2 + |\boldsymbol{\psi}_I^i(w)||\boldsymbol{\psi}_I^{i''}(w)|}{|\boldsymbol{\psi}^i(w)|} < 0. \end{aligned} \tag{3.82}$$

Since $\boldsymbol{\psi}^{i'}(w_1) = \boldsymbol{\psi}^{i'}(w_2) = 0$, local strict concavity will imply $|\boldsymbol{\psi}^i(w;w_1,w_2)| < 1/\sqrt{N_f}$ in $\mathcal{T}_{\text{near}}$. □

Acknowledgement

The text of this chapter is in full reprint of the material as it appears in Yifan Wu, Michael B. Wakin, and Peter Gerstoft, "Gridless DOA Estimation with Multiple Frequencies", *IEEE Transactions on Signal Processing*, 71, 417 - 432. The dissertation author was the primary researcher and author of this chapter. The co-authors listed in these publications directed and supervised the research.

Bibliography

[1] H. L. Van Trees, *Optimum array processing: Part IV of detection, estimation, and modulation theory* (John Wiley & Sons, 2004).

[2] K. Venugopal, A. Alkhateeb, N. G. Prelcic, and R. W. Heath, "Channel estimation for hybrid architecture-based wideband millimeter wave systems," IEEE J. Sel. Areas Commun. **35**(9), 1996–2009 (2017).

[3] Y. Wei, Y. Li, Z. Ding, Y. Wang, T. Zeng, and T. Long, "SAR parametric super-resolution image reconstruction methods based on admm and deep neural network," IEEE Trans. Geosci. Remote Sens. **59**(12), 10197–10212 (2021).

[4] R. O. Schmidt, "Multiple emitter location and signal parameter estimation," IEEE Trans. Antennas Propagat. **34**(3), 276–280 (1986).

[5] R. Roy and T. Kailath, "Esprit-estimation of signal parameters via rotational invariance techniques," IEEE Trans. Acoust., Speech, and Signal Process. **37**(7), 984–995 (1989).

[6] M. Wax, T. Shan, and T. Kailath, "Spatio-temporal spectral analysis by eigenstructure methods," IEEE Trans. Acoust., Speech, Signal Process. **32**(4), 817–827 (1984).

[7] H. Wang and M. Kaveh, "Coherent signal-subspace processing for the detection and estimation of angles of arrival of multiple wideband sources," IEEE Trans. Acoust., Speech, Signal Process. **33**(4), 823–831 (1985).

[8] K. M. Buckley and L. J. Griffiths, "Broad-band signal-subspace spatial-spectrum (BASS-ALE) estimation," IEEE Trans. Acoust., Speech, Signal Process. **36**(7), 953–964 (1988).

[9] E. D. Di C. and R. Parisi, "WAVES: Weighted average of signal subspaces for robust wideband direction finding," IEEE Trans. Signal Process. **49**(10), 2179–2191 (2001).

[10] Y. Yoon, L. M. Kaplan, and J. H. McClellan, "TOPS: New DOA estimator for wideband signals," IEEE Trans. Signal Process. **54**(6), 1977–1989 (2006).

[11] J. Zhang, N. Hu, M. Bao, X. Li, and W. He, "Wideband DOA estimation based on block FOCUSS with limited samples," in *IEEE GlobalSIP* (2013), pp. 634–637.

[12] L. Wang, L. Zhao, G. Bi, C. Wan, L. Zhang, and H. Zhang, "Novel wideband DOA estimation based on sparse Bayesian learning with Dirichlet process priors," IEEE Trans. Signal Process. **64**(2), 275–289 (2015).

[13] C. Liu, Y. V. Zakharov, and T. Chen, "Broadband underwater localization of multiple sources using basis pursuit denoising," IEEE Trans. Signal Process. **60**(4), 1708–1717 (2011).

[14] Z. Tang, G. Blacquiere, and G. Leus, "Aliasing-free wideband beamforming using sparse signal representation," IEEE Trans. Signal Process. **59**(7), 3464–3469 (2011).

[15] K. L. Gemba, S. Nannuru, P. Gerstoft, and W. S. Hodgkiss, "Multi-frequency sparse Bayesian learning for robust matched field processing," J. Acoust. Soc. Am. **141**(5), 3411–3420 (2017).

[16] N. Antonello, E. De Sena, M. Moonen, P. A. Naylor, and T. van Waterschoot, "Joint acoustic localization and dereverberation through plane wave decomposition and sparse regularization," IEEE/ACM Trans. Audio, Speech, Lang. Process. **27**(12), 1893–1905 (2019).

[17] S. Nannuru, K. L. Gemba, P. Gerstoft, W. S. Hodgkiss, and C. F. Mecklenbräuker, "Sparse bayesian learning with multiple dictionaries," Signal Process. **159**, 159–170 (2019).

[18] K. L. Gemba, S. Nannuru, and P. Gerstoft, "Robust ocean acoustic localization with sparse Bayesian learning," IEEE J. Sel. Topics Signal Process. **13**(1), 49–60 (2019).

[19] V. Chandrasekaran, B. Recht, P. A. Parrilo, and A. S. Willsky, "The convex geometry of linear inverse problems," Found. Comput. Math. **12**(6), 805–849 (2012).

[20] E. J. Candès and C. Fernandez-Granda, "Towards a mathematical theory of super-resolution," Commun. Pure Appl. Math. **67**(6), 906–956 (2014).

[21] G. Tang, B. N. Bhaskar, P. Shah, and B. Recht, "Compressed sensing off the grid," IEEE Trans. Inf. Theory **59**(11), 7465–7490 (2013).

[22] Y. Chi and Y. Chen, "Compressive two-dimensional harmonic retrieval via atomic norm minimization," IEEE Trans. Signal Process. **63**(4), 1030–1042 (2014).

[23] Y. Li and Y. Chi, "Off-the-grid line spectrum denoising and estimation with multiple measurement vectors," IEEE Trans. Signal Process. **64**(5), 1257–1269 (2015).

[24] C. Fernandez-Granda, "Super-resolution of point sources via convex programming," Inf. Inference, J. IMA **5**(3), 251–303 (2016).

[25] Y. Chi, "Guaranteed blind sparse spikes deconvolution via lifting and convex optimization," IEEE J. Sel. Topics Signal Process. **10**(4), 782–794 (2016).

[26] Z. Yang and L. Xie, "Exact joint sparse frequency recovery via optimization methods," IEEE Trans. Signal Process. **64**(19), 5145–5157 (2016).

[27] D. Yang, G. Tang, and M. B. Wakin, "Super-resolution of complex exponentials from modulations with unknown waveforms," IEEE Trans. Inf. Theory **62**(10), 5809–5830 (2016).

[28] S. Li, D. Yang, G. Tang, and M. B. Wakin, "Atomic norm minimization for modal analysis from random and compressed samples," IEEE Trans. Signal Process. **66**(7), 1817–1831 (2018).

[29] Z. Yang and L. Xie, "Enhancing sparsity and resolution via reweighted atomic norm minimization," IEEE Trans. Signal Process. **64**(4), 995–1006 (2015).

[30] Z. Yang, J. Tang, Y. C. Eldar, and L. Xie, "On the sample complexity of multichannel frequency estimation via convex optimization," IEEE Trans. Inf. Theory **65**(4), 2302–2315 (2018).

[31] M. Wagner, Y. Park, and P. Gerstoft, "Gridless DOA estimation and root-MUSIC for non-uniform linear arrays," IEEE Trans. Signal Process. **69**, 2144–2157 (2021).

[32] Y. Park and P. Gerstoft, "Gridless sparse covariance-based beamforming via alternating projections including co-prime arrays," J. Acoust. Soc. Am. **151**(6), 3828–3837 (2022).

[33] Z. M. Liu, Z. T. Huang, and Y. Y. Zhou, "An efficient maximum likelihood method for direction-of-arrival estimation via sparse Bayesian learning," IEEE Trans. Wireless Comm. **11**(10), 1–11 (2012) doi: 10.1109/TWC.2012.090312.111912.

[34] P. Chen, Z. Chen, Z. Cao, and X. Wang, "A new atomic norm for DOA estimation with gain-phase errors," IEEE Trans. Signal Process. **68**, 4293–4306 (2020).

[35] S. Li, P. Nayeri, and M. B. Wakin, "Digital beamforming robust to time-varying carrier frequency offset," arXiv preprint arXiv:2103.04948 (2021).

[36] A. Xenaki and P. Gerstoft, "Grid-free compressive beamforming," J. Acoust. Soc. Am. **137**, 1923–1935 (2015).

[37] S. Li, D. Gaydos, P. Nayeri, and M. B. Wakin, "Adaptive interference cancellation using atomic norm minimization and denoising," IEEE Antennas Wirel. Propag. Lett. **19**(12), 2349–2353 (2020).

[38] B. N. Bhaskar, G. Tang, and B. Recht, "Atomic norm denoising with applications to line spectral estimation," IEEE Trans. Signal Process. **61**(23), 5987–5999 (2013).

[39] S. Li, M. B. Wakin, and G. Tang, "Atomic norm denoising for complex exponentials with unknown waveform modulations," IEEE Trans. Inf. Theory **66**(6), 3893–3913 (2019).

[40] Y. Xie, M. B. Wakin, and G. Tang, "Simultaneous sparse recovery and blind demodulation," IEEE Trans. Signal Process. **67**(19), 5184–5199 (2019).

[41] Y. Xie, M. B. Wakin, and G. Tang, "Support recovery for sparse signals with unknown non-stationary modulation," IEEE Trans. Signal Process. **68**, 1884–1896 (2020).

[42] Y. Chi and M. F. Da Costa, "Harnessing sparsity over the continuum: Atomic norm minimization for superresolution," IEEE Signal Process. Mag. **37**(2), 39–57 (2020).

[43] J. W. Helland, *Atomic Norm Algorithms for Blind Spectral Super-resolution Problems* (Colorado School of Mines, 2019).

[44] B. Dumitrescu, *Positive trigonometric polynomials and signal processing applications*, Vol. 103 (Springer, 2017).

[45] Z. Yang, "A gridless sparse method for super-resolution of harmonics," in *IEEE EUSIPCO* (2017), pp. 2096–2100.

[46] Y. Wu, M. B. Wakin, and P. Gerstoft, "Gridless doa estimation with multiple frequencies," arXiv preprint arXiv:2207.06159 (2022).

[47] S. Boyd and L. Vandenberghe, *Convex optimization* (Cambridge university press, 2004).

[48] M. Grant and S. Boyd, "CVX: Matlab software for disciplined convex programming, version 2.1," (2014).

[49] Y. Liang, W. Liu, Q. Shen, W. Cui, and S. Wu, "A review of closed-form Cramér-Rao bounds for DOA estimation in the presence of Gaussian noise under a unified framework," IEEE Access **8**, 175101–175124 (2020).

Chapter 4

Non-uniform Array and Frequency Spacing for Regularization-free Gridless DOA

Gridless direction-of-arrival (DOA) estimation with multiple frequencies can be applied in acoustics source localization problems. We formulate this as an atomic norm minimization (ANM) problem and derive an equivalent *regularization-free* semi-definite program (SDP) thereby avoiding regularization bias. The DOA is retrieved using a Vandermonde decomposition on the Toeplitz matrix obtained from the solution of the SDP. We also propose a fast SDP program to deal with non-uniform array and frequency spacing. For non-uniform spacings, the Toeplitz structure will not exist, but the DOA is retrieved via irregular Vandermonde decomposition (IVD), and we theoretically guarantee the existence of the IVD. We extend ANM to the multiple measurement vector (MMV) cases and derive its equivalent regularization-free SDP. Using multiple frequencies and the MMV model, we can resolve more sources than the number of physical sensors *for a uniform linear array*. Numerical results demonstrate that the regularization-free framework is robust to noise and aliasing, and it overcomes the regularization bias.

4.1 Introduction

Direction-of-arrival (DOA) estimation is an important topic in sensor array processing [1] that has a broad range of applications in wireless communication [2], radar [3], remote sensing, etc. Conventional DOA estimation methods (e.g. multiple signal classification (MUSIC) [4], and estimation of signal parameters via rotational invariant techniques (ESPRIT) [5]) are mainly developed for narrowband signals. In the past few decades, some wideband DOA estimation methods have been proposed [6–16]. Recently proposed methods based on sparse recovery and a multi-frequency model [8, 10] have demonstrated superior performance in wideband DOA estimation problems. Before introducing the contributions of this paper, we review the relevant prior works.

4.1.1 Related Work

Wideband DOA Estimation and Multiple Frequencies

Wideband signal DOA estimation has been studied for decades [6, 11–14]. In [6], a subspace-based wideband DOA estimation approach, the incoherent signal subspace method (ISSM), was proposed. The coherent signal subspace method (CSSM) [11] led to improved performance compared to ISSM. A broadband spatial-spectrum estimation approach [12] overcame the peak bias and source spectral content sensitivity from CSSM. Variants of CSSM, such as the weighted average of signal subspaces method [13] and the test of orthogonality of projected subspaces method [14] were also proposed. Recently, some wideband DOA estimation methods based on sparse recovery have also been developed [7–10, 15–19]. These sparsity-based methods have demonstrated superior performance compared to conventional methods and generally require much fewer samples.

The multi-frequency model [7–10, 15, 16] has shown success in modeling wideband signals. The multi-frequency model uses N_f (rather than 1) temporal frequency bins in a frequency

set $\{F_1, \ldots, F_{N_f}\}$ to characterize a wideband signal. All these frequencies are used for estimation, as opposed to using a single frequency under the narrowband model. One challenge for multi-frequency processing is aliasing [8, 10], which will be present when the receiver spacing is greater than the half wavelength of the highest frequency. The performance of a DOA estimation method may degrade significantly in the presence of aliasing. In [15], the authors present an aliasing-free DOA estimation method based on sparse signal recovery. In [8, 9, 16], wideband signal DOA estimation based on sparse Bayesian learning (SBL) with multiple frequencies is proposed [8] and applied to matched field processing [16] and robust ocean acoustic localization [9]. A joint localization and dereverberation method based on sparse regularization is also proposed in [7] for room source localization and tracking.

Atomic Norm Minimization (ANM)

ANM was initially proposed in [20] as a general framework for promoting sparse signal decompositions. The main benefit of ANM is that it overcomes the grid mismatch error that plagues grid-based methods. The pioneering ANM paper [21] proposed an optimization-based continuous (temporal) frequency estimation method and provided a theoretical guarantee when full data are available. The authors in [22] studied continuous temporal frequency estimation based on randomly sampled data for the single measurement vector (SMV) case. ANM for multiple measurement vectors (MMVs) under the uniform (or equispaced) time samples (analogous to a uniform linear array, or ULA) setup was studied in [23–25], and it was extended to the non-uniform array (NUA) setting in [26]. It was also extended to multiple frequencies for wideband DOA estimation in [10, 27]. The sample complexity of modal analysis with random temporal compression was established in [28]. We refer readers to [29] for a comprehensive overview of ANM and its applications.

Non-uniform Array and More Sources than Sensors

An NUA enables the possibility to resolve more sources than the number of physical sensors. Early works involving NUA include the minimum redundancy array (MRA) [30], and the minimum holes array (MHA) [31]. For a given number of sources, MRA and MHA require an extensive search through all possible sensor combinations to find the optimal design. Recently, a new structure of NUA, known as a co-prime array [32], was developed. The co-prime array has a closed-form expression for the sensor positions so that the exhaustive search over the sensor combinations is avoided. The nested array [33] and co-array [34] based approaches were also proposed to detect more sources than the number of sensors.

An alternative way to resolve more sources than sensors is to use fourth-order cumulants [35, 36]. However, this approach is limited to non-Gaussian sources. In [37], with the help of the Khatri-Rao (KR) product and assuming quasi-stationary sources, it was shown that one can identify up to $2N-1$ sources using an N-element ULA without computing higher-order statistics. Unfortunately, the quasi-stationary assumption is not applicable to stationary sources.

4.1.2 Our Contributions

In previous work [10], we developed a gridless DOA estimation method for the multi-frequency model based on ANM. This was formulated as a semi-definite program (SDP) problem so that ANM is solved using off-the-shelf SDP solvers, e.g., CVX [38]. The DOAs are retrieved by finding the roots of the dual polynomial. The dual polynomial served as a certificate for the optimality and an interpolation method that constructed the dual certificate was presented.

In this work, we propose a wideband DOA estimation framework that significantly expands the applicability from [10]. Our contribution is summarized in the following respects (see also Table 4.1).

Regularization-free Framework

An SDP that is equivalent to ANM is formulated in [10] based on the dual atomic norm and the definition of the dual polynomial in the noise-free case. When noise is present, a common strategy in ANM works is giving some tolerance to the constraints using regularization in the SDP [22, 24, 39]. In addition to the challenges from the noise, [10] shows that for array spacing above half a wavelength of the highest frequency and with multiple sources, the performance may degrade remarkably due to a phenomenon termed near collision [10]. To mitigate near collisions, an $\ell_{1,2}$ regularization term is added. Although these regularization terms prevent failures due to noise or near collisions, they lead to bias. The performance of ANM degrades due to such bias compared to the competing method SBL [40], especially at a low signal-to-noise ratio (SNR).

Although most ANM works promote robustness to noise by adding a regularization term, [26] demonstrates that it is possible to deal with the noise by solving a noise-free optimization problem. In [26], the authors propose a two-step DOA estimation approach. The first step is to apply the alternating projection (AP) algorithm to solve a *noise-free* optimization problem and obtain a matrix with an irregular Toeplitz structure. The second step computes an irregular Vandermonde decomposition (achieved by generalized root-MUSIC) to retrieve the DOAs from the irregular Toeplitz matrix. Although the optimization problem solved in the first step does not have explicit robustness to the noise, the second step enables the method to work in noisy cases. This method effectively avoids the explicit bias and the non-trivial effort required to tune the regularization parameter.

Inspired by [26], we formulate the dual problem of the *noise-free* SDP in [10, eq. (20)] *without regularization*. This problem is again an SDP and we deem it as the *primal domain SDP* (since [10] formulates its SDP in the dual domain). Solving this SDP gives a Toeplitz matrix, and the DOAs are further retrieved by Vandermonde decomposition of this Toeplitz matrix. One computational method for Vandermonde decomposition is root-MUSIC [41], and it has robustness to both noise and near collisions. Therefore, with the help of "post-SDP processing"

(root-MUSIC), regularization is avoided and no prior knowledge of the noise is needed. At low SNRs in simulation, the method can achieve a better performance than competing methods, and it approaches closer to the Cramér-Rao bound (CRB) for Gaussian noise.

Non-uniform Frequencies and Irregular Vandermonde Decomposition

We also develop a fast SDP for the primal domain SDP. The fast SDP is derived based on the dual problem of the fast algorithm in [10]. The fast algorithm can not only improve the speed but also can extend the method to the non-uniform frequency (NUF) case. In this case, the DOAs are encoded in a matrix with an *irregular Toeplitz* structure. We apply the irregular Vandermonde decomposition (IVD) [26] to this matrix to retrieve the DOAs. Furthermore, we provide a theoretical guarantee for the existence of the IVD which is not shown in [26]. While it is mentioned in [10] that the fast dual algorithm proposed therein can be applied to the NUF case, this is not tested in [10], and our experiments (see Fig. 4.5) indicate that the fast primal method is more effective.

Multiple Snapshots and More Sources Than Sensors

The method in [10] is developed under the SMV case. Prior works show that MMVs can give improved performance [23, 24, 42]. That motivates us to extend the framework in [10] to the MMV case. In the MMV setting, the received signal from the sensor array is a three-dimensional tensor (sensors $\times$ snapshots $\times$ frequencies). Based on the signal model, we formulate the corresponding ANM problem and derive the SDP (in the dual domain) that is equivalent to the ANM. The dual problem of the SDP is then derived to obtain the SDP in the primal domain. The purpose of the primal SDP is to enhance the robustness to the noise and near collision without regularization.

The multi-frequency setup also enables resolving more sources than sensors case in the ULA setting. The maximum number of uniquely identifiable sources in an N_M-element ULA

Table 4.1: Comparison of [10] and this work.

	[10]	This work
Assumption	ULA and uniform frequency	NUA and NUF
Procedure	Dual SDP $\rightarrow$ Polynomial rooting	Primal SDP $\rightarrow$ IVD
Model	SMV	MMV
Noise-free SDPs	Dual uniform (20) (SDP equivalent to ANM) Fast dual (27)-(28) (extension of (20); nonuniform not tested) Full-dimension primal (29) (dual of (20); uniform case)	Dual uniform (4.13) (SDP equivalent to MMV-MF ANM) Fast dual (4.17) (extension of(4.13); accommodates NUA/NUF) Fast primal (4.19) (dual of (4.17); accommodates NUA/NUF) Fast SMV primal (4.23) (special case of (4.19) when $N_l = 1$) Full-dimension primal (4.24) (dual of (4.13); uniform case)
Noisy SDPs	Dual uniform (21) (robust version of (20))	Dual uniform (4.15) (robust version of (4.13))

is $N_M - 1$ [42, Sec. 11.2.3] for the single-frequency case. Co-prime array techniques [32] can break through such a limit with a carefully designed array structure, enabling the resolution of more sources than the number of sensors. We show that it is possible to resolve more sources than sensors *with a ULA under the multi-frequency model*. The physical intuition is that multiple frequencies increase the diversity of the harmonics and these "new harmonics" can serve as extra "virtual sensors" in a large virtual array. Due to this intrinsic property, it is possible to break through such a bottleneck in the ULA setup. In many practical scenarios, the array geometry is fixed and ULA is one of the most commonly used arrays. This result has a practical impact and demonstrates the benefit of multi-frequency processing.

In summary, the framework proposed is superior to [10] in terms of generality, practicality, performance, and complexity. Our work also demonstrates the possibility of resolving more sources than sensors *under the ULA setup* which is an important merit of the multi-frequency model.

4.1.3 Notation

Throughout the paper, the following notation is adopted. Boldface letters are used to represent matrices and vectors. Conventional notations $(\cdot)^T$, $(\cdot)^H$, $(\cdot)^*$, $\langle \cdot, \cdot \rangle_{\mathbb{R}}$, and $\langle \cdot, \cdot \rangle$ stand for matrix/vector transpose, Hermitian transpose, complex conjugate, real inner product, and inner product, respectively. $\mathrm{Tr}(\cdot)$ is used to represent the trace of a matrix. $\|\cdot\|_p$, $\|\cdot\|_F$, and $\|\cdot\|_{\mathrm{HS}}$ are

used to express vector ℓ_p norm, matrix Frobenius norm, and Hilbert-Schmidt norm for the tensor (for a 3D tensor $\|\mathcal{A}\|_{\text{HS}} = \sqrt{\sum_{ijk} |a_{ijk}|^2}$). For a Hermitian matrix $\mathbf{A}$, $\mathbf{A} \succeq 0$ means $\mathbf{A}$ is a positive semidefinite matrix. The imaginary unit is denoted by $j = \sqrt{-1}$.

4.2 Preliminaries

When multiple snapshots are available, DOA estimation methods can have improved performance [23, 24, 42]. In this section, we extend the SMV multi-frequency ANM framework for gridless DOA estimation from [10] to the MMV setting; we refer to the resulting framework as the *MMV-MF model*. This model will help us explore the possibility of having more sources than the sensors in Sec. 4.5.

4.2.1 Assumptions

The following assumptions are made for the array configuration and signal model:

1. The sensors comprise a linear array with positions drawn from a uniform grid $\{0, 1, \ldots, N_M - 1\} \cdot d$, where d is the sensor spacing unit. We let $\mathcal{M} \subseteq \{0, 1, \ldots, N_M - 1\}$ denote the indices of the actual sensors; the resulting positions are thus $\{m \cdot d | m \in \mathcal{M}\}$. We define $N_m := |\mathcal{M}| \leq N_M$ as the number of sensors. When all sensors are present, $N_m = N_M$, and we have a *uniform linear array (ULA)* case. When only some sensors are present, $N_m < N_M$, and we have a *nonuniform array (NUA)* case.

2. The sources have temporal frequency components drawn from a uniform grid $\{1, \ldots, N_F\} \cdot F_1$, where F_1 is the spacing between frequencies. Let $\lambda_1 := c/F_1$ denote the wavelength corresponding to F_1, where c is the propagation speed. We assume $\lambda_1 = 2d$ where d is the sensor spacing unit above; equivalently, $d = \frac{c}{2F_1}$. This spacing is for simplifying the derivation and can be relaxed to any $d \leq \frac{\lambda_1}{2}$ (see [10] for details). We let $\mathcal{F} \subseteq \{1, \ldots, N_F\}$ denote the

indices of the active source frequencies; the resulting frequencies are thus $\{f \cdot F_1 | f \in \mathcal{F}\}$ and the wavelengths are $\{\lambda_1/f | f \in \mathcal{F}\}$. We define $N_f := |\mathcal{F}| \leq N_F$ to be the number of active source frequencies. When all frequencies are active, $N_f = N_F$, and we refer to this as the *uniform frequency* case. When only some frequencies are active, $N_f < N_F$, and we refer to this as the *nonuniform frequency (NUF)* case.

3. Suppose there are N_l snapshots (time samples) received by each sensor. The source amplitude for the f-th frequency ($f \in \mathcal{F}$) is $\mathbf{x}_w(f) = [x_w^{(1)}(f) \ \ldots \ x_w^{(N_l)}(f)]^T \in \mathbb{C}^{N_l}$.

4. There are K active uncorrelated sources impinging on the array from unknown directions of arrival (DOAs) θ, or in directional cosines

$$w := F_1 d \cos(\theta)/c = \cos(\theta)/2. \tag{4.1}$$

4.2.2 MMV-MF Model

We begin by considering the case of a ULA with uniform frequencies, i.e., $N_m = N_M$ and $N_f = N_F$. (We incorporate the NUA and NUF cases in Section 4.4.) The received signals can be arranged into a tensor $\mathcal{Y} \in \mathbb{C}^{N_M \times N_l \times N_F}$ (sensors $\times$ snapshots $\times$ frequencies) with the following structure:

$$\mathcal{Y} = \mathcal{X} + \mathcal{N} \tag{4.2}$$

$$\begin{aligned} \mathcal{X} &= \sum_w c_w [\mathbf{a}(1,w)\mathbf{x}_w^T(1) | \ldots | \mathbf{a}(N_F,w)\mathbf{x}_w^T(N_F)] \\ &= \sum_w c_w \mathbf{A}(w) * \mathbf{X}_w^T \end{aligned} \tag{4.3}$$

where $\mathbf{a}(f,w) = [1 \ e^{-j2\pi wf} \ldots e^{-j2\pi wf(N_M-1)}]^T = [1 \ z^f \ldots z^{f(N_M-1)}]^T \in \mathbb{C}^{N_M}$ ($z := e^{-j2\pi w}$) is the array manifold vector for the f-th frequency. $\mathcal{N} \in \mathbb{C}^{N_M \times N_l \times N_F}$ denotes additive Gaussian uncorrelated noise in (4.2). Denote $\mathbf{A}(w) = [\mathbf{a}(1,w) \ldots \mathbf{a}(N_F,w)] \in \mathbb{C}^{N_M \times N_F}$ and $\mathbf{X}_w = [\mathbf{x}_w(1) \ldots \mathbf{x}_w(N_F)]^T \in \mathbb{C}^{N_F \times N_l}$. $\mathbf{A}(w) * \mathbf{X}_w^T$ is the "reshaped Khatri-Rao product" defined as

$[\mathbf{A}(w) * \mathbf{X}_w^T]_{::f} := \mathbf{a}(f,w)\mathbf{x}_w^T(f)$ $(f = 1,...,N_F)$. When $N_l = 1$, the above matches the SMV model in [10].

Finally, we define

$$N = N_F(N_M - 1) + 1, \tag{4.4}$$

noting that $N_F(N_M - 1)$ appears in the largest exponent of any array manifold vector used in the MMV-MF model. Consequently, N will determine the size of certain SDP formulations such as (4.13).

4.2.3 Collision and Near Collision

A challenge for multi-frequency processing is the risk of a phenomenon known as *collision*, which occurs when, at some frequencies, the array manifold vectors for two DOAs coincide due to aliasing. Two DOAs w_1 and w_2 are said to have a *collision* in the f-th frequency if [10, eq. (46)]

$$\mathbf{a}(f,w_1) = \mathbf{a}(f,w_2). \tag{4.5}$$

Such a collision occurs whenever w_1 and w_2 satisfy [10, eq. (47)]

$$|w_1 - w_2| = \frac{k}{f} \quad (f \in \mathcal{F}, f > 1). \tag{4.6}$$

A *near collision* is said to occur when [10, eq. (50)]

$$|w_1 - w_2| \approx \frac{k}{f} \quad (f \in \mathcal{F}, f > 1). \tag{4.7}$$

4.2.4 Irregular Vandermonde and Toeplitz Matrices

Define some real-valued vector $\boldsymbol{\gamma} = [\gamma_1 \dots \gamma_{N_\gamma}]^T \in \mathbb{Z}^{N_\gamma}$, complex-valued vector $\mathbf{z} = [z_1 \dots z_{N_z}]^T \in \mathbb{C}^{N_z}$, and $\mathbf{w}(\boldsymbol{\gamma}, z) := [z^{\gamma_1} \dots z^{\gamma_{N_\gamma}}]^T$. For arbitrary dimensions N_γ and N_z, an *irregular Vandermonde*

matrix of size $N_\gamma \times N_z$ is a matrix having the form [26, eq. (25)]

$$\begin{aligned}\mathbf{W} = \mathbf{W}(\boldsymbol{\gamma}, \mathbf{z}) &= [\mathbf{z}^{\gamma_1} \dots \mathbf{z}^{\gamma_{N_\gamma}}]^T \\ &= [\mathbf{w}(\boldsymbol{\gamma}, z_1) \dots \mathbf{w}(\boldsymbol{\gamma}, z_{N_z})].\end{aligned} \tag{4.8}$$

Note that when the entries of $\boldsymbol{\gamma}$ form an arithmetic progression, specifically $\boldsymbol{\gamma} = [0 \dots N_\gamma - 1]^T$, $\mathbf{W}(\boldsymbol{\gamma}, \mathbf{z})$ forms a regular Vandermonde matrix.

An (N_γ, N_z)-*irregular Toeplitz matrix* is any matrix $\mathbf{T} \in \mathbb{C}^{N_\gamma \times N_\gamma}$ that can be constructed from an irregular Vandermonde matrix as follows [26, eq. (27)]:

$$\mathbf{T} = \mathbf{W}(\boldsymbol{\gamma}, \mathbf{z}) \mathbf{D} \mathbf{W}(\boldsymbol{\gamma}, \mathbf{z})^H, |\mathbf{z}| = 1, \tag{4.9}$$

where $\boldsymbol{\gamma} \in \mathbb{Z}^{N_\gamma}$ and $\mathbf{z} \in \mathbb{C}^{N_z}$, and where $\mathbf{D} \in \mathbb{R}^{N_z \times N_z}$ is a diagonal matrix. We refer to (4.9) as an *irregular Vandermonde decomposition (IVD)*. Note that any $N_\gamma \times N_\gamma$ positive semi-definite regular Toeplitz matrix $\mathbf{T}$ with rank N_z has a regular Vandermonde decomposition of the form (4.9) in which $\boldsymbol{\gamma} \in \mathbb{Z}^{N_\gamma}$ is an arithmetic progression.

4.3 Atomic Norm Minimization for MMV-MF

In this section, we formulate the atomic norm minimization problem for the MMV-MF model. Then, we derive an equivalent SDP that makes the proposed framework computationally feasible.

Define the atomic set

$$\mathcal{A} = \{\mathbf{A}(w) * \mathbf{X}_w^T \mid w \in [-1/2, 1/2], \|\mathbf{X}_w\|_F = 1\}. \tag{4.10}$$

The atomic norm of a tensor $\mathcal{X} \in \mathbb{C}^{N_M \times N_l \times N_F}$ is defined as $\|\mathcal{X}\|_{\mathcal{A}} := \inf\{\sum_w |c_w| \big| \mathcal{X} = c_w \mathbf{A}(w) *$

$\mathbf{X}_w^T \mid \|\mathbf{X}_w\|_F = 1\}$. The *atomic norm minimization (ANM)* problem for the noise-free case can be expressed as

$$\min_{\mathcal{X}} \quad \|\mathcal{X}\|_{\mathcal{A}} \quad \text{s.t.} \quad \mathcal{Y} = \mathcal{X}. \tag{4.11}$$

When noise is present, the optimization problem is modified to relax the equality constraint:

$$\min_{\mathcal{X}} \quad \|\mathcal{X}\|_{\mathcal{A}} \quad \text{s.t.} \quad \|\mathcal{Y} - \mathcal{X}\|_{\text{HS}} \leq \eta. \tag{4.12}$$

The following proposition guarantees that (4.11) is equivalent to an SDP problem.

Proposition 4.3.1 *Problem* (4.11) *is equivalent to the following SDP problem*

$$\begin{aligned} &\max_{\mathcal{Q},\mathbf{P}_0} \langle \mathcal{Q}, \mathcal{Y} \rangle_{\mathbb{R}} \quad s.t. \begin{bmatrix} \mathbf{P}_0 & \widetilde{\mathbf{Q}} \\ \widetilde{\mathbf{Q}}^H & \mathbf{I}_{N_l N_F} \end{bmatrix} \succeq 0, \\ &\sum_{i=1}^{N-k} \mathbf{P}_0(i, i+k) = \delta_k, \widetilde{\mathbf{Q}} = [\mathcal{R}(\mathbf{Q}_1) \dots \mathcal{R}(\mathbf{Q}_{N_F})], \end{aligned} \tag{4.13}$$

where $\mathcal{Q} = [\mathbf{Q}_1 | \dots | \mathbf{Q}_{N_F}] \in \mathbb{C}^{N_M \times N_l \times N_F}$ is the dual variable, $\mathbf{P}_0 \in \mathbb{C}^{N \times N}$, $\widetilde{\mathbf{Q}} = [\widetilde{\mathbf{Q}}_1 \dots \widetilde{\mathbf{Q}}_{N_F}] \in \mathbb{C}^{N \times N_l N_F}$, and $\widetilde{\mathbf{Q}}_f = \mathcal{R}(\mathbf{Q}_f) : N_M \times N_l \to N \times N_l$ is a mapping defined as

$$\mathcal{R}(\mathbf{Q}_f)(i,l) = \begin{cases} \mathbf{Q}_f(m,l) & \text{for } (i,l) = (f(m-1)+1, l) \\ 0 & \text{otherwise.} \end{cases} \tag{4.14}$$

Proof See Appendix 4.9.1.

Fig. 4.1 demonstrates the mapping $\mathcal{R}$. Across all frequencies, $\mathcal{R} : N_M \times N_l \times N_F \to N \times N_l N_F$ is a linear mapping and can be expressed as a tall binary matrix multiply $\text{vec}(\widetilde{\mathbf{Q}}) = \mathbf{R}\,\text{vec}(\mathcal{Q})$. The transpose of the matrix $\mathbf{R}$ describes the behavior of the adjoint operator $\mathcal{R}^* : N \times N_l N_F \to N_M \times N_l \times N_F$, which is also demonstrated in Fig. 4.1.

To provide intuition for the role of $\mathcal{R}$, recall from (4.3) that the array manifold vectors

in the MMV-MF model are frequency-dependent, and so the rows of different slices of $\mathcal{X}$ correspond to different space-frequency products. After lifting the dual variable tensor $\mathcal{Q}$ to a higher-dimensional space, however, every row corresponds to the same space-frequency product $f(m-1)$, allowing $\widetilde{\mathbf{Q}}$ to play a similar role in the SDP to the dual variables in more conventional ANM formulations.

In the noisy case, the equivalent SDP of (4.12) is the regularized version of (4.13):

$$\begin{aligned} &\max_{\mathcal{Q},\mathbf{P}_0} \langle \mathcal{Q}, \mathcal{Y} \rangle_{\mathbb{R}} - \eta \|\mathcal{Q}\|_{\mathrm{HS}} \quad \text{s.t.} \begin{bmatrix} \mathbf{P}_0 & \widetilde{\mathbf{Q}} \\ \widetilde{\mathbf{Q}}^H & \mathbf{I}_{N_l N_F} \end{bmatrix} \succeq 0, \\ &\sum_{i=1}^{N-k} \mathbf{P}_0(i, i+k) = \delta_k, \widetilde{\mathbf{Q}} = [\mathcal{R}(\mathbf{Q}_1) \dots \mathcal{R}(\mathbf{Q}_{N_F})], \end{aligned} \tag{4.15}$$

where η depends on the noise level and is the same as in (4.12).

4.4 Regularization-free SDP and Fast Algorithm

In the previous section, we obtained an SDP that is equivalent to ANM. This SDP relies on the dual norm and dual polynomial (see Appendix 4.9.1 for the dual norm (4.39) and dual polynomial (4.40)), and so we deem the SDP in (4.13) as the *dual SDP*. We now derive the dual problem of the SDP in Sec. 4.3; we deem this as the *primal SDP*. The benefit of the primal SDP is that it is regularization-free and it thus avoids regularization bias in (4.15). In numerical experiments, this primal SDP is inherently robust to noise and near collisions. Further, we derive a fast, reduced-dimension version of the primal SDP. The fast program improves the speed, and more importantly, it relaxes the requirements that the sensor positions and temporal frequencies be uniform.

4.4.1 Non-uniform Array (NUA) and Non-uniform Frequency (NUF) Settings

In the previous sections, we focused on the ULA and uniform frequency case. However, in general, the array spacing and frequency may not be uniform. Thus we generalize the proposed framework to NUA and NUF cases.

Recall that $\mathcal{F} \subseteq \{1,\dots,N_F\}$ denotes the indices of the active source frequencies, with $N_f := |\mathcal{F}| \leq N_F$ denoting the number of active frequencies. The nonuniform frequency (NUF) case corresponds to the scenario where $N_f < N_F$, i.e., only some of the frequencies are active. Similarly, $\mathcal{M} \subseteq \{0,1,\dots,N_M-1\}$ denotes the indices of the sensors, with $N_m := |\mathcal{M}| \leq N_M$ denoting the number of sensors. The nonuniform array (NUA) case corresponds to the scenario where $N_m < N_M$, i.e., only some sensors are present.

Recall that every exponent in an array manifold vector from the MMV-MF model involves a product of one temporal frequency and one sensor position. To capture all such products in the nonuniform setting, we define a spatial-frequency index set $\mathcal{U}$ as follows:

$$\mathcal{U} = \{m \cdot f | m \in \mathcal{M}, f \in \mathcal{F}\}. \tag{4.16}$$

The cardinality of this set $N_u := |\mathcal{U}| \leq N$, with N is defined in (4.4). In many settings, $N_u \ll N$. In later sections, we see that the size of the fast SDP depends on N_u, and its complexity is greatly reduced compared to the original SDP.

4.4.2 Fast Dual SDP for the NUA and NUF Case

Proposition 4.3.1 gives the SDP for the ULA and uniform frequency case. We generalize the SDP to the NUA and NUF cases. The SDP is not only more general but also can reduce the complexity in the ULA and uniform frequency case. Inspired by the fast algorithm in [10, Sec. III-F], the SDP in this section is considered the fast algorithm for MMV.

For NUA and NUF, the measurement tensor $\mathcal{Y} \in \mathbb{C}^{N_m \times N_l \times N_f}$ and the SDP in Proposition 4.3.1 is generalized as

$$\begin{aligned} &\max_{Q, \mathbf{P}_{r0}} \langle Q, \mathcal{Y} \rangle_{\mathbb{R}} \quad \text{s.t.} \begin{bmatrix} \mathbf{P}_{r0} & \widetilde{\mathbf{Q}}_r \\ \widetilde{\mathbf{Q}}_r^H & \mathbf{I}_{N_l N_f} \end{bmatrix} \succeq 0, \\ &\sum_{\mathcal{U}_j - \mathcal{U}_i = k} \mathbf{P}_{r0}(i,j) = \delta_k, \widetilde{\mathbf{Q}}_r = [\mathcal{R}_{\mathfrak{l}}(\mathbf{Q}_1) \dots \mathcal{R}_{\mathfrak{l}}(\mathbf{Q}_{N_f})], \end{aligned} \tag{4.17}$$

where $Q = [\mathbf{Q}_1 | \dots | \mathbf{Q}_{N_f}] \in \mathbb{C}^{N_m \times N_l \times N_f}$ is the dual variable, $\mathbf{P}_{r0} \in \mathbb{C}^{N_u \times N_u}$, $\widetilde{\mathbf{Q}}_r = [\widetilde{\mathbf{Q}}_r^1 \dots \widetilde{\mathbf{Q}}_r^{N_f}] \in \mathbb{C}^{N_u \times N_l N_f}$ ($\widetilde{\mathbf{Q}}_r^f = \mathcal{R}_{\mathfrak{l}}(\mathbf{Q}_f) \in \mathbb{C}^{N_u \times N_l}$), and $\mathcal{R}_{\mathfrak{l}}(\mathbf{Q}_f) : N_m \times N_l \to N_u \times N_l$ is a mapping that pads zeros to the extra entries defined as

$$\mathcal{R}_{\mathfrak{l}}(\mathbf{Q}_f)(r,l) = \begin{cases} \mathbf{Q}_f(m,l) & \text{for } (\mathcal{U}_r, l) = (f \cdot (m-1), l) \\ 0 & \text{otherwise.} \end{cases} \tag{4.18}$$

Fig. 4.2 demonstrates the $\mathcal{R}_{\mathfrak{l}}(\cdot)$ mapping. We note that any rows of $\widetilde{\mathbf{Q}}_f$ which would have remained all-zero under the operator $\mathcal{R}(\cdot)$ (corresponding to unused space-frequency products) are simply omitted in $\mathcal{R}_{\mathfrak{l}}(\cdot)$.

Comparing (4.18) with (4.14), these two mappings pad zeros for the same input $\mathbf{Q}_f$ to obtain the output matrix with a different dimension. The $\mathcal{R}$ mapping defined in (4.14) maps a matrix with N_M rows into one with N rows, while $\mathcal{R}_{\mathfrak{l}}$ defined in (4.18) omits the unused products of temporal frequency and sensor position, mapping a matrix with N_m rows into one with only N_u rows. This not only gives a lower-dimensional formulation (the size of $\mathbf{P}_{r0}$ decreases from $N \times N$ to $N_u \times N_u$), but it naturally accommodates the NUA and NUF settings. Still, (4.17) can be applied to the ULA and uniform frequency case, where N_u will often be somewhat smaller than N.

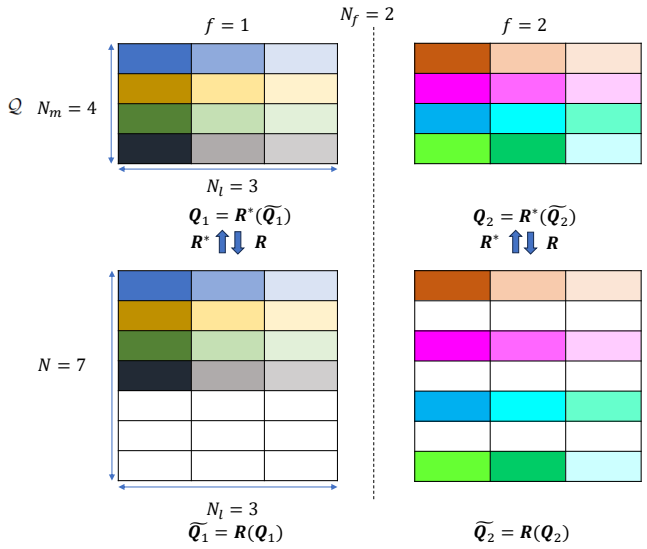

Figure 4.1: Demonstration for the $\mathcal{R}(\cdot)$ mapping and its adjoint mapping $\mathcal{R}^*(\cdot)$. $N_m = N_M = 4$, $N_l = 3$, $N_f = N_F = 2$, $N = (N_M - 1)N_F + 1 = 7$.

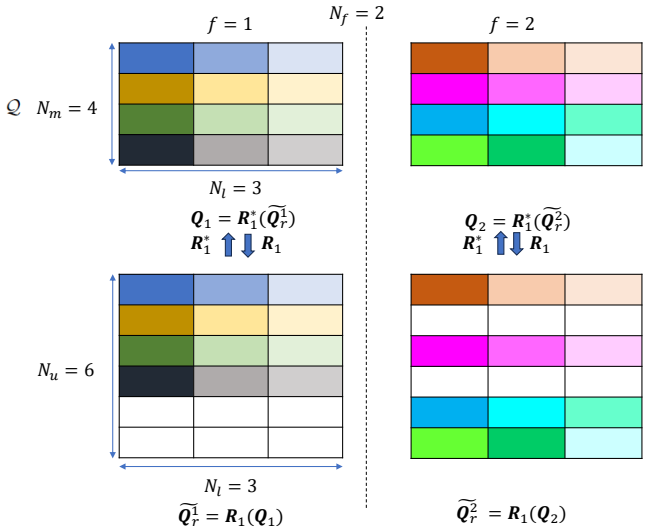

Figure 4.2: Demonstration for the $\mathcal{R}_\mathcal{U}(\cdot)$ mapping and its adjoint mapping $\mathcal{R}_\mathcal{U}^*(\cdot)$. $N_m = N_M = 4$, $N_l = 3$, $N_f = N_F = 2$, $\mathcal{U} = \{0,1,2,3,4,6\}$, $N_u = |\mathcal{U}| = 6$.

4.4.3 Fast Primal SDP for the NUA and NUF Case

In this section, we derive the dual problem of (4.17), yielding a fast primal SDP that is regularization-free and naturally accommodates the NUA and NUF settings.

Proposition 4.4.1 *The dual problem of* (4.17) *is given by*

$$\begin{aligned} &\min_{\mathbf{W},\mathbf{u},\widetilde{\mathbf{Y}}} [\mathrm{Tr}(\mathrm{T}(\mathbf{u})) + \mathrm{Tr}(\mathbf{W})] \\ &s.t. \begin{bmatrix} \mathrm{T}(\mathbf{u}) & \widetilde{\mathbf{Y}} \\ \widetilde{\mathbf{Y}}^H & \mathbf{W} \end{bmatrix} \succeq 0, \mathbf{Y}_f = \mathcal{R}_{\mathfrak{l}}^*(\widetilde{\mathbf{Y}}_f), f \in \mathcal{F}, \end{aligned} \tag{4.19}$$

where $\widetilde{\mathbf{Y}} \in \mathbb{C}^{N_u \times N_l N_f}$, $\mathbf{W} \in \mathbb{C}^{N_l N_f \times N_l N_f}$, $\mathbf{Y}_f \in \mathbb{C}^{N_m \times N_l}$ *is the slice of the received signal tensor* $\mathcal{Y}$ *corresponding to frequency* f*, and* $\widetilde{\mathbf{Y}}_f \in \mathbb{C}^{N_u \times N_l}$ *comes from taking the* N_l *columns of* $\widetilde{\mathbf{Y}}$ *corresponding to frequency* f*.* $\mathcal{R}_{\mathfrak{l}}^*(\cdot) : N_u \times N_l \to N_m \times N_l$ *is the adjoint mapping of* $\mathcal{R}_{\mathfrak{l}}$*.*

Proof Consider the Lagrangian given by

$$\begin{aligned} &\mathcal{L}(\mathcal{Q}, \mathbf{P}_{r0}, \mathbf{U}_r, \mathbf{\Lambda}_1, \mathbf{\Lambda}_2, \mathbf{\Lambda}_3, \mathbf{\Lambda}_Q, \mathbf{v}) = \\ &\langle \mathcal{Q}, \mathcal{Y} \rangle_{\mathbb{R}} - \left\langle \begin{bmatrix} \mathbf{\Lambda}_1 & \mathbf{\Lambda}_2 \\ \mathbf{\Lambda}_2^H & \mathbf{\Lambda}_3 \end{bmatrix}, \begin{bmatrix} \mathbf{P}_{r0} & \mathbf{U}_r \\ \mathbf{U}_r^H & \mathbf{I}_{N_l N_f} \end{bmatrix} \right\rangle_{\mathbb{R}} \\ &- \sum_{k=0}^{N-1} v_k (\delta_k - \sum_{\mathcal{U}_j - \mathcal{U}_i = k} \mathbf{P}_{r0}(i,j)) - \sum_{f \in \mathcal{F}} \langle \mathbf{\Lambda}_Q^f, \mathbf{U}_r^f - \mathcal{R}_{\mathfrak{l}}(\mathbf{Q}^f) \rangle_{\mathbb{R}} \\ &= \sum_{f \in \mathcal{F}} [\langle \mathbf{Q}_f, \mathbf{Y}_f \rangle_{\mathbb{R}} + \langle \mathbf{\Lambda}_Q^f, \mathcal{R}_{\mathfrak{l}}(\mathbf{Q}_f) \rangle_{\mathbb{R}}] - [\langle \mathbf{P}_{r0}, \mathbf{\Lambda}_1 \rangle_{\mathbb{R}} \\ &+ 2\langle \mathbf{\Lambda}_2, \mathbf{U}_r \rangle_{\mathbb{R}} + \mathrm{Tr}(\mathbf{\Lambda}_3)] - \mathbf{v}_0 + \langle \mathbf{P}_{r0}, \mathrm{T}(\mathbf{v}) \rangle_{\mathbb{R}} - \sum_{f \in \mathcal{F}} \langle \mathbf{\Lambda}_Q^f, \mathbf{U}_r^f \rangle_{\mathbb{R}}. \end{aligned} \tag{4.20}$$

Note that we use the following fact during the derivation: $\sum_{k=0}^{N-1} v_k \sum_{\mathcal{U}_j - \mathcal{U}_i = k} \mathbf{P}_{r0}(i,j) = \langle \mathbf{P}_{r0}, \mathrm{T}(\mathbf{v}) \rangle_{\mathbb{R}}$, where $\mathrm{T} : N \times 1 \to N_u \times N_u$ is explicitly defined as (note * denotes complex conjugate)

$$\mathrm{T}(\mathbf{v})(i,j) := \begin{cases} v_{\mathcal{U}_j - \mathcal{U}_i} & \mathcal{U}_j - \mathcal{U}_i \geq 0 \\ v^*_{\mathcal{U}_i - \mathcal{U}_j} & \mathcal{U}_j - \mathcal{U}_i < 0. \end{cases} \tag{4.21}$$

We provide an example of this mapping in Sec. 4.4.5.

The dual matrix $\begin{bmatrix} \mathbf{\Lambda}_1 & \mathbf{\Lambda}_2 \\ \mathbf{\Lambda}_2^H & \mathbf{\Lambda}_3 \end{bmatrix}$ associated with the inequality constraint $\begin{bmatrix} \mathbf{P}_{r0} & \mathbf{U}_r \\ \mathbf{U}_r^H & \mathbf{I}_{N_f} \end{bmatrix} \succeq 0$ needs to be a PSD matrix to ensure that the inner product between these two matrices is non-negative so that the optimal value for the dual problem gives a lower bound for the primal problem.

The dual function is

$$\begin{aligned} g(\mathbf{\Lambda}_1,\mathbf{\Lambda}_2,\mathbf{\Lambda}_3,\mathbf{\Lambda}_Q,\mathbf{v}) = \inf_{Q,\mathbf{P}_{r0},\mathbf{U}_r} & \mathcal{L}(Q,\mathbf{P}_{r0},\mathbf{U}_r,\mathbf{\Lambda}_1,\mathbf{\Lambda}_2,\mathbf{\Lambda}_3,\mathbf{\Lambda}_Q,\mathbf{v}) \\ \text{s.t.} & \begin{bmatrix} \mathbf{\Lambda}_1 & \mathbf{\Lambda}_2 \\ \mathbf{\Lambda}_2^H & \mathbf{\Lambda}_3 \end{bmatrix} \succeq 0. \end{aligned} \tag{4.22}$$

The infimum of $\mathcal{L}$ in (4.20) over Q is thereby $\inf_Q J(Q) := \sum_{f\in\mathcal{F}}[\langle \mathbf{Q}_f, \mathbf{Y}_f\rangle_{\mathbb{R}} + \langle \mathbf{\Lambda}_Q^f, \mathcal{R}_1^*(\mathbf{Q}_f)\rangle_{\mathbb{R}}] = \sum_{f\in\mathcal{F}}[\langle \mathbf{Q}_f, \mathbf{Y}_f\rangle_{\mathbb{R}} + \langle \mathbf{Q}_f, \mathcal{R}_1^*(\mathbf{\Lambda}_Q^f)\rangle_{\mathbb{R}}] = \sum_{f\in\mathcal{F}}\langle \mathbf{Q}_f, \mathbf{Y}_f + \mathcal{R}_1^*(\mathbf{\Lambda}_Q^f)\rangle_{\mathbb{R}}$. The infimum of $J(\mathbf{Q})$ is bounded only if $\mathbf{Y}_f = -\mathcal{R}_1^*(\mathbf{\Lambda}_Q^f)$ for any $f \in \mathcal{F}$. Similarly, the infimum of $\mathcal{L}$ over $\mathbf{P}_{r0}$ is bounded only if $\mathrm{T}(\mathbf{v}) = \mathbf{\Lambda}_1 \succeq 0$. The infimum of $\mathcal{L}$ over $\mathbf{U}_r$ is bounded only if $\mathbf{\Lambda}_Q^f = -2\mathbf{\Lambda}_2^f$. Considering $2\mathbf{\Lambda}_2^f = \widetilde{\mathbf{Y}}_f$, then we must have $\mathbf{Y}_f = -\mathcal{R}_1^*(\mathbf{\Lambda}_Q^f) = \mathcal{R}_1^*(2\mathbf{\Lambda}_2^f) = \mathcal{R}_1^*(\widetilde{\mathbf{Y}}_f)$.

Considering $\mathbf{\Lambda}_3 = \frac{1}{2}\mathbf{W}$ and $\mathbf{v} = \frac{1}{2}\mathbf{u}$, the dual function becomes $-\frac{1}{2}\mathrm{Tr}(\mathbf{W}) - \frac{1}{2}\mathrm{Tr}(\mathrm{T}(\mathbf{u}))$.

Therefore, the fast program in the primal domain is given by (4.19). □

SMV Setup

The fast program (4.19) can not only improve the execution time in the uniform cases, but it naturally accommodates the NUA and NUF cases as well. (4.19) can also be adapted to the SMV setup (i.e. $N_l = 1$). In that case, the received signal $\mathbf{Y}$ will reduce to an $N_m \times N_f$ matrix and

(4.19) will reduce to

$$\begin{aligned} &\min_{\mathbf{W},\mathbf{u},\widetilde{\mathbf{Y}}} [\mathrm{Tr}(\mathrm{T}(\mathbf{u})) + \mathrm{Tr}(\mathbf{W})] \\ &\text{s.t.} \begin{bmatrix} \mathrm{T}(\mathbf{u}) & \widetilde{\mathbf{Y}} \\ \widetilde{\mathbf{Y}}^H & \mathbf{W} \end{bmatrix} \succeq 0, \mathbf{Y}_f = \mathcal{R}_l^*(\widetilde{\mathbf{Y}}_f), f \in \mathcal{F}, \end{aligned} \tag{4.23}$$

where $\widetilde{\mathbf{Y}} \in \mathbb{C}^{N_u \times N_f}$, $\mathbf{W} \in \mathbb{C}^{N_f \times N_f}$, $\mathbf{Y}_f \in \mathbb{C}^{N_m \times 1}$ is the column of the received signal $\mathbf{Y}$ corresponding to frequency f, and $\widetilde{\mathbf{Y}}_f \in \mathbb{C}^{N_u \times 1}$ comes from taking the column of $\widetilde{\mathbf{Y}}$ corresponding to frequency f.

Comparison to full-dimension primal SDP

Recall that (4.13) is the dual SDP for the ULA and uniform frequency setting. A significant difference between (4.13) and (4.17) lies in the dimensions of the matrices in the PSD constraint and the equality constraint. Following the same procedure in this section, the dual SDP of (4.13) can be obtained, yielding the following full-dimension primal SDP for the ULA and uniform frequency case:

$$\begin{aligned} &\min_{\mathbf{W},\mathbf{u},\widetilde{\mathbf{Y}}_N} [\mathrm{Tr}(\mathrm{Toep}(\mathbf{u})) + \mathrm{Tr}(\mathbf{W})] \\ &\text{s.t.} \begin{bmatrix} \mathrm{Toep}(\mathbf{u}) & \widetilde{\mathbf{Y}}_N \\ \widetilde{\mathbf{Y}}_N^H & \mathbf{W} \end{bmatrix} \succeq 0, \mathbf{Y}_f = \mathcal{R}^*(\widetilde{\mathbf{Y}}_{Nf}), f = 1, \ldots, N_F, \end{aligned} \tag{4.24}$$

where $\mathrm{Toep}(\cdot) : N \times 1 \to N \times N$ is the Toeplitz operator that maps a vector to a self-adjoint Toeplitz matrix. $\widetilde{\mathbf{Y}}_N \in \mathbb{C}^{N \times N_l N_F}$, $\mathcal{R}^*(\cdot) : N \times N_l \to N_M \times N_l$ is the adjoint mapping of $\mathcal{R}(\cdot)$, and $\widetilde{\mathbf{Y}}_{Nf} \in \mathbb{C}^{N \times N_l}$ is taking N_l columns from $\widetilde{\mathbf{Y}}_N$ (from the $(f-1) \cdot N_l + 1$-th to the $f \cdot N_l$-th column). Compared to (4.19), a main difference is that $\mathrm{T}(\mathbf{u}) \in \mathbb{C}^{N_u \times N_u}$ in (4.19) is changed to $\mathrm{Toep}(\mathbf{u}) \in \mathbb{C}^{N \times N}$.

4.4.4 Existence of Irregular Vandermonde Decomposition (IVD)

The full-dimension primal SDP in (4.24) has an interesting connection to the SDPs from the ANM literature which involve trace minimization of a (regular) Toeplitz matrix [22, 24]. In ANM problems that involve trace minimization of a regular Toeplitz matrix, one typically computes the Vandermonde decomposition of the resulting Toeplitz matrix in order to extract the frequencies/DOAs. Indeed, as we discuss further in Section 4.6, trace minimization serves as a convex relaxation of rank minimization, and a formal connection can be established between rank minimization and finding the sparsest decomposition in the atomic set $\mathcal{A}$.

In contrast, the fast primal SDPs (4.19) and (4.23) derived in the previous section involve trace minimization not of a Toeplitz matrix but rather a matrix of the form $\mathrm{T}(\mathbf{u})$. (See Sec. 4.4.5 for an illustration of the structure of $\mathrm{T}(\mathbf{u})$.) However, as we establish in Theorem 4.4.2 below, there is an important connection between $\mathrm{T}(\mathbf{u})$ and Toeplitz matrices: $\mathrm{T}(\mathbf{u})$ is guaranteed to be an irregular Toeplitz matrix, and therefore is guaranteed to have an IVD. This inspires our proposed method for extracting DOA information from $\mathrm{T}(\mathbf{u})$, which we outline in Section 4.4.6.

Theorem 4.4.2 *For any* $\mathbf{u}$ *such that* $\mathrm{Toep}(\mathbf{u})$ *is PSD,* $\mathrm{T}(\mathbf{u}) \in \mathbb{C}^{N_u \times N_u}$ *is an* (N_u, K)*-irregular Toeplitz matrix, where* $K = \mathrm{rank}(\mathrm{Toep}(\mathbf{u}))$. *Specifically,* $\mathrm{T}(\mathbf{u})$ *has an IVD of the form* (4.9)*, where* $\boldsymbol{\gamma} = [\mathcal{U}_1, \ldots \mathcal{U}_{N_u}]^T$.

Proof First, let $P_{\mathcal{U}} : \mathbb{C}^N \to \mathbb{C}^{N_u}$ denote a linear restriction operator that selects only the entries in a vector corresponding to the positions indexed by $\mathcal{U}$.

Now, consider $\mathrm{Toep}(\mathbf{u}) \in \mathbb{C}^{N \times N}$, and observe that $\mathrm{T}(\mathbf{u}) \in \mathbb{C}^{N_u \times N_u}$ can be obtained by a mapping from $\mathrm{Toep}(\mathbf{u})$ as follows: $\mathrm{T}(\mathbf{u}) := P_{\mathcal{U}} \mathrm{Toep}(\mathbf{u}) P_{\mathcal{U}}^H$. Since $\mathrm{Toep}(\mathbf{u})$ is PSD, it is guaranteed to have a Vandermonde decomposition of the form [42, Theorem 11.5]:

$$\mathrm{Toep}(\mathbf{u}) = \mathbf{V}(\mathbf{z}) \mathbf{D} \mathbf{V}(\mathbf{z})^H \tag{4.25}$$

where $\mathbf{V}(\mathbf{z}) \in \mathbb{C}^{N \times K}$ is a Vandermonde matrix parameterized by $\mathbf{z}$ with $|\mathbf{z}| = 1$, and $\mathbf{D} \in \mathbb{R}^{K \times K}$ is

a diagonal matrix with positive diagonals. Hence,

$$\begin{aligned}
\mathrm{T}(\mathbf{u}) &= P_{\mathcal{U}}\mathrm{Toep}(\mathbf{u})P_{\mathcal{U}}^H = P_{\mathcal{U}}\mathbf{V}(\mathbf{z})\mathbf{D}\mathbf{V}(\mathbf{z})^H P_{\mathcal{U}}^H \\
&= (P_{\mathcal{U}}\mathbf{V}(\mathbf{z}))\mathbf{D}(\mathbf{V}(\mathbf{z})^H P_{\mathcal{U}}^H) \\
&= \mathbf{W}(\boldsymbol{\gamma},\mathbf{z})\mathbf{D}\mathbf{W}(\boldsymbol{\gamma},\mathbf{z})^H,
\end{aligned} \tag{4.26}$$

where $\mathbf{W}(\boldsymbol{\gamma},\mathbf{z}) := P_{\mathcal{U}}\mathbf{V}(\mathbf{z})$ will be an irregular Vandermonde matrix of the form (4.8) with $\boldsymbol{\gamma} = [\mathcal{U}_1 \dots \mathcal{U}_{N_u}]^T$. Therefore, $\mathrm{T}(\mathbf{u})$ is an (N_u, K)-irregular Toeplitz matrix. □

4.4.5 An Example for $\mathrm{T}(\mathbf{v})$

We demonstrate the structure of $\mathrm{T}(\mathbf{v})$ in the following example. Consider $\mathcal{M} = \{0,1,3,4\}$ and $\mathcal{F} = \{1,3,4\}$. Therefore, $N_m = |\mathcal{M}| = 4$, $N_f = |\mathcal{F}| = 3$, $\mathcal{U} = \{0,1,3,4,9,12,16\}$, $N_M = 5$, $N_F = 4$, $N = (N_M - 1)N_F + 1 = 17$, and $N_u = |\mathcal{U}| = 7$. For $\mathbf{v} = [v_0 \dots v_{16}]^T$, $\mathrm{T}(\mathbf{v}) \in \mathbb{C}^{N_u \times N_u}$ can be expressed as

$$\mathrm{T}(\mathbf{v}) = \begin{bmatrix}
v_0 & v_1 & v_3 & v_4 & v_9 & v_{12} & v_{16} \\
v_1^* & v_0 & v_2 & v_3 & v_8 & v_{11} & v_{15} \\
v_3^* & v_2^* & v_0 & v_1 & v_6 & v_9 & v_{13} \\
v_4^* & v_3^* & v_1^* & v_0 & v_5 & v_8 & v_{12} \\
v_9^* & v_8^* & v_6^* & v_5^* & v_0 & v_3 & v_7 \\
v_{12}^* & v_{11}^* & v_9^* & v_8^* & v_3^* & v_0 & v_4 \\
v_{16}^* & v_{15}^* & v_{13}^* & v_{12}^* & v_7^* & v_4^* & v_0
\end{bmatrix}.$$

Note v_{10} and v_{14} do not appear in $\mathrm{T}(\mathbf{v})$. In Theorem 4.4.2, we show that for any $\mathbf{v}$ such that such that $\mathrm{Toep}(\mathbf{v})$ is PSD, $\mathrm{T}(\mathbf{v})$ is guaranteed to be an irregular Toeplitz matrix. In this case, $\mathrm{T}(\mathbf{v})$ is guaranteed to have an IVD: $\mathrm{T}(\mathbf{v}) = \mathbf{W}(\boldsymbol{\gamma},\mathbf{z})\mathbf{D}\mathbf{W}(\boldsymbol{\gamma},\mathbf{z})^H$, where $\mathbf{D} = \mathrm{diag}(d_1,\dots,d_K)$ with $K = \mathrm{rank}(\mathrm{Toep}(\mathbf{v}))$, and where $\boldsymbol{\gamma} = [0\ 1\ 3\ 4\ 9\ 12\ 16]^T$.

4.4.6 DOA Extraction

After solving the fast primal SDP (4.19) by an off-the-shelf SDP solver (e.g., CVX [38]) and obtaining $\mathbf{u}$, we propose to extract the DOAs by exploiting the IVD of the irregular Toeplitz $\mathrm{T}(\mathbf{u}) = \mathbf{W}(\boldsymbol{\gamma},\mathbf{z})\mathbf{D}\mathbf{W}(\boldsymbol{\gamma},\mathbf{z})^H$. Although this factorization is not computed explicitly as part of solving the SDP, its existence provides a means to estimate the entries of $\mathbf{z}$, each corresponding to a point on the unit circle whose complex angle encodes a DOA.

Let $\mathbf{T}(\mathbf{u})$ denote an (N_u, K)-irregular Toeplitz matrix that has an IVD of the form $\mathrm{T}(\mathbf{u}) = \mathbf{W}(\boldsymbol{\gamma},\mathbf{z})\mathbf{D}\mathbf{W}(\boldsymbol{\gamma},\mathbf{z})^H$, where $\boldsymbol{\gamma} = [\mathcal{U}_1 \dots \mathcal{U}_{N_u}]^T$. Consider the eigen-decomposition of $\mathbf{T}(\mathbf{u})$:

$$\mathbf{T}(\mathbf{u}) = \mathbf{U}_S\boldsymbol{\Lambda}_S\mathbf{U}_S^H + \mathbf{U}_N\boldsymbol{\Lambda}_N\mathbf{U}_N^H, \tag{4.27}$$

where $\boldsymbol{\Lambda}_S \in \mathbb{C}^{K\times K}$ is a diagonal matrix containing the K largest eigenvalues of $\mathbf{T}(\mathbf{u})$, $\mathbf{U}_S \in \mathbb{C}^{N_u\times K}$ contains the corresponding eigenvectors, and $\boldsymbol{\Lambda}_N \in \mathbb{C}^{(N_u-K)\times(N_u-K)}$ and $\mathbf{U}_N \in \mathbb{C}^{N_u\times(N_u-K)}$ contain the remaining (zero) eigenvalues and corresponding eigenvectors. $\mathbf{U}_S$ and $\mathbf{U}_N$ are known as the *signal and noise subspaces*, respectively.

For $z \in \mathbb{C}$, define the irregular null spectrum $\tilde{D}(z)$ of $\mathbf{T}(\mathbf{u})$ as [26, eq. (29)]

$$\tilde{D}(z) = \mathbf{w}(\boldsymbol{\gamma},z)^H\mathbf{U}_N\mathbf{U}_N^H\mathbf{w}(\boldsymbol{\gamma},z) = \mathbf{w}(\boldsymbol{\gamma},z)^H\mathbf{G}\mathbf{w}(\boldsymbol{\gamma},z), \tag{4.28}$$

where $\mathbf{G} = \mathbf{U}_N\mathbf{U}_N^H$. The behavior of the irregular null spectrum is plotted in Fig. 4.3.

Since $\mathbf{G} \perp \mathbf{W}(\boldsymbol{\gamma},\mathbf{z})$ and $|\mathbf{z}| = 1$, the DOAs encoded in $\mathbf{z}$ are associated to the K roots of $\tilde{D}(z)$ on the unit circle. [26] suggests that the local minima of $\tilde{D}(z)$ evaluated on the unit circle give DOA estimates with similar accuracy as those given by the actual roots. Therefore, $\mathbf{z}$ is estimated as [26, eq. (43)]

$$\hat{\mathbf{z}} = \arg\min_{|z|=1}^{k} \tilde{D}(z), \quad k = 1,\dots,K \tag{4.29}$$

where $\arg\min_z^k$ denotes the argument, z, which produces the kth smallest local minima. The

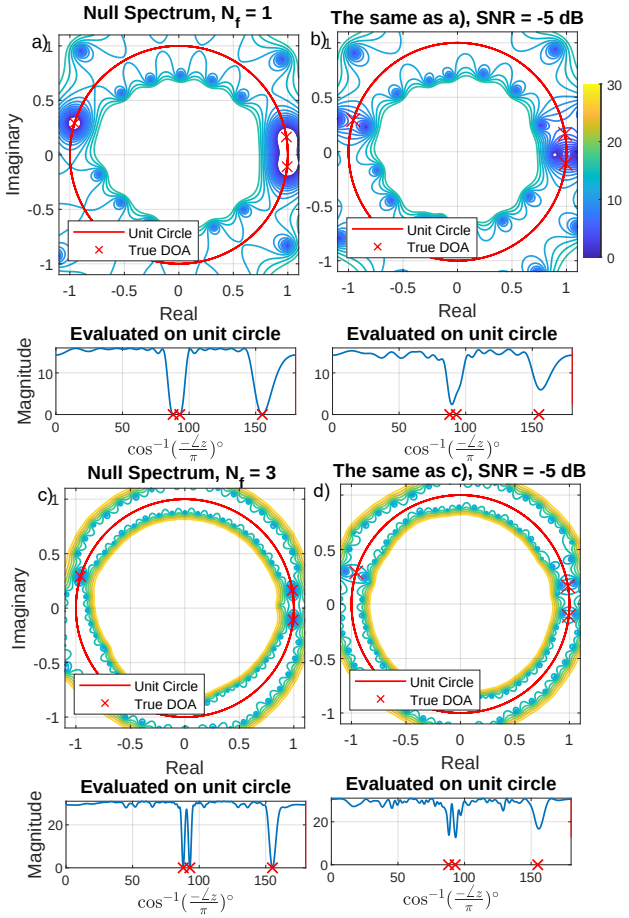

Figure 4.3: Null spectrum contours (dB) using $N_M = 16$, $K = 3$, $N_l = 5$. For a) - b) $N_F = 1$, and for c) - d) $N_F = 3$. The frequency set is $\{1,\ldots,N_F\}\cdot 100$ Hz and ULA is applied. DOAs are $[88,93,155]^\circ$, marked by red x's. a) and c): Null spectrum from noise-free measurement. b) and d): SNR = -5 dB.

DOAs $\hat{\theta}, \hat{w}$, and $\hat{z}$ are estimated by

$$\hat{\theta} = \cos^{-1}\left(-\frac{\angle\hat{z}}{\pi}\right), \quad \hat{w} = \frac{-\angle\hat{z}}{2\pi}, \quad \hat{z} = e^{-j\pi\cos(\hat{\theta})}. \tag{4.30}$$

In summary, we first solve the SDP (4.19) via an off-the-shelf SDP solver (e.g., CVX [38]). After $\mathbf{u}$ is obtained, the DOAs can be retrieved by computing the irregular null spectrum $\tilde{D}(z)$ of $\mathrm{T}(\mathbf{u})$ and following the steps mentioned in this section. The implementation details of the

proposed method are summarized in Algorithm 2.

Algorithm 2: Regularization-free DOA estimation

Input: $\mathcal{Y} \in \mathbb{C}^{N_m \times N_l \times N_f}$, K

Initialization:

Solve (4.19) by CVX and obtain $\mathbf{u}$

Obtain $\mathrm{T}(\mathbf{u})$ based on (4.21)

$[\mathbf{U}, \mathbf{\Lambda}] = \mathrm{eig}(\mathrm{T}(\mathbf{u}))$

$\mathbf{U}_N = \mathbf{U}(:, K+1 : N_u)$

$\mathbf{G} = \mathbf{U}_N \mathbf{U}_N^H$

Obtain $\tilde{D}(z)$ based on (4.28)

$\hat{\mathbf{z}} = \mathrm{find}(\arg\min(\tilde{D}(z)), |\mathbf{z}| = 1)$

$\hat{\theta} \leftarrow 180 - \mathrm{acosd}(\mathrm{angle}(\hat{\mathbf{z}}/\pi))$

Output: $\hat{\theta}$

4.5 More Sources Than Sensors in the ULA Setup

Many prior works have demonstrated the possibility of resolving more sources than the number of array sensors based on special array geometries such as MRA [30, 43], co-prime arrays [32], and nested array [33]. However, for single-frequency ULA, the maximum number of resolvable sources is $N_M - 1$ [42, Sec 11.2.3]. In this section, we will demonstrate the possibility of resolving more sources than sensors *under the ULA setup* if multiple frequencies are available. We primarily solve (4.24) and follow the procedures in Algorithm 1 to retrieve the DOAs. In our multi-frequency ANM configuration, it can resolve up to $N - 1 = (N_M - 1)N_F$ sources as $\mathrm{Toep}(\mathbf{u}) \in \mathbb{C}^{N \times N}$ and $\mathbf{U}_N$ exists only if $K \leq N - 1$. The reason for using (4.24) instead of (4.19) is that (4.19) can resolve up to $N_u - 1$ sources and (4.24) has the potential to resolve more sources than (4.19) because $\mathrm{Toep}(\mathbf{u})$ in (4.24) has a higher dimension than $\mathrm{T}(\mathbf{u})$ in (4.19).

The key observation for the multi-frequency model is that these frequencies increase the diversity of the harmonics. These extra harmonics serve as "virtual" sensors in the array, and they bring about an enhanced degree of freedom. For example, consider a ULA with $N_M = 4$ sensors

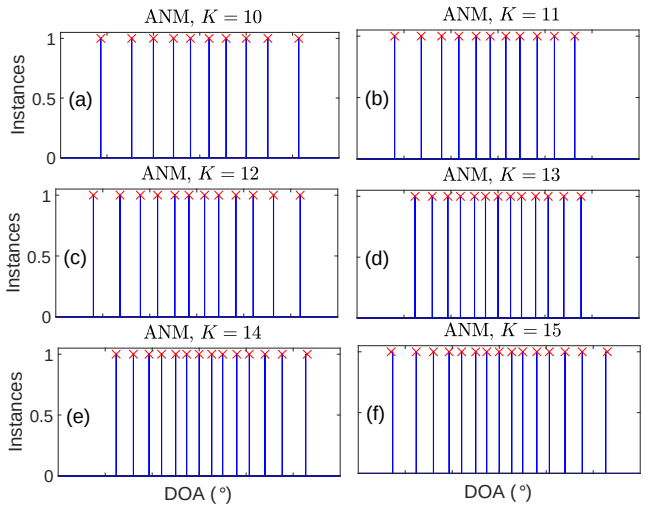

Figure 4.4: Estimated and True DOAs for ANM ("$\times$" indicates the true DOAs and the blue vertical line indicates the estimated DOAs). $N_M = 4$, $N_F = 5$, $N_l = 1$, and $K = 10, 11, 12, 13, 14, 15$. The RMSEs of ANM under $K = 10, 11, 12, 13, 14, 15$ are 0.005°, 0.16°, 0.20°, 0.04°, 0.27°, and 0.27°.

and $N_F = 5$ uniform frequencies. Therefore, it can resolve up to $(N_M - 1)N_F = 15$ sources. The SDP problem (4.19) can be interpreted as a structured covariance matrix estimation problem (T($\mathbf{u}$) can be interpreted as the covariance matrix). We notice this covariance matrix is in a higher dimension, which corresponds to our intuition that there are more sensors in our "virtual" array.

As an example, suppose we have $N_M = 4$ sensors, $N_F = 5$ frequencies ($\{100, \ldots, 500\}$ Hz), $N_l = 1$ noise-free snapshot, and $K = 10, 11, 12, 13, 14, 15$ sources with uniform and deterministic across frequencies. For $K = 10, 12$, and 15, the DOAs are generated as the uniform distribution in the cosine domain (i.e., the DOAs are $\lfloor \cos^{-1}(-1 + 2([1:K] - 0.5)/K) \rfloor$). For $K = 11$, we pick up the last 11 sources in the $K = 12$ case. For $K = 13$, we pick up the middle 13 sources in the $K = 15$ case, and for $K = 14$, we pick up the middle 14 sources. We plot the estimated DOAs for ANM. From Fig. 4.4, we can see our ANM can resolve up to $(N_M - 1)N_F = 15$ sources.

4.6 Rank Minimization and Atomic ℓ_0 Norm Minimization

In this section, we highlight the connection between rank minimization and atomic ℓ_0 norm minimization. More specifically, atomic ℓ_0 norm minimization can be interpreted as a covariance matrix estimation approach where low-rankness and Toeplitz structure are explicitly enforced [22, 24]. However, atomic ℓ_0 norm minimization is non-convex and may not be computationally feasible. By considering ANM, the convex relaxation of the atomic ℓ_0 norm, we obtain (4.19) and (4.23) as trace minimization problems that are computationally feasible and in which the low-rankness and Toeplitz structure are implicitly enforced. In this way, we can understand the benefits of ANM compared to conventional covariance matrix estimation using the sample covariance matrix. Before describing the equivalence, we review the definitions of the covariance matrix and the sample covariance matrix.

We assume $N_l = 1$, noise-free measurement, uniform frequency and ULA setup, and full dimensional SDP in this section, and our discussion serves as a means to interpret (4.23).

4.6.1 Covariance Matrix Estimation

Suppose $\widetilde{\mathbf{Y}} \in \mathbb{C}^{N \times N_F}$ is noise-free and defined as

$$\widetilde{\mathbf{Y}} = \sum_{k=1}^{K} \mathbf{z}_k \mathbf{x}_k^H = [\mathbf{z}_1 \dots \mathbf{z}_K][\mathbf{x}_1 \dots \mathbf{x}_K]^H = \mathbf{Z}\mathbf{X} \tag{4.31}$$

where $\mathbf{z}_k := [z_k^0 \dots z_k^{N-1}]^T \in \mathbb{C}^N$, $\mathbf{x}_k = [x_k^{(1)} \dots x_k^{(N_F)}]^T \in \mathbb{C}^{N_F}$, $\mathbf{Z} := [\mathbf{z}_1 \dots \mathbf{z}_K] \in \mathbb{C}^{N \times K}$, and $\mathbf{X} := [\mathbf{x}_1 \dots \mathbf{x}_K]^H \in \mathbb{C}^{K \times N_F}$. Note that $\mathbf{Z}$ is a Vandermonde matrix and that $\widetilde{\mathbf{Y}}$ satisfies

$$\mathbf{Y} = \mathcal{R}^*(\widetilde{\mathbf{Y}}). \tag{4.32}$$

The sample covariance matrix $\hat{\mathbf{R}}_{\tilde{y}\tilde{y}}$ and covariance matrix $\mathbf{R}_{\tilde{y}\tilde{y}}$ are defined as

$$\hat{\mathbf{R}}_{\tilde{y}\tilde{y}} = \frac{1}{N_f}\widetilde{\mathbf{Y}}\widetilde{\mathbf{Y}}^H, \tag{4.33}$$

$$\mathbf{R}_{\tilde{y}\tilde{y}} = \mathbb{E}[\hat{\mathbf{R}}_{\tilde{y}\tilde{y}}] = \mathbf{Z}\mathbf{\Lambda}_X\mathbf{Z}^H \tag{4.34}$$

where $\mathbf{\Lambda}_X := \frac{1}{N_f}\mathbb{E}[\mathbf{X}\mathbf{X}^H]$ is a diagonal matrix due to uncorrelated sources. Note that $\mathbf{R}_{\tilde{y}\tilde{y}}$ is a Toeplitz Hermitian matrix in the noise-free case, $\mathbf{Z}\mathbf{\Lambda}_X\mathbf{Z}^H$ is its Vandermonde decomposition, and the DOAs are encoded in the Vandermonde matrix $\mathbf{Z}$. The essence of some classical DOA estimation approaches (e.g. MUSIC, and ESPRIT) lies in Vandermonde decomposition of the estimated covariance matrix. However, $\widetilde{\mathbf{Y}}$ is not fully observed in our problem as only $\mathbf{Y}$, the image of the $\mathcal{R}^*$ mapping is accessible. To further obtain $\tilde{\mathbf{Y}}$, the $\mathcal{R}$ mapping needs to be applied. Note if we apply $\mathcal{R}^*$ first and then $\mathcal{R}$ on a matrix, we may not obtain the same matrix as the white entries in Fig. 4.1 cannot be recovered after the $\mathcal{R}^*$ mapping. Therefore, the covariance matrix of $\tilde{\mathbf{Y}}$ must be estimated by solving a convex optimization problem.

4.6.2 Connection Between Rank Minimization and Atomic ℓ_0 Norm Minimization

As described in Sec. 4.4.6, after solving the SDP (4.23) and obtaining $\mathbf{u}$, DOAs are extracted by computing the IVD of $\mathrm{T}(\mathbf{u})$. In light of the discussion in Section 4.6.1, then, (4.23) can be interpreted as a covariance matrix estimation problem where $\mathrm{T}(\mathbf{u})$ serves as an estimate for a covariance matrix that contains the DOA information. In this section, we discuss this connection more deeply.

From (4.34), the true covariance matrix in the noise-free case $\mathbf{R}_{\tilde{y}\tilde{y}}$ has three important properties: (1) Toeplitz and Hermitian; (2) PSD; (3) low-rank (its rank is K (number of sources) and is usually much smaller than its size N_u). A commonly used estimate for the covariance matrix

is the *sample covariance matrix* $\hat{\mathbf{R}}_{\tilde{y}\tilde{y}}$ defined in (4.33), which is PSD. However, this estimate does not promote the Toeplitz structure of the covariance matrix. This limitation is overcome by the SDP formulation in (4.23). The irregular Toeplitz structure is obviously enforced in $\mathrm{T}(\mathbf{u})$. Meanwhile, (4.23) also promotes low-rank structure, a fact that warrants more discussion.

The atomic ℓ_0 norm of an $N \times N_F$ matrix $\widetilde{\mathbf{Y}}$ is defined as

$$\|\widetilde{\mathbf{Y}}\|_{\mathcal{A},0} := \inf\left\{ K \middle| \widetilde{\mathbf{Y}} = \sum_{k=1}^{K} c_k \mathbf{z}_k \mathbf{x}_k^H, c_k > 0 \right\} \tag{4.35}$$

where $\mathbf{z}_k := [z_k^0 \dots z_k^{N-1}]^T \in \mathbb{C}^N$ such that $|z_k| = 1$ and $\mathbf{x}_k = [x_k^{(1)} \dots x_k^{(N_F)}]^T \in \mathbb{C}^{N_F}$ such that $\|\mathbf{x}_k\|_2 = 1$.

The following proposition establishes an equivalence between the atomic ℓ_0 norm and rank minimization.

Proposition 4.6.1 *([42, Theorem 11.13]) For any $N \times N_F$ matrix $\widetilde{\mathbf{Y}}$ with an atomic decomposition of the form* (4.35) *(which includes any $\widetilde{\mathbf{Y}}$ satisfying* (4.31)*), $\|\widetilde{\mathbf{Y}}\|_{\mathcal{A},0}$ is equal to the optimal value of the following rank minimization problem:*

$$\begin{aligned} \min_{\mathbf{W},\mathbf{u}} \quad & \mathrm{rank}(\mathrm{Toep}(\mathbf{u})) \\ s.t. \quad & \begin{bmatrix} \mathrm{Toep}(\mathbf{u}) & \widetilde{\mathbf{Y}} \\ \widetilde{\mathbf{Y}}^H & \mathbf{W} \end{bmatrix} \succeq 0. \end{aligned} \tag{4.36}$$

Remark To summarize our intuition, the proposition above indicates that (4.23), which is essentially a reduced-dimension convex relaxation of (4.36), will promote both low-rankness and Toeplitz structure and therefore yields a favorable covariance matrix estimation that reveals the sparse decomposition of the DOAs and is consistent with the observed data.

4.7 Numerical Results

We use numerical experiments to examine the performance of the method. In this section, N_F and N_f are used to denote the number of frequencies for the uniform and non-uniform frequency set, respectively. N_M and N_m are used to denote the number of sensors for the uniform and non-uniform array spacing sets, respectively. For each experiment and trial, K DOAs are generated. The source amplitude is complex Gaussian. N_l snapshots are collected. The uniform frequency set is defined as $\{1,...,N_F\} \cdot F_1$ (F_1 is the minimum frequency). The array spacing for ULA is $\frac{\lambda_1}{2}$ where λ_1 is the wavelength for the minimum frequency in the frequency set. The noise for each frequency and each snapshot is randomly generated from the complex Gaussian distribution $\mathcal{CN}(0,\sigma^2)$ and then scaled to fit the desired signal-to-noise ratio (SNR) defined as

$$\text{SNR} = 20\log_{10}\frac{\|\mathcal{X}\|_{\text{HS}}}{\|\mathcal{N}\|_{\text{HS}}}. \tag{4.37}$$

In the Monte-Carlo experiments, $MC = 100$ trials are executed to compute the root mean square error (RMSE) defined as

$$\text{RMSE} = \sqrt{\frac{1}{MC}\sum_{m=1}^{MC}\left[\min\left(\frac{1}{K}\sum_{k=1}^{K}(\hat{\theta}_{mk}-\theta_{mk})^2, 10^2\right)\right]}, \tag{4.38}$$

where $\hat{\theta}_{mk}$, and θ_{mk} are (sorted) estimated DOAs, and (sorted) ground-truth DOAs for the kth DOA and mth trial. A maximum threshold of 10° is used to penalize the incorrect DOA estimates. We compare the proposed method with the multi-frequency sparse Bayesian learning (SBL) [8]. The Cramér-Rao bound (CRB) [44, Eq. (121)] for the multi-frequency model is computed for reference.

4.7.1 Robustness to Aliasing/Collision

We first examine the robustness of aliasing/collision. Suppose $K = 3$ sources impinge in a ULA with $N_M = 16$ sensors. The source amplitudes are complex Gaussian and the DOAs are randomly generated from a uniform distribution with range $[15^\circ, 165^\circ]$ with minimum separation $4/N_M$ in the cosine domain. We consider $N_F = 2$ or 4 under the single-snapshot and uniform frequency case ($N_l = 1$). All frequencies other than the fundamental frequency will have the risk of aliasing/collision. We solve the SDP program (4.23) by CVX [38] and apply the root-MUSIC (Vandermonde decomposition) to retrieve the DOAs.

From Fig. 4.5 (a)–(b), we can see the primal ANM is more robust to the aliasing than SBL. It also overcomes the collision issues for the dual ANM [10]. Moreover, the primal ANM does not need any hyper-parameter tuning and it therefore avoids the bias from the regularization terms.

4.7.2 Non-uniform Frequency Cases

We examine the performance under the non-uniform frequency set. In this case, $N_f = 4$, and the frequency set is $\{100, 200, 300, 500\}$ Hz and $\{200, 300, 400, 500\}$ Hz. Other conditions are the same as in Sec. 4.7.1. Fig. 4.5 (c)-(d) demonstrates the effectiveness of the proposed method under the non-uniform frequency case. We see superior performance to the fast dual algorithm proposed in [10].

4.7.3 MMV Case

We examine the performance of ANM under the MMV setup. We consider the case $N_l = 20$, and $K = 3$ DOAs at $[88, 93, 155]^\circ + \boldsymbol{\varepsilon}$ where $\boldsymbol{\varepsilon}$ is a three dimensional random vector with uniform distribution from $[0, 1]$. Fig. 4.6 demonstrates the superior performance of ANM in the high SNR region, and it follows the trend of CRB.

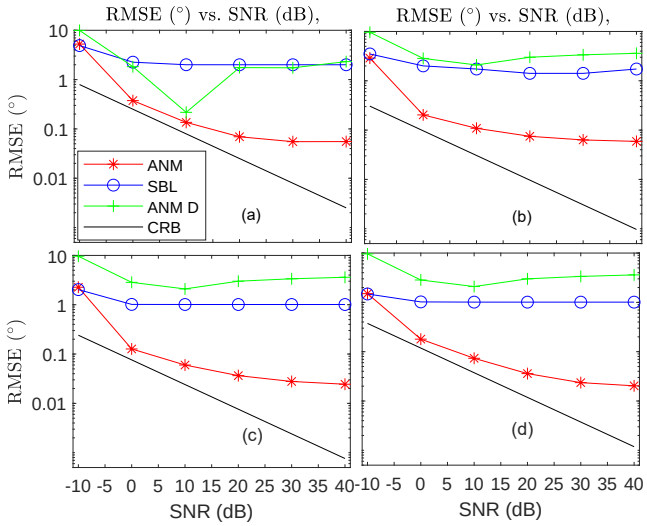

Figure 4.5: RMSE (°) versus SNR. $N_M = 16$ ULA with $d = \lambda_{100}/2$. $N_l = 1$, and $K = 3$. (a): $N_F = 2$ with frequency sets $100 \cdot \{1,2\}$ Hz; (b) - (d) $N_F = 4$ with frequency set (b) $100 \cdot \{1,2,3,4\}$ Hz, (c) $100 \cdot \{1,2,3,5\}$ Hz and (d) $100 \cdot \{2,3,4,5\}$ Hz. "ANM P" and "ANM D" represent the primal and dual SDP.

We then examine the performance of ANM with varying numbers of snapshots N_l for SNR = 20 dB, and the other setup as Fig. 4.6. From Fig. 4.7, we can see ANM follows the trend of CRB and outperforms SBL. In addition, comparing Fig. 4.7 (a) with Fig. 4.7 (b), ANM performs better with higher N_F, which demonstrates the benefits of muli-frequency processing.

4.7.4 The Effect of Multiple Frequencies

We study the performance of the method under varying N_F in Fig. 4.8. From Fig. 4.8 (a), the estimation error of ANM generally goes down with increasing N_F and the only exception is $N_F = 7$. To understand that, the true and the aliasing DOAs are in Fig. 4.8 (b). It can be seen that the DOAs 93° and 155° collide with each other at frequency 700 Hz. There are other intersection points between the solid and dashed lines but none of them lie in any frequency that belongs to the frequency set. That explains why the error significantly goes up when N_F increases from 6 to 7.

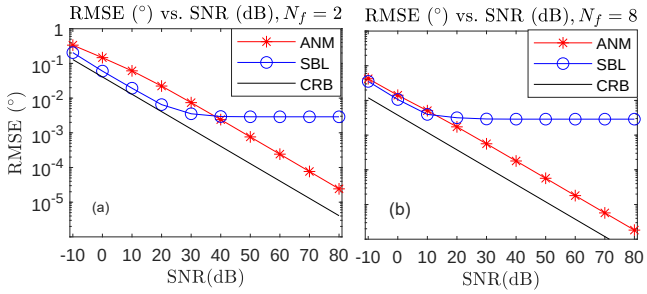

Figure 4.6: RMSE (°) versus SNR for MMV setup. $N_M = 16$ ULA with $d = \lambda_{100}/2$. $K = 3$ DOAs at $[88°, 93°, 155°] + \boldsymbol{\varepsilon}$ where $\boldsymbol{\varepsilon}$ is the random offsets from a uniform distribution $[0,1]$. $N_l = 20$. (a): $N_F = 2$ with frequency set $\{100, 200\}$ Hz; (b) $N_F = 8$ with frequency set $\{100, \ldots, 800\}$ Hz.

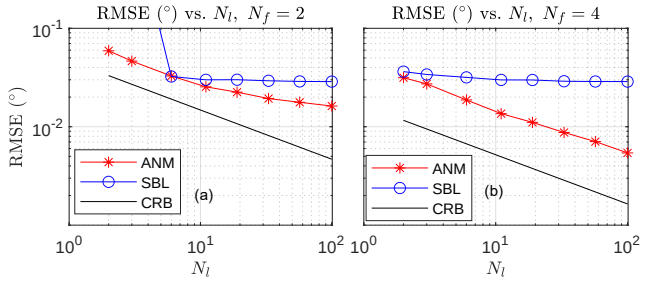

Figure 4.7: RMSE (°) versus N_l for MMV setup. $N_M = 16$ ULA with $d = \lambda_{100}/2$. $K = 3$ DOAs at $[88°, 93°, 155°] + \boldsymbol{\varepsilon}$ where $\boldsymbol{\varepsilon}$ is the random offsets from a uniform distribution $[0,1]$. SNR = 20 dB. (a): $N_F = 2$ with frequency set $\{100, 200\}$ Hz; (b) $N_F = 4$ with frequency set $\{100, 200, 300, 400\}$ Hz.

4.7.5 Co-prime Array and More Sources than Sensors

We examine an $N_m = 6$ co-prime array, a particular example of the non-uniform array (NUA). A co-prime array involves two ULAs with spacing $M_1 d$ and $M_2 d$. M_1 and M_2 are co-prime integers and their greatest common divisor is 1. The first ULA has M_2 sensors and the second ULA has $2M_1$ sensors. Since the first sensor is shared, there are $N_m = 2M_1 + M_2 - 1$ sensors in the array. In this example, we consider $M_1 = 2$, $M_2 = 3$. $N_f = 3$ and the non-uniform frequency set is $\{100, 300, 400\}$ Hz. $d = \lambda_{100}/2$. The first ULA is $[0, 2d, 4d]$ and the second ULA is $[0, 3d, 6d, 9d]$. The entire co-prime array is $[0, 2d, 3d, 4d, 6d, 9d]$. $N_l = 50$, SNR = 20 dB, and $K = 7$ DOAs with at $\{45, 60, 75, 90, 105, 120, 140\}°$. Note, $K > N_m$ in this case.

From Fig. 4.9, the proposed method resolves more DOAs than sensors in the NUA case,

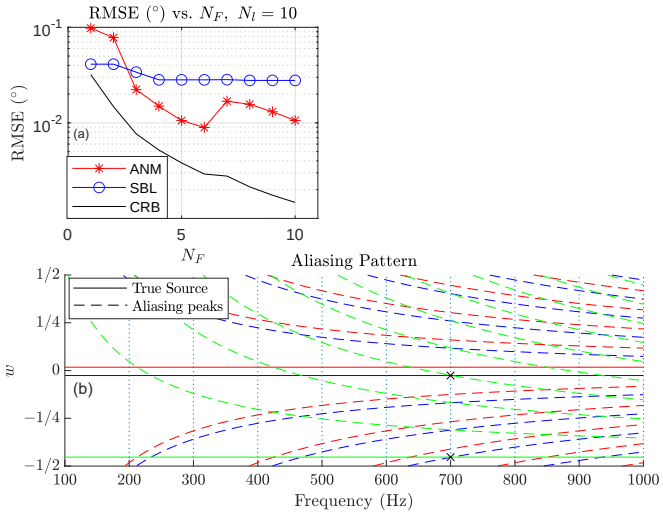

Figure 4.8: (a) RMSE (°) versus N_F and (b) aliasing pattern for MMV setup. $N_M = 16$ ULA with $d = \lambda_{100}/2$. $N_l = 10$. The frequency set is $\{1,\ldots,N_F\} \cdot 100$ Hz. $K = 3$ DOAs at $[88°, 93°, 155°] + \boldsymbol{\varepsilon}$ where $\boldsymbol{\varepsilon} \sim U(0,1)$. SNR = 20 dB. In (b), the true (solid) and the aliasing DOAs (dashed) are shown.

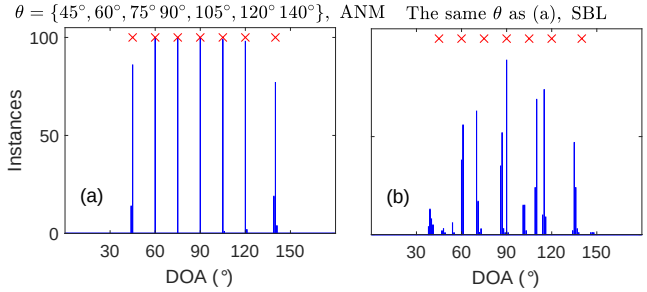

Figure 4.9: Histogram for the estimated DOAs for (a) ANM, and (b) SBL under the co-prime array with N_m= 6 (sensor locations are $[0,2,3,4,6,9]$), N_f = 3 ($[100,300,400]$ Hz), N_l = 50, SNR = 20 dB, and K = 7. The RMSE for ANM is 0.2°, and for SBL 8.6°.

while SBL fails in this case and has a high RMSE (The maximum RMSE is 10° as the maximum threshold of the RMSE for one trial is 10° based on (4.38)).

Further, we examine the case when there are more DOAs than sensors *under the ULA setup*. We have already demonstrated that in Sec. 4.5 under a noise-free and uniform amplitude setup. Here, we consider a more practical case when there is noise and the amplitude is random. From Fig. 4.10, ANM can resolve 6 DOAs when only $N_M = 4$ physical sensors are available under the noisy and non-uniform amplitude case and it achieves lower RMSE performance than

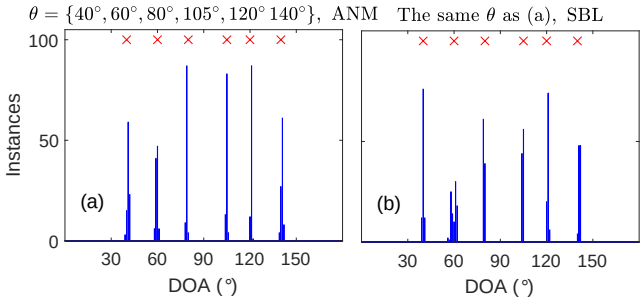

Figure 4.10: Histogram for the estimated DOAs for an ULA (a) ANM, and (b) SBL. $N_M = 4$, $N_F = 3$ ($[100, 200, 300]$ Hz), $N_l = 50$, SNR = 20 dB and $K = 6$. The RMSE for ANM is $0.90°$, and for SBL $1.10°$.

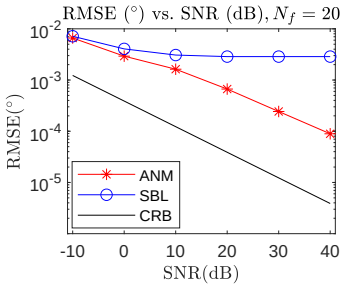

Figure 4.11: RMSE (°) versus SNR for MMV setup. $N_M = 20$ ULA with $d = \lambda_{100}/2$. $K = 3$ DOAs at $[88°, 93°, 155°] + \boldsymbol{\varepsilon}$ where $\boldsymbol{\varepsilon}$ is the random offsets from a uniform distribution $[0, 1]$. $N_l = 10$. (a): $N_F = 20$ with frequency set $\{100, \ldots, 2000\}$ Hz.

SBL.

4.7.6 Practical Test

We consider a case with $N_F = 20$ frequencies, $N_l = 10$ snapshots, and $N_M = 20$ sensors. In previous examples, the number of frequencies is small, but in practical cases, there may be much more frequencies in the wideband signal. We compare the performance to the SBL with high resolution $0.01°$. From Fig. 4.11, our method can deal with such a practical case with lower RMSE than the high-resolution SBL.

4.8 Conclusion

This paper proposes a gridless DOA estimation method based on *regularization-free* SDP and Vandermonde decomposition. We further extend this framework to MMV, NUA, and non-uniform frequency cases. Under the NUA and non-uniform frequency case, the Toeplitz structure will not hold. However, we demonstrate the possibility of using IVD in these cases, and the existence of IVD is theoretically guaranteed. With the help of multiple frequencies, the method can resolve more sources than the number of physical sensors under the ULA setup. Therefore, multi-frequency processing can reduce hardware complexity and increase the maximum resolvable sources. Numerical results demonstrate the proposed framework is robust to noise and aliasing and can achieve a superior performance under the MMV, NUA, and NUF setup.

4.9 Appendix

4.9.1 Proof for Proposition 4.3.1

Proof The primal atomic norm $\|\mathcal{X}\|_{\mathcal{A}}$ is expressed in terms of the dual atomic norm $\|Q\|_{\mathcal{A}}^*$ as

$$\|\mathcal{X}\|_{\mathcal{A}} = \sup_{\|Q\|_{\mathcal{A}}^* \leq 1} \langle Q, \mathcal{X} \rangle_{\mathbb{R}} = \sup_{\|Q\|_{\mathcal{A}}^* \leq 1} \langle Q, \mathcal{Y} \rangle_{\mathbb{R}}, \tag{4.39}$$

where the last equality is only for the noise-free case.

For any dual variable Q, we can define the *dual polynomial matrix* $\mathbf{\Psi}(Q,w) \in \mathbb{C}^{N_F \times N_l}$ as

$$\mathbf{\Psi}(Q,w) := [\mathbf{Q}_1^H \mathbf{a}(1,w) \dots \mathbf{Q}_{N_F}^H \mathbf{a}(N_F,w)]^T. \tag{4.40}$$

Note that since each frequency has different array manifold vectors, it is difficult to express $\mathbf{\Psi}(Q,w)$ as a matrix multiplication of Q and a vector. To construct a homogeneous

representation for $\mathbf{\Psi}(Q,w)$, we will leverage $\mathbf{z} := [z^0 \dots z^{N-1}]^T \in \mathbb{C}^N$ ($z = z(w) := e^{-j2\pi w}$), an ensemble of the array manifold, and the matrix $\widetilde{\mathbf{Q}}_f \in \mathbb{C}^{N\times N_l}$ defined as follows [10, eq. (14)]

$$\widetilde{\mathbf{Q}}_f(i,l) = \begin{cases} \mathbf{Q}_f(m,l) & \text{for } (i,l) = (f\cdot(m-1)+1, l) \\ 0 & \text{otherwise,} \end{cases} \tag{4.41}$$

or $\widetilde{\mathbf{Q}}_f = \mathcal{R}(\mathbf{Q}_f)$.

With the help of $\widetilde{\mathbf{Q}}_f$ and $\mathbf{z}$, $\mathbf{\Psi}(Q,w)$ has the representation

$$\mathbf{\Psi}(Q,w) = [\widetilde{\mathbf{Q}}_1^H \mathbf{z} \dots \widetilde{\mathbf{Q}}_{N_F}^H \mathbf{z}]^T. \tag{4.42}$$

Now, we consider $\|Q\|_{\mathcal{A}}^*$, which appears in the constraint in (4.39). Recalling that $\|\mathbf{X}_w\|_F = 1$, we have a similar derivation to [10, eq. (17)]:

$$\begin{aligned} \|Q\|_{\mathcal{A}}^* &:= \sup_{\|\mathcal{X}\|_{\mathcal{A}}\le 1} \langle Q, \mathcal{X}\rangle_{\mathbb{R}} = \sup_{\|\mathcal{X}\|_{\mathcal{A}}\le 1} \langle Q, \mathbf{A}(w) * \mathbf{X}_w^T\rangle_{\mathbb{R}} \\ &= \sup_{\substack{\mathbf{X}_w \\ w}} \mathrm{Tr}[\sum_{f=1}^{N_F} \mathbf{Q}_f^H \mathbf{a}(f,w)\mathbf{x}_w^T(f)] \\ &= \sup_{\substack{\mathbf{X}_w \\ w}} \mathrm{Tr}[\mathbf{\Psi}^H \mathbf{X}_w] = \sup_w \|\mathbf{\Psi}(Q,w)\|_F. \end{aligned} \tag{4.43}$$

Using (4.43), the condition $\|Q\|_{\mathcal{A}}^* \le 1$ can be equivalently formulated as an SDP constraint. Construct a similar polynomial as in [10, eq. (23)]:

$$\begin{aligned} R(w) &:= 1 - \|\mathbf{\Psi}(Q,w)\|_F^2 = 1 - \mathrm{Tr}[\mathbf{\Psi}^H(Q,w)\mathbf{\Psi}(Q,w)] \\ &= 1 - \mathrm{Tr}(\sum_{f=1}^{N_F} \widetilde{\mathbf{Q}}_f^H \mathbf{z}\mathbf{z}^H \widetilde{\mathbf{Q}}_f) = 1 - \sum_{f=1}^{N_F} \mathbf{z}^H \widetilde{\mathbf{Q}}_f \widetilde{\mathbf{Q}}_f^H \mathbf{z}. \end{aligned} \tag{4.44}$$

Therefore, $\|Q\|_{\mathcal{A}}^* \le 1$ holds if and only if $R(w) \ge 0$ for all $w \in [-1/2, 1/2]$.

Now, suppose there exists a matrix $\mathbf{P}_0 \in \mathbb{C}^{N\times N}$ such that the constraints in (4.13) hold.

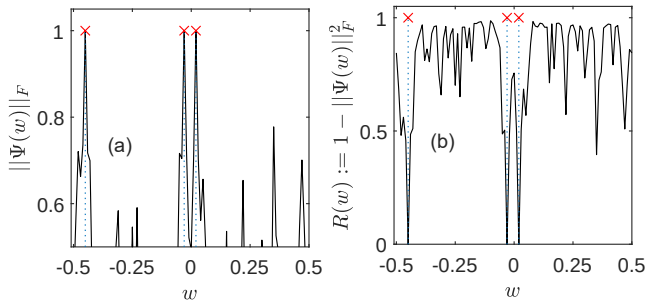

Figure 4.12: Dual polynomial visualization. A ULA with $N_M = 16$ sensors and spacing $d = c/2F_1$ ($F_1 = 100$ Hz) is used. $N_F = 5$, $N_l = 5$, $\theta = [87.7076^\circ, 93.4398^\circ, 154.1581^\circ]$, and $w = [0.02, -0.03, -0.45]$. (a) $\|\boldsymbol{\psi}(\mathbf{Q}, w)\|_F$ versus w; (b) $R(w)$ versus w.

We must argue that $R(w) \geq 0$ and therefore $\|Q\|_{\mathcal{A}}^* \leq 1$ for all w. Consider the expression $\mathbf{z}^H \mathbf{P}_0 \mathbf{z}$ and note that

$$\mathbf{z}^H \mathbf{P}_0 \mathbf{z} = \mathrm{Tr}(\mathbf{z}\mathbf{z}^H \mathbf{P}_0) = \sum_{k=-(N-1)}^{N-1} r_k z^{-k} \tag{4.45}$$

where $r_k = \sum_{i=1}^{N-k} \mathbf{P}_0(i, i+k)$ for $k \geq 0$ and $r_k = r_{-k}^*$ for $k < 0$. Since $\sum_{i=1}^{N-k} \mathbf{P}_0(i, i+k) = \delta_k$ holds, we can conclude that $\mathbf{z}^H \mathbf{P}_0 \mathbf{z} = z^0 = 1$. Define $\mathbf{P}_1 := \sum_{f=1}^{N_F} \widetilde{\mathbf{Q}}_f \widetilde{\mathbf{Q}}_f^H = \widetilde{\mathbf{Q}} \widetilde{\mathbf{Q}}^H$ and substitute this fact into $R(w)$. We have

$$R(w) = \mathbf{z}^H \mathbf{P}_0 \mathbf{z} - \mathbf{z}^H \mathbf{P}_1 \mathbf{z} = \mathbf{z}^H (\mathbf{P}_0 - \mathbf{P}_1) \mathbf{z}. \tag{4.46}$$

Since $\begin{bmatrix} \mathbf{P}_0 & \widetilde{\mathbf{Q}} \\ \widetilde{\mathbf{Q}}^H & \mathbf{I}_{N_l N_F} \end{bmatrix} \succeq 0$, its Schur complement $\mathbf{P}_0 - \widetilde{\mathbf{Q}} \mathbf{I}_{N_F}^{-1} \widetilde{\mathbf{Q}}^H = \mathbf{P}_0 - \mathbf{P}_1 \succeq 0$, and so $R(w) \geq 0$ for all $w \in [-1/2, 1/2]$.

Next, suppose $R(w) \geq 0$ for all $w \in [-1/2, 1/2]$. We need to argue that there exists a matrix $\mathbf{P}_0 \in \mathbb{C}^{N \times N} \succeq 0$ such that the constraints in (4.13) hold. Since $R(w) \leq 0$, $1 \geq \mathbf{z}^H \mathbf{P}_1 \mathbf{z}$, where $\mathbf{P}_1 := \sum_{f=1}^{N_F} \widetilde{\mathbf{Q}}_f \widetilde{\mathbf{Q}}_f^H = \widetilde{\mathbf{Q}} \widetilde{\mathbf{Q}}^H$. From [45, Lemma 4.25] and the fact that 1 and $\mathbf{z}^H \mathbf{P}_1 \mathbf{z}$ are both univariate trigonometric polynomials, it follows that there exists $\mathbf{P}_0 \succeq \mathbf{P}_1$ such that $1 = \mathbf{z}^H \mathbf{P}_0 \mathbf{z}$ and $\sum_{i=1}^{N-k} \mathbf{P}_0(i, i+k) = \delta_k$ hold. The matrix $\begin{bmatrix} \mathbf{P}_0 & \widetilde{\mathbf{Q}} \\ \widetilde{\mathbf{Q}}^H & \mathbf{I}_{N_l N_F} \end{bmatrix}$ has Schur complement $\mathbf{P}_0 - \widetilde{\mathbf{Q}} \mathbf{I}_{N_F}^{-1} \widetilde{\mathbf{Q}}^H = \mathbf{P}_0 - \mathbf{P}_1 \succeq 0$, and therefore this matrix is positive semi-definite. This concludes the proof. □

Acknowledgement

The text of this chapter is in part and under some rearrangements a reprint of the material as it appears in Yifan Wu, Michael B. Wakin, and Peter Gerstoft, "Regularization-free Gridless DOA Estimation for Multi-frequency Signals", *IEEE Transactions on Signal Processing*, to be submitted 2023. The dissertation author was the primary researcher and author of this chapter. The co-authors listed in these publications directed and supervised the research.

Bibliography

[1] H. L. Van Trees, *Optimum array processing: Part IV of detection, estimation, and modulation theory* (John Wiley & Sons, 2002).

[2] Y. Chen, L. Yan, C. Han, and M. Tao, "Millidegree-level direction-of-arrival estimation and tracking for terahertz ultra-massive mimo systems," IEEE Trans. Wirel. Comm. **21**(2), 869–883 (2021).

[3] C. Vasanelli, F. Roos, A. Durr, J. Schlichenmaier, P. Hugler, B. Meinecke, M. Steiner, and C. Waldschmidt, "Calibration and direction-of-arrival estimation of millimeter-wave radars: A practical introduction," IEEE Antennas and Propag. Mag. **62**(6), 34–45 (2020).

[4] R. O. Schmidt, "Multiple emitter location and signal parameter estimation," IEEE Trans. Antennas Propagat. **34**(3), 276–280 (1986).

[5] R. Roy and T. Kailath, "Esprit-estimation of signal parameters via rotational invariance techniques," IEEE Trans. Acoust., Speech, and Signal Process. **37**(7), 984–995 (1989).

[6] M. Wax, T. Shan, and T. Kailath, "Spatio-temporal spectral analysis by eigenstructure methods," IEEE Trans. Acoust., Speech, Signal Process. **32**(4), 817–827 (1984).

[7] N. Antonello, E. De Sena, M. Moonen, P. A. Naylor, and T. van Waterschoot, "Joint acoustic localization and dereverberation through plane wave decomposition and sparse regularization," IEEE/ACM Trans. Audio, Speech, Lang. Process. **27**(12), 1893–1905 (2019).

[8] S. Nannuru, K. L. Gemba, P. Gerstoft, W. S. Hodgkiss, and C. F. Mecklenbräuker, "Sparse bayesian learning with multiple dictionaries," Signal Process. **159**, 159–170 (2019).

[9] K. L. Gemba, S. Nannuru, and P. Gerstoft, "Robust ocean acoustic localization with sparse Bayesian learning," IEEE J. Sel. Topics Signal Process. **13**(1), 49–60 (2019).

[10] Y. Wu, M. B. Wakin, and P. Gerstoft, "Gridless doa estimation with multiple frequencies," IEEE Trans. Signal Process. **71**, 417–432 (2023).

[11] H. Wang and M. Kaveh, "Coherent signal-subspace processing for the detection and estimation of angles of arrival of multiple wideband sources," IEEE Trans. Acoust., Speech, Signal Process. **33**(4), 823–831 (1985).

[12] K. M. Buckley and L. J. Griffiths, "Broad-band signal-subspace spatial-spectrum (BASS-ALE) estimation," IEEE Trans. Acoust., Speech, Signal Process. **36**(7), 953–964 (1988).

[13] E. D. Di C. and R. Parisi, "WAVES: Weighted average of signal subspaces for robust wideband direction finding," IEEE Trans. Signal Process. **49**(10), 2179–2191 (2001).

[14] Y. Yoon, L. M. Kaplan, and J. H. McClellan, "TOPS: New DOA estimator for wideband signals," IEEE Trans. Signal Process. **54**(6), 1977–1989 (2006).

[15] Z. Tang, G. Blacquiere, and G. Leus, "Aliasing-free wideband beamforming using sparse signal representation," IEEE Trans. Signal Process. **59**(7), 3464–3469 (2011).

[16] K. L. Gemba, S. Nannuru, P. Gerstoft, and W. S. Hodgkiss, "Multi-frequency sparse Bayesian learning for robust matched field processing," J. Acoust. Soc. Am. **141**(5), 3411–3420 (2017).

[17] J. Zhang, N. Hu, M. Bao, X. Li, and W. He, "Wideband DOA estimation based on block FOCUSS with limited samples," in *IEEE GlobalSIP* (2013), pp. 634–637.

[18] L. Wang, L. Zhao, G. Bi, C. Wan, L. Zhang, and H. Zhang, "Novel wideband DOA estimation based on sparse Bayesian learning with Dirichlet process priors," IEEE Trans. Signal Process. **64**(2), 275–289 (2015).

[19] C. Liu, Y. V. Zakharov, and T. Chen, "Broadband underwater localization of multiple sources using basis pursuit denoising," IEEE Trans. Signal Process. **60**(4), 1708–1717 (2011).

[20] V. Chandrasekaran, B. Recht, P. A. Parrilo, and A. S. Willsky, "The convex geometry of linear inverse problems," Found. Comput. Math. **12**(6), 805–849 (2012).

[21] E. J. Candès and C. Fernandez-Granda, "Towards a mathematical theory of super-resolution," Commun. Pure Appl. Math. **67**(6), 906–956 (2014).

[22] G. Tang, B. N. Bhaskar, P. Shah, and B. Recht, "Compressed sensing off the grid," IEEE Trans. Inf. Theory **59**(11), 7465–7490 (2013).

[23] Y. Li and Y. Chi, "Off-the-grid line spectrum denoising and estimation with multiple measurement vectors," IEEE Trans. Signal Process. **64**(5), 1257–1269 (2015).

[24] Z. Yang and L. Xie, "Exact joint sparse frequency recovery via optimization methods," IEEE Trans. Signal Process. **64**(19), 5145–5157 (2016).

[25] Z. Yang, J. Tang, Y. C. Eldar, and L. Xie, "On the sample complexity of multichannel frequency estimation via convex optimization," IEEE Trans. Inf. Theory **65**(4), 2302–2315 (2018).

[26] M. Wagner, Y. Park, and P. Gerstoft, "Gridless DOA estimation and root-MUSIC for non-uniform linear arrays," IEEE Trans. Signal Process. **69**, 2144–2157 (2021).

[27] Y. Wu, M. B. Wakin, and P. Gerstoft, "Gridless DOA estimation under the multi-frequency model," in *IEEE ICASSP* (2022), pp. 5982–5986.

[28] S. Li, D. Yang, G. Tang, and M. B. Wakin, "Atomic norm minimization for modal analysis from random and compressed samples," IEEE Trans. Signal Process. **66**(7), 1817–1831 (2018).

[29] Y. Chi and M. F. Da Costa, "Harnessing sparsity over the continuum: Atomic norm minimization for superresolution," IEEE Signal Process. Mag. **37**(2), 39–57 (2020).

[30] A. Moffet, "Minimum-redundancy linear arrays," IEEE Trans. Antennas Propag. **16**(2), 172–175 (1968).

[31] G. S. Bloom and S. W. Golomb, "Applications of numbered undirected graphs," Proceedings of the IEEE **65**(4), 562–570 (1977).

[32] P. P. Vaidyanathan and P. Pal, "Sparse sensing with co-prime samplers and arrays," IEEE Trans. Signal Process. **59**(2), 573–586 (2010).

[33] P. Pal and P. P. Vaidyanathan, "Nested arrays: A novel approach to array processing with enhanced degrees of freedom," IEEE Trans. Signal Process. **58**(8), 4167–4181 (2010).

[34] M. Wang and A. Nehorai, "Coarrays, music, and the cramér–rao bound," IEEE Trans. Signal Process. **65**(4), 933–946 (2016).

[35] M. C. Dogan and J. M. Mendel, "Applications of cumulants to array processing. i. aperture extension and array calibration," IEEE Trans. Signal Process. **43**(5), 1200–1216 (1995).

[36] P. Chevalier, L. Albera, A. Ferréol, and P. Comon, "On the virtual array concept for higher order array processing," IEEE Trans. Signal Process. **53**(4), 1254–1271 (2005).

[37] W. Ma, T. Hsieh, and C. Chi, "Doa estimation of quasi-stationary signals via khatri-rao subspace," in *2009 ICASSP*, IEEE (2009), pp. 2165–2168.

[38] M. Grant and S. Boyd, "CVX: Matlab software for disciplined convex programming, version 2.1," (2014).

[39] A. Xenaki and P. Gerstoft, "Grid-free compressive beamforming," J. Acoust. Soc. Am. **137**, 1923–1935 (2015).

[40] P. Gerstoft, C. F. Mecklenbräuker, A. Xenaki, and S. Nannuru, "Multisnapshot sparse Bayesian learning for DOA," IEEE Signal Process. Lett. **23**(10), 1469–1473 (2016).

[41] B. D. Rao and K. S. Hari, "Performance analysis of root-music," IEEE Trans. Acoust., Speech, and Signal Process. **37**(12), 1939–1949 (1989).

[42] Z. Yang, J. Li, P. Stoica, and L. Xie, "Sparse methods for direction-of-arrival estimation," in *Academic Press Library in Signal Processing, Volume 7* (Elsevier, 2018), pp. 509–581.

[43] C. Zhou, Y. Gu, X. Fan, Z. Shi, G. Mao, and Y. D. Zhang, "Direction-of-arrival estimation for coprime array via virtual array interpolation," IEEE Trans. Signal Process. **66**(22), 5956–5971 (2018).

[44] Y. Liang, W. Liu, Q. Shen, W. Cui, and S. Wu, "A review of closed-form Cramér-Rao bounds for DOA estimation in the presence of Gaussian noise under a unified framework," IEEE Access **8**, 175101–175124 (2020).

[45] B. Dumitrescu, *Positive trigonometric polynomials and signal processing applications*, Vol. 103 (Springer, 2017).

Chapter 5

Conclusion and Future Work

5.1 Conclusion

In this dissertation, wideband source localization is studied from both data-driven and model-based perspectives.

For the data-driven part, a novel deep learning based sound source localization method is proposed. The method is based on multi-task learning and image translation network. The network is designed according to the encoder-decoder structure to implement the multi-task learning so that the network can jointly localize the sound sources and mitigate the multipath artifacts from the reverberation. The blocks and layers are designed according to the image translation network to enhance the generalization performance. Extensive experiments show that the proposed network can outperform the baseline methods and can generalize to the unseen data in the training phase.

For the model-based part, a gridless DOA estimation method is proposed under the multi-frequency model which is used to model the wideband source. The multi-frequency DOA estimation problem is formulated as an atomic norm minimization problem so that the method is gridless and the grid mismatch error can be avoided. An SDP that is equivalent to atomic

norm is derived to make the problem computationally feasible. The SDP is formulated both in the primal and dual form and extensive analysis for both forms is given. The primal form is regularization-free and it has the benefit of avoiding the regularization bias. The method is studied under various setups, including the multiple measurement vector, non-uniform array, and non-uniform frequency cases. In addition, it turns out that the proposed framework is able to resolve more sources than the number of physical sensors under the *uniform linear array* setup due the intrinsic structure of the multi-frequency model. Extensive theoretical analysis and numerical experiments are given to demonstrate the effectiveness of the proposed method.

5.2 Future Work

5.2.1 Wideband Source Localization based on Deep Unrolling Network

Model-based and data-driven methods both have their advantages and disadvantages. Recently, there is a new technique called deep unrolling network [1–7] aiming to incorporate the data-driven module into the traditional model-based optimization framework to enhance the generalization and interpretability of the method. The deep unrolling network is based on an iterative algorithm and unrolls it to a number of layers that consist of learnable parameters. Most hyperparameters in the original iterative algorithm become the learnable parameters in the network. By feeding the network with training data, it can adjust these parameters properly to perform the task better. Many works show that the deep unrolling network has a faster convergence compared to the original iterative method, better interpretability than black box neural networks, and satisfactory generalization performance in the data-limited case [1]. Due to these appealing merits, there has been a surge of efforts to unroll iterative algorithms for many signal processing problems including compressive sensing [2, 3, 7], deconvolution [4], graph signal processing [5], and medical imaging [6]. Moreover, with the help of training data, the unrolling network can potentially solve a more challenging task compared to the original iterative method. It will be

interesting to apply the deep unrolling network to the wideband source localization problem and it is likely to be both faster and more accurate than the existing data-driven and model-based methods.

5.2.2 Sound Source Localization for Multiple Sources

In Chapter 2 of the dissertation, a deep learning based sound source localization is developed under the single source assumption. It will be an interesting future direction to extend the current framework to the multiple sources case. It will be a challenging problem to consider the case when multiple sources are active simultaneously.

5.2.3 Multi-frequency DOA Estimation under the Non-integer Spacing or Frequency Case

In Chapter 4 of the dissertation, the sensor index set and the frequency set are both assumed to be an integer set so that the T operator and the irregular Vandermonde decomposition are both valid. It will be interesting to study if this assumption can be relaxed so that the method can be generalized to any real sensor index set and frequency set.

Bibliography

[1] V. Monga, Y. Li, and Y. C. Eldar. Algorithm unrolling: Interpretable, efficient deep learning for signal and image processing. *IEEE Signal Process. Mag.*, 38(2):18–44, 2021.

[2] Y. Yang, J. Sun, H. Li, and Z. Xu. Deep admm-net for compressive sensing mri. In *NIPS*, 2016.

[3] Y. Yang, J. Sun, H. Li, and Z. Xu. Admm-csnet: A deep learning approach for image compressive sensing. *IEEE Trans. Pattern Anal. Mach. Intell.*, 42(3):521–538, 2018.

[4] Y. Li, M. Tofighi, V. Monga, and Y. C. Eldar. An algorithm unrolling approach to deep image deblurring. In *IEEE ICASSP*, pages 7675–7679. IEEE, 2019.

[5] S. Chen, Y. C. Eldar, and L. Zhao. Graph unrolling networks: Interpretable neural networks for graph signal denoising. *IEEE Trans. Signal Process.*, 69:3699–3713, 2021.

[6] Y. B. Sahel, J. P. Bryan, B. Cleary, S. L. Farhi, and Y. C. Eldar. Deep unrolled recovery in sparse biological imaging: Achieving fast, accurate results. *IEEE Signal Process. Mag.*, 39(2):45–57, 2022.

[7] H. Zhu, W. Feng, C. Feng, T. Ma, and B. Zou. Deep unfolded gridless doa estimation networks based on atomic norm minimization. *Remote Sensing*, 15(1):13, 2022.